

Chemical Gas Sensors based on Functionalized Self-Actuated Piezo-Resistive Cantilevers

Dissertation zur Erlangung des akademischen Grades eines Doktors
der Ingenieurwissenschaften (Dr.-Ing.) im
Fachbereich Elektrotechnik / Informatik
der Universität Kassel

vorgelegt von

Dipl.-Ing. Denys Filenko

Kassel, 2008

Erstgutachter Prof. Dr. Johann Peter Reithmaier

Zweitgutachter Prof. Dr. Hartmut Hillmer

Prüfungsgremium Prof. Dr. Johann Peter Reithmaier

Prof. Dr. Hartmut Hillmer

Prof. Dr. Dirk Dahlhaus

Prof. Dr. Josef Börcsök

Tag der mündlichen Prüfung 19 Dezember 2008

Dissertation an der Universität Kassel, Fachbereich 16 (Elektrotechnik)
vorgelegt am 20 Juni 2008

© 2008 Denys Filenko

*To my mother Valentyna Redina
and my father Anatolii Filenko*

Summary

Investigation of physical, chemical, and biochemical properties of various substances plays a vital role for many scientific, household, and industrial applications. In comparison with normally expensive and cumbersome spectroscopy equipment, handheld application-specific chemical and biological sensors offer rapid and low-cost analysis of many chemical and biological species. Microcantilever-based sensors offer significant advantages over other types of chemical sensors (based on SAW, QCM, ISFET, etc.) in terms of better specific mass sensitivity, broader dynamic response, improved reliability and precision, greatly reduced size, versatility, etc. Their ability to operate in vacuum, gases, and liquids as well as compatibility with standard silicon microtechnology make them excellent candidates for mass production and further adaptation to a wide range of practical applications.

This thesis is focused on the application of functionalized microcantilevers with integrated piezo-resistive read-out and bimorph-effect actuator for chemical gas sensors, which are capable to fast, portable, and inexpensive detection and recognition of different volatile substances.

This study includes an overview of general concepts and major types of (bio-)chemical sensors. Main application fields for advantageous implementation of (bio-)chemical sensors are listed. Particular attention is paid to the microcantilever-based sensor array concept, which can be employed as “electronic nose” for volatile organic compounds discrimination. Recent advances in microcantilever-based chemical sensors are reviewed and actual research challenges are outlined.

Integrated cantilever design used in this study is described and main transduction scenarios are considered. Cantilever operation in both static bending and dynamic resonant modes is theoretically analysed. Special emphasis is placed on analytical descriptions of the cantilever operation for fast and explicit estimations of the cantilever resonant behaviour and corresponding mass sensitivity. Accurate estimation of the cantilever resonance frequencies at the first and higher modes of its transversal vibration is carried out by remaining consistence with simple harmonic oscillator model, which possess a phenomenological effective mass. Geometrical parameters, which allow calculating of the effective mass at higher modes, have

been derived for the first time. Dependences of the resonance frequency on the cantilever dimensions are simulated.

Mass-sensitivity improvement by operating the microcantilevers at higher modes is analytically simulated, experimentally demonstrated, compared and analysed. Mass sensitivity is analytically simulated for both concentrated and uniformly distributed masses. Mass resolution limitations are classified and described in terms of the cantilever intrinsic and extrinsic noises. Practically feasible signal pattern improving technique by differentiating the adsorption-induced signal and the signal gathered from a referent channel with an uncoated cantilever is implemented.

The referent channel technique is also shown to decrease influence of an initial resonance frequency drift of a thermally excited cantilever. For this purposes, influence of the temperature on the cantilever resonance frequency is analysed. Young's modulus is shown to be the principal temperature-affected parameter. Temperature-affected adsorption kinetics is also experimentally demonstrated.

Cantilever operation in dynamic resonant mode is modelled in vacuum for first and higher transversal modes of vibration. Influence of air damping is analytically introduced and experimentally verified by cantilever measurements in vacuum, air, and gas flow. A detailed discussion of various damping mechanisms in microcantilever transducers related to extrinsic as well as intrinsic dissipation phenomena is given. Energy dissipation mechanisms are discussed and Q-factor as their quantitative measure is introduced.

Actuation and detection techniques for microcantilevers are reviewed and compared. Advantages of integrated bimorph-effect actuator and piezo-resistive read-out are emphasised. Output signal from the cantilevers is modelled according to the described design of the read-out unit. Bimorph-effect actuator principle is described. Influence of the voltage supplied to the actuator on the cantilever amplitude, resonance frequency, and the offset voltage is experimentally demonstrated.

Special attention is paid to the improvement of the microcantilever transducer performance by operating the cantilevers at peculiar modes. In particular, principle of the phase-shift detection in cantilever-based chemical sensors has been implemented for the first time. Three detection principles, which are applicable to acquire information from cantilevers with piezo-resistive read-out, are described and compared. They include monitoring of the offset voltage, the resonance frequency shift, and the phase delay shift. Practical implementation of the experimental set-up allows simultaneously measuring of the offset voltage and the resonance frequency so that both dynamic and static cantilever behaviour can be monitored at the same

time. However, advantageous experimental results have been achieved by measuring phase shift of the cantilevers driven near their resonances.

The microcantilever's amplitude and phase spectra in respect to the variations in damping and the spring constant are simulated. Calibration of the phase-shift response, which is one of the key-issues of the presented work, is provided. Unambiguous relation between 1 Hz resonance frequency shift and 2.4 deg. of the phase-shift responses has been established. In addition to the absence of the quantization noise by operating the cantilevers in the phase-shift mode, practical 25x sensitivity improvement has been achieved. Such a way, advantages of phase shift measurements have been theoretically predicted and experimentally confirmed.

The experimental measurements within this work have been carried out by using specially developed experimental setup, which serves for sensors investigation in either gas flow mode or gas single injection mode as well as in vacuum. Three generations of the cantilever measurement cell are presented. Relative humidity monitoring utility has been developed. Acquisition and control electronics and software has been developed and optimised.

The thesis also overviews and summarises different sorption-induced effects and their influence on the cantilever operation. Three main sorption models are described and contributed with particular experiments: (a) adsorption onto a thin solid surface; (b) absorption by a thicker analyte-permeable coating; (c) mixed-mode sorption by a nanostructured coating. Influence of adsorption-induced spring constant variations is denoted.

Adsorption onto uncoated cantilever surfaces has been thoroughly investigated. Both theoretical and experimental data on the native and thermally grown silicon dioxide adsorption processes are represented. The resonance frequency and Q-factor modulations of an uncoated cantilever towards different analyte concentrations have been measured and analysed. Low and relatively unspecific adsorption capability of the uncoated cantilevers suggests their adaptation as referent sensors.

Functionalization of the microcantilevers has substantially contributed to the sensor selectivity along with up to 20x increase of the magnitude of the selective response. Completely novel functionalization coatings, such as inorganic chalcogenide glasses and organic phosphorylated calixarenes, have been investigated by means of the microcantilevers for the first time.

Thin (120 nm) amorphous chalcogenide $\text{Ge}_{30}\text{S}_{60}(\text{AgI})_{10}$ films have been exposed to organic vapours and their sorption properties have been investigated for the first time. Chemical modification of the chalcogenide surface with ammonia vapour has been explored. This phenomenon allows demonstrating and distinguishing of physisorption and chemisorption processes within the cantilever. Moreover, the cantilever sensitivity due to the chemical

modification of the chalcogenide surface has been significantly (~10x) improved and theoretically explained. The sensitivity degradation during intense sensor exploitation has been estimated to drop down exponentially with time constant of about 5 weeks.

Investigations on microcantilevers functionalized with conventional organic polymers have been carried out. Appropriate polymer deposition techniques are overviewed. Such organic polymers as polymethyl methacrylate, polydimethylsiloxane, polyvinylpyridine, styrene-acrylonitrile copolymers, Formvar™, vinylchloride-vinylacetate copolymer, photoresist AZ1518, etc. have been implemented as functionalization coatings. Influence of the polymer layer on the resonance properties of the cantilevers is demonstrated. Excitation of the cantilevers with thermal heater is shown to have no noticeable effect on the functionalization layers. A wide range of specific, reversible and reproducible sensor responses to the analyte vapours is demonstrated.

Simultaneous operation of the cantilevers functionalized with polydimethylsiloxane, polyvinylpyridine, and carbon nitride films has been investigated by exposure to vapours of water, ethanol, methanol, 2-propanol, as well as binary mixtures of methanol with 2-propanol and methanol with water. Cantilevers with thicker carbon nitride layers demonstrate larger responses. The time responses of the cantilevers under varying analyte concentrations have been measured. The transient responses of the cantilevers have been investigated. Significant differences in the recovery time of differently functionalized cantilevers are proposed as an additional information parameter, which can be involved to the chemical recognition algorithm.

Structural and sorption properties of tert-butyl-calixarenes, resorcinarenes, and phosphorylated calixarenes are described. Calixarene conformations, surface immobilization means, and deposition techniques are overviewed. Pioneering experimental results on the microcantilevers functionalized with tert-butyl-calixarenes and phosphorylated calixarenes are presented. Their detection and recognition abilities towards vapours of water, ethanol, methanol, 2-propanol, acetone, ammonia, and few sorts of whiskeys have been tested. Influence of either hydroxyl- or alkyl- groups, which can be attached to the calixarene macrocycle, is discussed and experimentally verified. The experimental results obtained with QCM transducers are presented. Calixarene as a wide class of innovative functionalization coatings for chemical sensors have contributed with high selectivity and well defined dynamic responses.

Achieved results suggest using of microcantilevers with integrated read-out and actuation as an advantageous platform for the next generation of (bio-)chemical sensors.

Zusammenfassung

Die Untersuchung physikalischer, chemischer und biochemischer Eigenschaften verschiedener Substanzen spielt für viele Anwendungen in der Wissenschaft, im Haushalt und in der Industrie eine wichtige Rolle. Im Vergleich zur normalerweise teuren und aufwendigen Spektroskopie bieten tragbare, anwendungsspezifische chemische und biologische Sensoren eine schnelle und kostengünstige Analyse vieler chemischer und biologischer Substanzen. Mikrocantilever-basierte Sensoren bieten signifikante Vorteile gegenüber anderen Typen von chemischen Sensoren (SAW-, QCM-, ISFET-basierte usw.) wie etwa eine bessere spezifische Masseempfindlichkeit, breitere dynamische Antwort, bessere Zuverlässigkeit und Präzision, deutlich geringere Abmessungen und größere Vielfalt. Ihre Fähigkeit, in Vakuum, Gas oder Flüssigkeit zu arbeiten, und ihre Kompatibilität zur Standard-Silizium-Mikrotechnologie machen sie zu ausgezeichneten Kandidaten für die Massenproduktion und für eine weitere Anpassung an eine Vielzahl von praktischen Anwendungen.

Der Schwerpunkt dieser Arbeit liegt in der Anwendung funktionalisierter Mikrocantilever mit integrierter bimorpher Aktuation und piezo-resistiver Detektion als chemische Gassensoren für den schnellen, tragbaren und preisgünstigen Nachweis verschiedener flüchtiger Substanzen.

Diese Arbeit enthält einen Überblick prinzipieller Konzepte und gebräuchlicher Typen (bio-)chemischer Sensoren. Es werden Hauptanwendungsfelder für den vorteilhaften Einsatz (bio-)chemischer Sensoren aufgeführt. Besondere Beachtung erfährt das Konzept des Mikrocantilver-Array, das als „elektronische Nase“ zur Erkennung flüchtiger organischer Substanzen verwendet werden kann. Neueste Fortschritte auf dem Gebiet mikrocantilever-basierter chemischer Sensoren werden diskutiert und gegenwärtige Forschungsfragen skizziert.

Es erfolgt eine Beschreibung des integrierten Mikrocantilever-Designs und der wichtigsten Signalübertragungsszenarien. Der Cantilever-Betrieb wurde sowohl im statischen Biegemodus als auch im dynamischen Resonanzmodus theoretisch und praktisch untersucht. Dabei kam dem Aufzeigen einer Methode zur schnellen und expliziten Abschätzung des Resonanzverhaltens und der Masseempfindlichkeit eine besondere Bedeutung zu. Über das Modell des harmonischen Oszillators ergibt sich eine Abschätzung für die Resonanzfrequenzen des ersten Schwingungsmodus und höherer transversaler Schwingungsmodi. Dazu wurde ein geometrischer

Faktor für die effektive Masse abgeleitet. Zudem wurde die Abhängigkeit der Resonanzfrequenz von den Cantilever-Abmessungen simuliert. Die Verbesserung der Masseempfindlichkeit bei höheren Schwingungsmodi wurde analytisch simuliert, im Experiment gezeigt, verglichen und analysiert. Darüber hinaus erfolgt eine Simulation der Masseempfindlichkeit für konzentrierte wie auch verteilte Massen. Begrenzt wird die Masseempfindlichkeit durch intrinsisches oder extrinsisches Rauschen. Im Bezug darauf wurden praktisch umsetzbare Möglichkeiten zur Verbesserung des Signalmusters durch Differenzierung des Messsignals und des Referenzsignals, welches vom unbeschichteten Cantilever kommt, durchgeführt. Außerdem vermindert die Referenzkanaltechnik den Einfluss der Temperatur auf die Resonanzfrequenz des thermisch angeregten Cantilever. Am stärksten ist der Elastizitätsmodul abhängig von der Temperatur. Die Temperaturabhängigkeit der Adsorptionskinetik wurde experimentell nachgewiesen.

Der Cantilever-Betrieb im dynamischen Resonanzmodus wurde für den erste Schwingungsmodus und höhere Schwingungsmodi modelliert. Hierbei wurde der Einfluss der Dämpfung eingefügt und experimentell durch Messungen im Vakuum, in der Luft und im Gasstrom verifiziert. Die verschiedenen Dämpfungsmechanismen in Mikrocantilever-Sensoren, bezogen auf extrinsische als auch intrinsische Energiedissipationsphänomene, werden im Detail beschrieben und der Q-Faktor als deren quantitatives Maß eingeführt.

Für Mikrocantilever werden Aktuations- und Detektionstechniken zusammengestellt und verglichen, wobei die Vorteile der integrierten bimorphen Aktuation und piezo-resistiven Detektion hervorzuheben sind. Experimentell wurde der Einfluss der Betriebsspannung auf die Schwingungsamplitude, die Resonanzfrequenz und die Offset-Spannung des Cantilever ermittelt. Besondere Beachtung erfährt die Verbesserung der Cantilever-Empfindlichkeit durch den Betrieb in speziellen Modi. Zu den drei Detektionsprinzipien, die verglichen werden, gehören die Messung der Offset-Spannung, der Resonanzfrequenz- und der Phasenverschiebung. Die praktische Umsetzung des experimentellen Aufbaus erlaubt die gleichzeitige Messung der Offset-Spannung und der Resonanzfrequenz, so dass parallel das dynamische und das statische Verhalten des Cantilever beobachtet werden kann. Indessen liefert das Messen der Phasenverschiebung eines nahe der Resonanzfrequenz betriebenen Cantilever die besten experimentellen Ergebnisse. In diesem Zusammenhang erfolgte die Kalibrierung der Phasenverschiebung, die einen zentralen Punkt dieser Arbeit darstellt. Zwischen einer Resonanzfrequenzverschiebung von 1 Hz und einer Phasenverschiebung von $2,4^\circ$ ließ sich ein eindeutiger Zusammenhang nachweisen. Zur Abwesenheit von Quantisierungsrauschen beim Messen der Phasenverschiebung wurde ferner eine 25mal höhere Empfindlichkeit erreicht. Diese

Vorteile waren theoretisch vorhergesagt und experimentell nachgewiesen worden. Darüber hinaus wurde die Wirkung von Dämpfung und Federkonstante auf die Phasen- und Amplitudenspektren simuliert.

Die experimentellen Messungen dieser Arbeit wurden mit einem speziell entwickelten Messplatz ausgeführt. Er diente der Sensoruntersuchung im Gasstrom, in Gas-Luft-Gemischen und im Vakuum. Drei Generationen der Cantilever-Messzelle werden vorgestellt. Zur Messung der relativen Feuchtigkeit wurde eine Erfassungs- und Steuerungselektronik und die dazugehörige Software entwickelt und optimiert.

Um den Cantilever als Sensor einsetzen zu können, muss er funktionalisiert sein. Im Hinblick darauf ist zuerst ein Überblick über verschiedene sorptioninduzierten Effekte und ihr Einfluss auf die Cantilever-Eigenschaften gegeben. Drei Sorptionmodelle sind beschrieben und mit experimentellen Ergebnisse unterlegt: (a) Adsorption auf einer dünnen Festkörperoberfläche; (b) Absorption in einer dicken durchlässigen Polymerschicht; (c) Adsorption und Absorption an einer Schicht mit Nanostruktur.

Die Adsorption auf einer unbeschichteten Cantilever-Oberfläche aus Siliziumoxid wurde sorgfältig recherchiert. Dabei werden theoretische und experimentelle Ergebnisse zum Adsorptionsprozess auf natürlich und thermisch gewachsenen Siliziumoxid vorgestellt. Des Weiteren wurden die Veränderung der Resonanzfrequenz und des Q-Faktors eines unbeschichteten Cantilever unter dem Einfluss verschiedener Konzentrationen der Analysesubstanzen analysiert. Aufgrund des geringen und relativ unspezifischen Adsorptionsvermögens unbeschichteter Cantilever dienten diese als Referenzsensoren.

Die Funktionalisierung der Cantilever verbessert die Selektivität und erhöht das Antwortsignal um das 20fache. Zum ersten Mal wurden völlig neue Funktionsschichten wie anorganische Chalkohalidgläser und organische phosphorierte Calixarene untersucht. So wurden dünne (120 nm) amorphe Chalkohalidglasschichten $\text{Ge}_{30}\text{S}_{60}(\text{AgI})_{10}$ organischen Dämpfen ausgesetzt und ihre Sorptionseigenschaften untersucht. Ammoniak bewirkt im Vergleich zu den anderen Analysesubstanzen eine chemische Modifikation der Beschichtung. Folglich ist es möglich, die Prozesse der Chemisorption und Physisorption zu unterscheiden. Die Modifizierung des Cantilever mit einer Chalkohalidglasschicht führt zu einer maßgeblichen Verbesserung der Empfindlichkeit des Cantilever (um etwa das 10fache). Innerhalb von fünf Wochen intensiver Nutzung nahm die Sensorempfindlichkeit exponentiell ab.

Die Mikrocantilever wurden auch mit üblichen organischen Polymeren beschichtet. Dabei kamen verschiedene Beschichtungsmethoden zur Anwendung und wurden analysiert. Solche organischen Polymere sind unter anderem Polymethylmethacrylat (PMMA),

Polydimethylsiloxan, Polyvinylpyridin, Styrenacrylonitrilcopolymer, Formvar™, Vinylchloridvinylacetatcopolymer und Fotolack AZ1518. Als Beschichtung beeinflussen sie die Resonanzeigenschaften der Cantilever. Durch das Heizelement auf dem Cantilever, welches der Schwingungsanregung dient, werden sie nicht nachweislich beeinträchtigt. Der Nachweis von Analysesubstanzen mit Polymerschichten erwies sich als reversibel und reproduzierbar. Zudem wurden unterschiedlich beschichtete Cantilever gleichzeitig einer Analysesubstanz ausgesetzt. Die Beschichtungen bestanden aus Polydimethylsiloxan, Polyvinylpyridin und Kohlenstoffnitrid in zwei verschiedenen Dicken. Als Analysesubstanzen strömten Dämpfe von Wasser, Ethanol, Methanol, 2-Propanol, wie auch von Zweistoffgemischen Methanol/ 2-Propanol und Methanol/Wasser durch die Messzelle. Die dickere Kohlenstoffnitridschicht verursacht ein größeres Antwortsignal. Die Erholungszeit, d.h. die Zeit, in der kein Dampf mehr strömt und sich die physisorbierten Substanzen allmählich lösen, hängt von der Dampfkonzentration und der Funktionsschicht ab und variiert dementsprechend stark. Diese zusätzliche Information kann als weiterer Parameter in den chemischen Nachweisprozess eingebunden werden.

Erstmalig können Ergebnisse zu Cantilevern mit Funktionsschichten aus tert-Butylcalixaren, Resorcinaren und phosphorierte Calixarene vorgestellt werden. Außerdem sind die Struktur-, Immobilisierungs- und Sorptionseigenschaften der Calixarenschichten und Beschichtungsmethoden beschrieben. Es erfolgten Versuche zum Nachweis von Dämpfen aus Wasser, Ethanol, Methanol, 2-Propanol, Aceton, Ammoniak und einigen Sorten Spirituosen. Der Einfluss sowohl von Hydroxyl- als auch Alkylgruppen, welche an das Calixaren gebunden sein können, wurde analysiert. Zum Vergleich waren Quarzkristallmikrowaagen (QCM) mit Calixarenen beschichtet. Calixarenschichten weisen eine höhere Selektivität als alle anderen untersuchten Schichten auf.

Aus den präsentierten Ergebnissen lässt sich schlussfolgern, dass Cantilever mit integriertem Aktor und Sensor die Basis für die nächste Generation (bio-)chemischer Sensoren darstellen.

Content

Chapter 1. Introduction and motivation	1
1.1. Sensors; chemical and biochemical sensors and their arrays	1
1.2. Microcantilever-based chemical sensors	5
1.3. Motivation and outline of the thesis	8
Chapter 2. Self-actuated piezo-resistive cantilever transducer	10
2.1. Static bending mode	12
2.2. Dynamic resonant mode	16
2.2.1. Eigenfrequencies of a vibrating cantilever	17
2.3. Mass detection theory	22
2.4. Experiments on higher order modes operation.....	28
2.5. Mass resolution limitations.....	31
2.5.1. Intrinsic cantilever noises	32
2.5.2. Extrinsic Johnson noise	34
2.6. Noise subtraction using a referent channel with uncoated cantilever.	35
2.7. Temperature dependencies	36
2.8. Pressure dependencies	38
2.8.1. Q-factor of microcantilevers.....	39
2.8.2. Experimental results on damping phenomena.....	43
2.9. Actuation and detection techniques for microcantilevers.....	45
2.9.1. Detection methods	45
2.9.1.1. Integrated piezo-resistive read-out	46
2.9.2. Excitation methods	48
2.9.2.1. Integrated bimorph actuator.....	49
2.9.3. Piezo-resistive detection principles: offset voltage, frequency shift, phase shift..	55
2.9.3.1. Principle of phase-shift detection in cantilever sensors	56

2.9.3.2.	Simulation of microcantilever's amplitude and phase spectra	61
2.9.3.3.	Calibration of the phase-shift response	65
Chapter 3.	Experimental set-up	68
3.1.	Measurement cell for single cantilever investigations	69
3.2.	Measurement cell for 4 cantilever array investigations.....	71
3.3.	Measurement cell for 8 cantilever array investigations.....	72
3.4.	Gas sampling station.....	74
3.5.	Measurement electronics and acquisition software	76
Chapter 4.	Sorption-induced effects and their influence on the cantilever operation	81
4.1.	Overview of sorption models	82
4.1.1.	The first sorption model	84
4.1.2.	The second sorption model.....	85
4.1.3.	The third sorption model	85
4.2.	Adsorption onto cantilevers coated with silicon oxide films	86
4.3.	Investigation of chemical and physical adsorption with a chalcogenide-coated cantilever transducer.....	93
Chapter 5.	Functionalization of the cantilevers with organic coatings.....	100
5.1.	Investigations on microcantilevers functionalized with organic polymers	100
5.2.	Calixarenes as novel functionalization materials	111
Chapter 6.	Conclusion and outlook.....	123
References	126
Abbreviations	132
List of publications prepared during PhD work	134
Acknowledgements	136

Chapter 1.

Introduction and motivation

1.1. *Sensors; chemical and biochemical sensors and their arrays*

Sensors designate for all instruments suitable for the technical measurement of physical, chemical or biological quantities. These instruments are capable of converting the generally non-electrical parameters into electronic-compatible signals. *Sensor technology* encompasses many details in order to cover the vast range of market-oriented applications. According to the form of energy in which a measured quantity is received and generated, there are six signal domains [1, 2], namely:

- **mechanical** (e.g., length, area, volume, all time derivatives such as linear/angular velocity/acceleration, mass flow, force, torque, pressure, acoustic wavelength and intensity);
- **thermal** (e.g., temperature, (specific) heat, entropy, heat flow, state of matter);
- **electrical** (e.g., voltage, current, charge, resistance, inductance, capacitance, dielectric constant, polarization, electric field, frequency, dipole moment);
- **magnetic** (e.g., field intensity, flux density, magnetic moment, permeability);
- **radiant** (e.g., intensity, phase, wavelength, polarization, reflectance, transmittance, refractive index);
- **(bio-)chemical** (e.g., composition, concentration, reaction rate, pH value, oxidation/reduction potential).

(Bio-)chemical sensors are (miniaturized) devices, which convert a chemical state into an electrical signal [3]. Fundamental arrangement of a typical chemical and biochemical sensor to detect atoms, molecules, or ions (“particles”) in the gas or liquid phase is shown in Fig. 1.

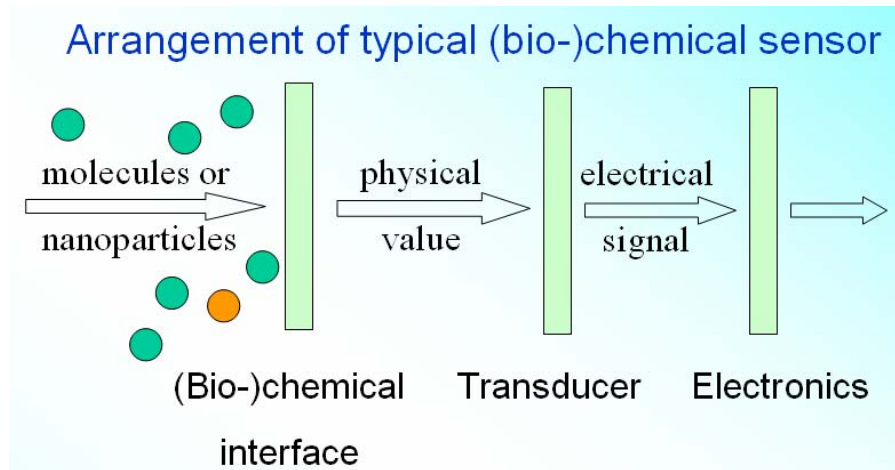


Fig. 1. General concept of a (bio-)chemical sensor.

A chemical state is determined by the different concentrations, partial pressures or activities of particles such as atoms, molecules, ions, or biologically relevant compounds to be detected in the gas, liquid, or solid phase. Common definitions of amounts of chemical species in gases include:

1) *Particle concentration*

number of particles of gas “*i*” per total number of particles *, e.g.

$$1\% = 1:10^2$$

$$1 \text{ ppm} = 1:10^6$$

$$1 \text{ ppb} = 1:10^9$$

2) *Mass concentration* $\rho_i = m_i / V$

(mg/m³)

mass of gas “*i*” per $V = 1 \text{ m}^3$ of the gas phase

3) *Partial pressure*

(Pa, mbar, Torr)

the partial pressure p_i of the component “*i*” is $p_i = (n_i / \sum n_i) \cdot p_{\text{tot}}$ with n_i as the number of moles of component “*i*”, $\sum n_i$ as the total number of moles of all components, and p_{tot} the total pressure.

* For instance, 1 m³ of air at 20° C and normal atmospheric pressure 101325 Pa contains $2.5 \cdot 10^{25}$ molecules. Saturated water vapour pressure under such conditions is calculated to be 1289 Pa, which corresponds to $3.2 \cdot 10^{23}$ molecules per m³. It means that water concentration in air is 12723 ppm.

The chemical state of the environment with its different compounds determines the complete analytical information. The different types of (bio-)chemical sensors may be classified according to the different sensor properties used for the particle detection. These properties (Tab. 1) change upon variations in the composition of chemical species interacting with the sensor.

Transducing physical values	Sensor classification
Masses	Mass sensitive sensors
Conductivities	Electronic conductivity sensors
Voltages, currents	Liquid electrolyte sensors
	Solid electrolyte sensors
Potentials	Field effect sensors
Capacities	Electronic capacitance sensors
Heats	Calorimetric sensors
Optical constants	Optochemical sensors

Tab. 1. (Bio-)chemical sensor classification according to the transducing physical properties.

Chemical sensors have become an ideal tool for performing real-time monitoring of both chemical and biochemical species. A chemical sensor incorporates the usage of various technologies from synthetic chemistry to surface analysis technologies.

Chemical sensor arrays have found a widespread use for biological and chemical recognition in a growing number of applications. They include: drug discovery and life sciences research; food analysis; fragrance and flavour analysis; chemical industry; medical diagnostics (e.g. detection of diseases in breath analysis); agriculture; environmental monitoring; security devices; detection of hazardous and explosive substances; study of chemical reactions or host-guest interactions on surfaces; criminalistics; etc.

Typical advantages of chemical sensors in comparison with conventional spectroscopy methods are: faster responses, portability, much lower prices.

A vapour-sensitive chemical recognition system, which detects volatile compounds with cross-reactive sensor arrays and interprets their responses with pattern recognition software, is usually referred to as a smart odour analyser or “electronic nose”. Researches in this area involve the search and investigation of novel sensing techniques, approaches and materials in order to improve recognition abilities of “electronic noses” along with reduction of their prices. At the same time, the odour-sensing concept remains the same: there is a chemical sensor array, where each sensor element is individually coated with an organic sensitive layer with specific sorption sensitivity (Fig. 2).

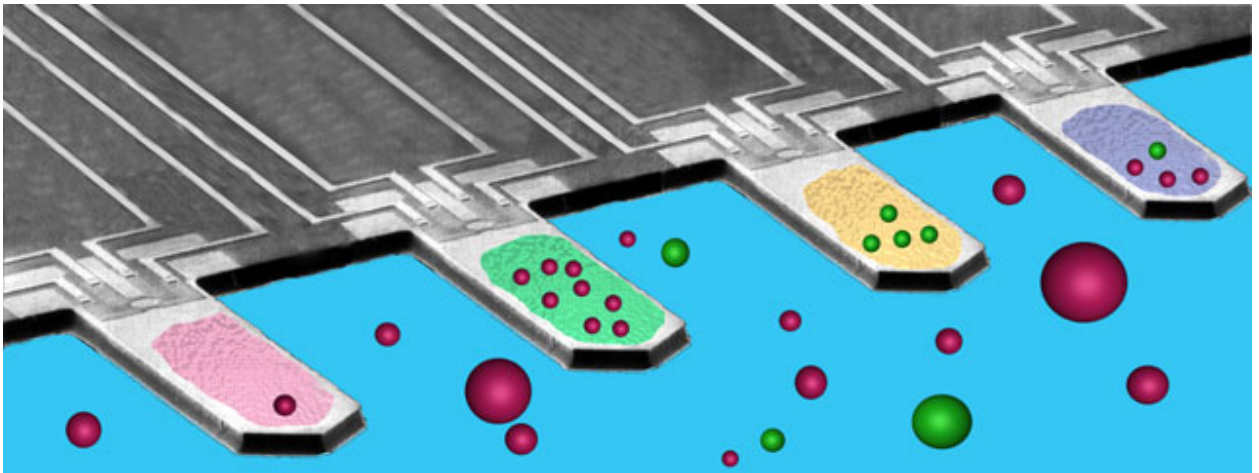


Fig. 2. Cantilever-based “electronic nose”.

Thus, exposition of “electronic nose” to a gaseous mixture results in individual electronic response from every sensor in the array. Qualitative and quantitative analysis of individual components in the gaseous mixture is then possible by applying pattern recognition software. Furthermore, sensors in the array may differ from each other not only by the coating (which is shown as “(Bio-)chemical interface” in Fig. 1), but also by the transducer type.

Beginning of artificial olfaction as a new technology was announced in Nature in 1982 [4], however the expression ‘electronic nose’ appeared for the first time in 1988. Nowadays commercial electronic nose instruments are produced by many manufacturers. They implement different chemical sensors in an array, such as:

- metal-oxide-semiconductor MOS-sensors (Alpha M.O.S., AppliedSensor Group, Lennartz Electronic, Daimler Chrysler Aerospace, Element Ltd, Forschungszentrum Karlsruhe, Marconi Applied Technologies (now ELV Technologies), WMA Airsense Analysentechnik GmbH);
- conducting polymers, e.g. composite polymer-carbon black polymers, conducting oligomers, and phthalocyanine-based sensors (Alpha M.O.S., Bloodhound Sensors Ltd, Cyrano Sciences Inc, Marconi Applied Technologies, Osmetech plc, OligoSense n.v.);
- surface acoustic wave SAW-sensors (Alpha M.O.S., Daimler Chrysler Aerospace, Electronic Sensor Technology Inc, Forschungszentrum Karlsruhe, Microsensor Systems Inc);
- quartz-crystal microbalances QCM-sensors (AppliedSensor Group, Daimler Chrysler Aerospace, HKR Sensorsysteme GmbH, Lennartz Electronic, Marconi Applied Technologies, Quartz Technology Ltd, Quality Sensor Systems Ltd).

1.2. *Microcantilever-based chemical sensors*

There is a considerable interest to microcantilevers as high-sensitive, express and low-cost detectors for monitoring of a specific substance in many applications listed above. By coating the cantilever surface with a chemical layer that selectively adsorbs or binds a given target substance, a cantilever can be converted into a highly sensitive and selective chemical or biochemical sensor.

When the cantilever comes “in contact” with the target substance, it reacts with a mechanical response: the cantilever bends due to surface stress and changes its resonance frequency due to the additional mass load. The tiny dimensions of the cantilever account for its extremely high sensitivity.

Using an array of microcantilevers coated with different adsorbents and involving computational analysis techniques, it is also possible to create an “electronic nose”, which is capable to recognize smells. Such the way, our increasing effort has been spent into the development of micromechanical cantilever-based chemical sensors. The main motivation for the application of cantilevers as chemical or biochemical sensors is based on the advantages, which are offered by their miniaturization, high sensitivity, and the possibility of integration of transducer, actuator and read-out unit on the same chip. For the application as a chemical sensor, one side of the cantilever has to be coated with a sensitive layer, which transduces a physical process or a chemical reaction into a nanomechanical response. When the sensitive layer is exposed to an analyte, the molecular absorption of the analyte into the layer causes a change of the effective mass of the cantilever/coating structure. In addition, the molecular adsorption of the analyte onto the layer could induce tensile or compressive stresses and also affect the stiffness of the cantilevered structure. Both effects result in a variation of the resonance frequency and /or a static deflection (bending) of the cantilever. By measuring the resonance frequency shift, the cantilever can register a wide range of analyte concentrations in the environment. In order to recognize a variety of analytes or different individual components in a mixture of analytes, an array of cantilevers can be used in which each cantilever is coated with a different material showing specific sorption sensitivity to these analytes (Fig. 2).

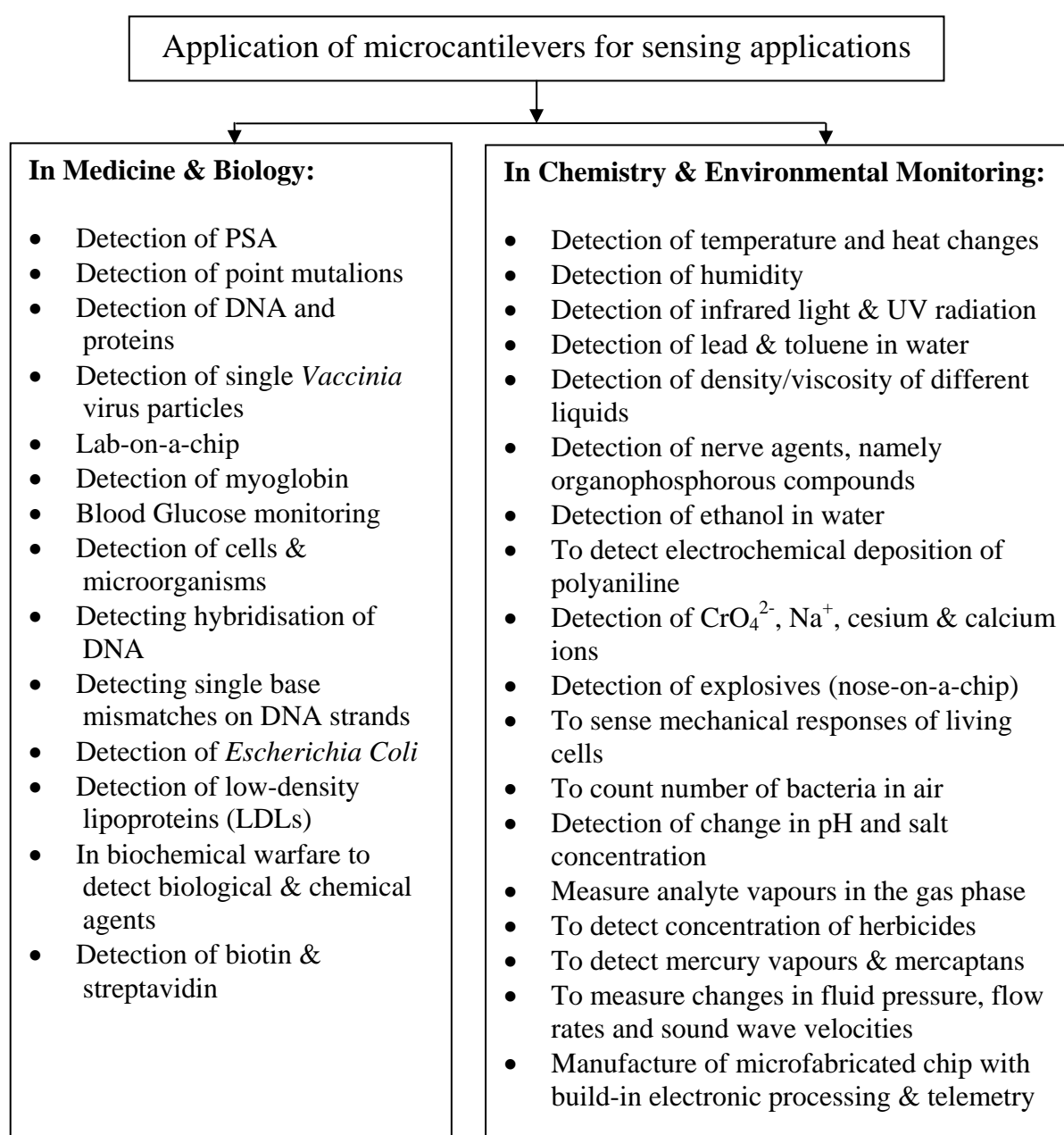
Besides our research group, there are other research consortia dealing with cantilever investigation for gas-sensing applications:

- 1) Swiss company Concentris from Basel in collaboration with IBM Research Laboratory in Zürich;
- 2) Oak Ridge National Laboratories, USA;
- 3) Danish company Cantion in collaboration with TU Denmark.

In general, cantilever responses are recorded by optical scheme, which can detect cantilever deflections in the sub-angstrom region. However, for many applications it is advantageous to have an integrated read-out mechanism, which requires less adjustment and alignment. For this reason, the sensors used in this study were rectangular layered Si/SiO₂ cantilevers (450 μm long and 150 μm wide) with an integrated piezo-resistive full Wheatstone bridge read-out. Such integrated cantilever read-out configuration was pioneered by Ivo Rangelow et al. in 1994 [5]. The fabrication process of these cantilevers is a modification of the double-sided silicon micromachining process developed for manufacturing of piezo-resistive AFM sensors, applying standard CMOS processing. In order to achieve a piezo-resistive deflection sensitivity of the cantilever better than $6 \times 10^{-5} \frac{\Delta R}{R}$ (change in resistance divided by total resistance) per nanometer beam deflection, very shallow piezo-resistors (50 nm under the surface) were fabricated. A detailed description of the technology for the fabrication of cantilevers with an integrated piezo-resistive read-out has been previously published, e.g. [6, 7]. Our approach implies also an integrated thermal actuation based on the bimetallic effect [7, 8]. Such combination of integrated read-out and actuation mechanisms on the sensor, which is fully compatible with standard silicon technology, reveals powerful possibilities for miniaturization, mass production, reduction of the price, etc.

The field of cantilever sensors has been extensively developed in recent years [9-14]. The main topics covered in the recent publications include the following: detection of vapours and volatile compounds (e.g., HF vapour) using individual microcantilevers operated in beam deflection static mode [15-18]; gas-phase sensing applications for solvents using piezo-resistive cantilevers [19-29]; biochemical applications in static mode in liquids [30-32] (e.g., as a glucose sensor); and C-reactive protein detection using dynamic-mode piezo-resistive microcantilevers [33, 34]. Several efforts have investigated the usability of microcantilever sensors as detectors for explosives [35-37] or *Escherichia Coli* bacteria [38, 39]. A pH sensor using hydrogel coatings [40, 41] has been suggested, as has the observation of electrochemical redox reactions using microcantilevers [42]. The theory of molecule adsorption on cantilevers has been investigated in several publications [43-47], whereas the bending, calibration, and curvature of cantilevers has been studied experimentally [48-50]. A new strategy to grow polymer brushes on the surface of microcantilevers has been proposed [51]. Others have described the production of polymer microcantilevers [52]. Torsional or lateral resonance modes could also be exploited for improved mass sensing in dynamic mode [53, 54]. Nanowire electrodes attached to cantilevers in an array could be used for local multiprobe resistivity measurements [55], and two-dimensional microcantilever arrays have been suggested for multiplexed biomolecular analysis [56].

Chemical sensor applications of resonant cantilevers have included humidity sensors [57, 58] or the detection of mercury vapours [59]. Complementary metal oxide semiconductor (CMOS) cantilevers coated with chemically sensitive polymers have previously been used for the detection of volatile organic compounds [57, 60-64]. A miniaturized system with an array of coated cantilevers for the simultaneous detection of hydrogen and mercury vapours was reported in [65]. Quantitative detection of the components of a binary mixture was demonstrated by ETH group (Switzerland) and by Kim et al. [66] Cantilevers can be included in application-specific chemical sensor systems [60] along with other types of CMOS-based microtransducers such as capacitors [67, 68] or microcalorimeters [69]. By visual demonstration, most common microcantilever-based sensor applications are listed in Tab. 2.



Tab. 2. Summary of the microcantilever applications for (bio-)chemical field [70].

A broadening cantilever sensor application in medicine concerns breath sample characterization as possible indication for diseases [71]. Before using modern diagnosis tools medical doctors examined patient's breath to detect diseases, as certain diseases can be recognized by study of exhaled air. Examples of such findings are:

- *diabetes mellitus* (type II diabetes), a severe, chronic form of diabetes caused by insufficient production of insulin and resulting in abnormal metabolism of carbohydrates, fats, and proteins. This disease involves acetone to be present in patient's breath.
- *uraemia*, a toxic condition resulting from kidney disease in which there is retention of waste products in the bloodstream normally excreted in the urine. A compound found in patient's breath associated with uraemia is dimethylamine.

Another recently arisen biosensor application area for microcantilevers is express detection of fungal contaminants (moulds), e.g. spores of *Aspergillus niger* [72, 73]. The spores can be detected *in situ* within ~ 4 h instead of ~ 5 days of laboratory exploration of the growing eukaryotic colony.

The mass resolution of the cantilevers is in the range of a few picograms [57, 60, 62, 74-77]. However, attogram detection with nanosized cantilevers in vacuum has been already reported [53]. From a scientific point of view, the challenge lies in optimizing cantilever sensors to improve their sensitivity until the ultimate limit is reached, which may be the nanomechanical detection of individual molecules.

Cantilever array (bio-)chemical sensing and recognition is based on convergence of physics, chemistry, biology, engineering, medicine, computer sciences.

1.3. Motivation and outline of the thesis

The presented work is aimed for development and investigation of chemical gas sensors and their arrays based on microcantilever transducers. The presented work had been divided into several research aspects, which were structured and described in six independent chapters of this thesis correspondingly.

First chapter has been an introduction into chemical gas sensor technology and the cantilever-based chemical sensing.

Second chapter describes implementation of microcantilever as a mass-sensitive transducer for chemical sensor. Integrated piezo-resistive read-out, integrated bimorph actuator, different operational modes and techniques are discussed.

Third chapter describes measurement set-up, its engineering solution, electronics and software as well as several implementations of the measurement cell.

Fourth chapter discusses influence of sorption-induced effects on cantilever operation. It summarises the research carried out on single cantilevers with inorganic coatings. Adsorption abilities of uncoated cantilevers are considered and experimentally measured. Especially interesting are experiments with a cantilever coated with a chalcogenide glass. Chemical modification of the coating with ammonia vapours made it possible to illustrate chemical and physical sorption processes.

Fifth chapter is devoted to organic application-specific functionalization materials. Polymer-coated cantilevers and their arrays were exposed to volatile organic compounds (VOCs) and their binary mixtures. Sensor performances of cantilevers functionalized with organic coatings towards different volatile analytes is demonstrated. Special emphasis is given to calixarenes as promising nanostructured material for molecular recognition and sensor applications.

Sixth chapter is a conclusion emphasising the most important results, which have been obtained during fulfilment of this work, as well as future prospects for the described technology.

Chapter 2.

Self-actuated piezo-resistive cantilever transducer

Microcantilever is a thinned silicon plate (beam) with one end fixed and the other end free. Depending on the projected application field, the microcantilever can also contain built-in read-out, actuation, and pre-processing circuits. For instance, microcantilevers designed and fabricated at the University of Kassel in the frame of the TASNANO EU-Project contain implanted piezo-resistive Wheatstone bridge as the read-out unit, meander-shaped aluminium heater as the thermal bimorph actuator, and the gold pad for the chemical (biological) functionalization, as shown in Fig. 3. General view of such a microcantilever used for investigations in this work is presented in Fig. 4.

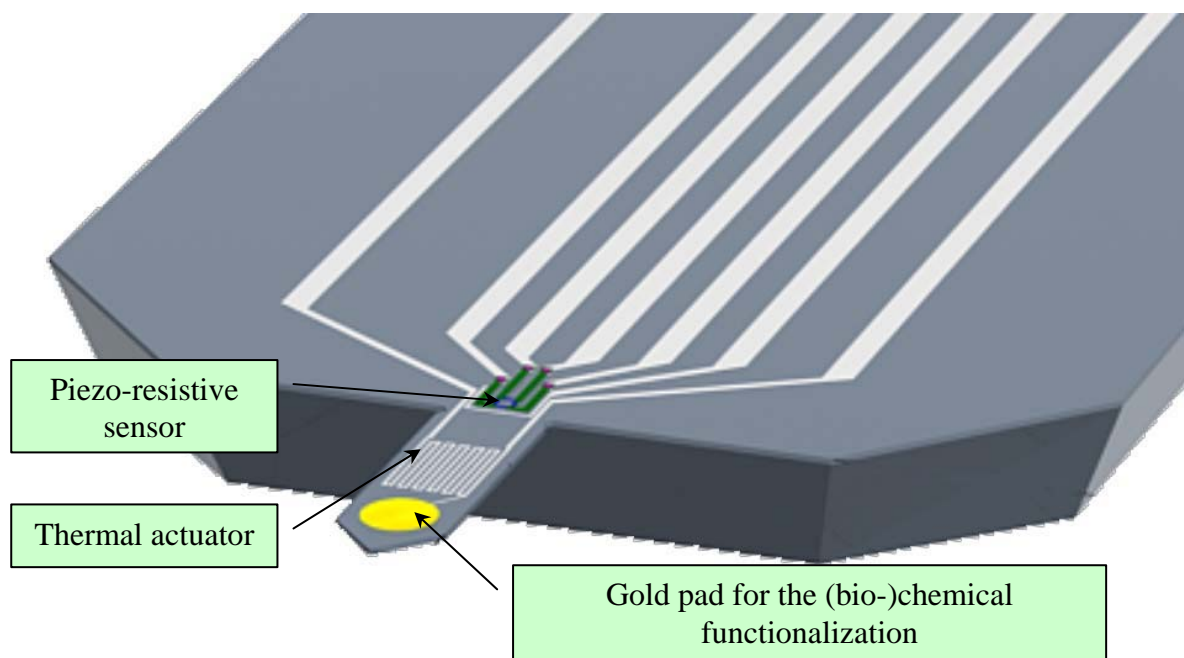


Fig. 3. Sketch layout of the investigated TASNANO-cantilevers.

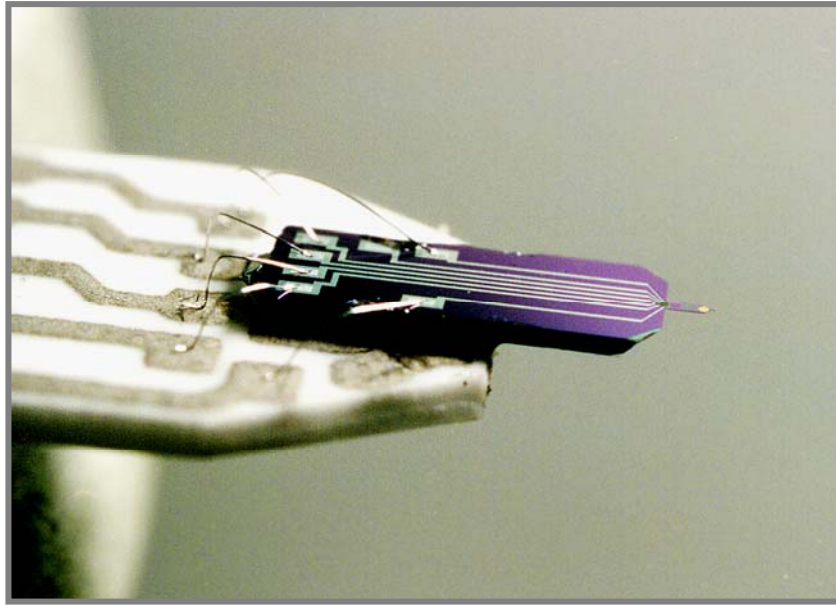


Fig. 4. Single microcantilever with integrated read-out and actuation. The TASNANO -cantilever beam dimensions are: length $l = 450 \mu\text{m}$, width $w = 150 \mu\text{m}$, thickness $h = 4 \mu\text{m}$.

Conversion of input stimuli into output signals by cantilever transducers is associated with a number of transduction mechanisms. Depending on the measured parameter (structural deformations or resonance frequency) the mode of sensor operation can be referred to as either *static (bending) mode* or *dynamic (resonant) mode*. Each of these modes, in turn, can be associated with different transduction scenarios, as depicted in Fig. 5. Analogous to contact and tapping modes of AFM, cantilever-based sensors also involve measurements of cantilever deflections, resonance frequencies and, in some cases, damping characteristics. However, the mechanisms that translate various components of a physical, chemical, or biological environment into these parameters are generally different from the mechanisms that are operative in AFM [78]. Static cantilever deflections can be caused by either external forces exerted on the cantilever (as in AFM) or intrinsic stresses generated on the cantilever surface or within the cantilever. While cantilever microfabrication technology is capable of producing nearly stress-free suspended beams, additional intrinsic stresses may subsequently originate from thermal expansion, interfacial processes and physicochemical changes. Cantilever sensors operating in the dynamic mode are essentially mechanical oscillators, resonance characteristics of which depend upon the attached mass as well as viscoelastic properties of the medium. For instance, adsorption of analyte molecules onto a resonating cantilever results in lowering of its resonance frequency due to the increased suspended mass of the resonator.

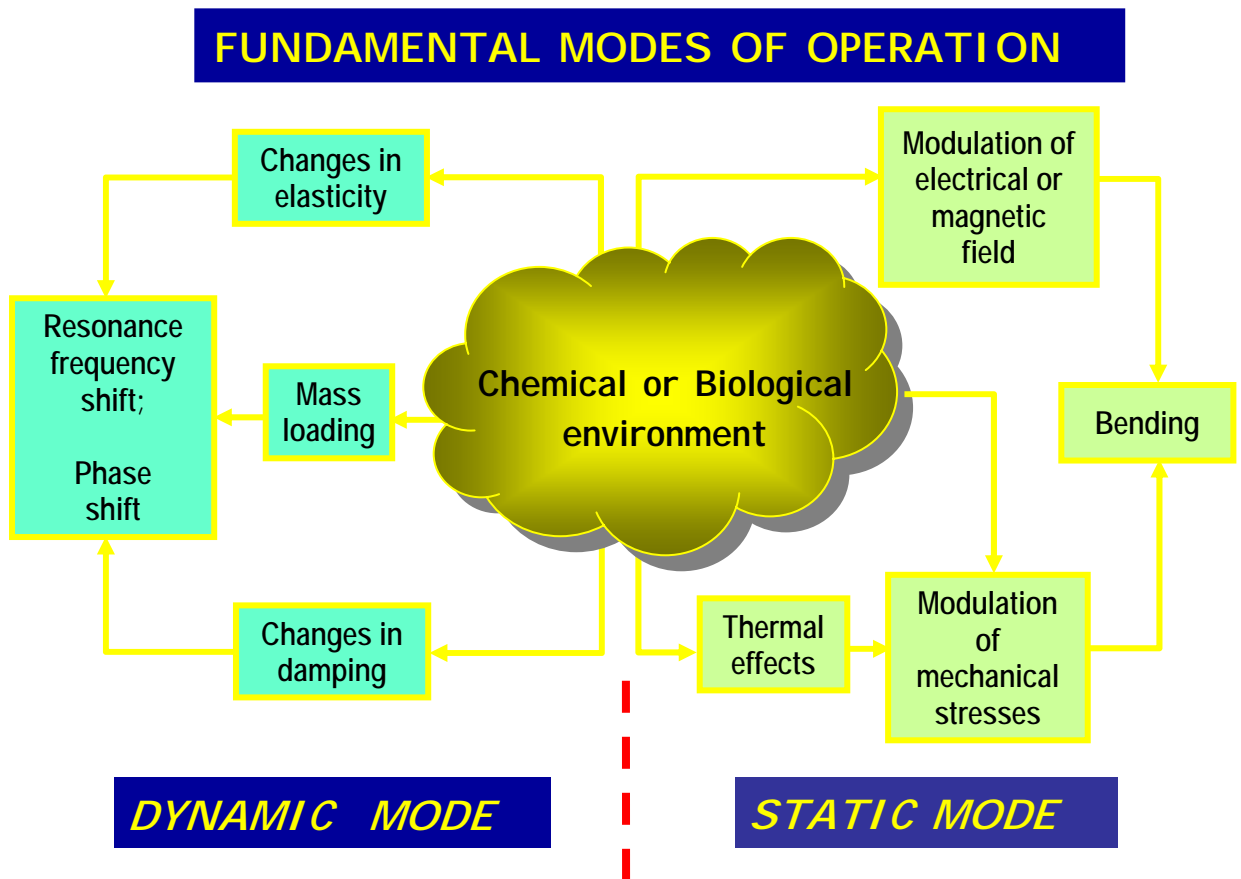


Fig. 5. Fundamental modes of operation [9].

This chapter is to describe both modes of cantilever operation in more detail. Some particular, advanced, and innovative techniques will be featured in separate paragraphs.

2.1. Static bending mode

This section is aimed at theoretical background of adsorption-induced stresses and definition of cantilever's spring constant, which will be widely used for further explanations. Fig. 6 introduces a cross sectional drawing of a cantilever along with some designations.

The most general relationship between the force exerted normally on the cantilever apex (F) and its displacement (Δz) can be defined using Hook's law:

$$F = -k \cdot \Delta z, \quad (1)$$

where k is spring constant of the cantilever beam, which denotes its elastic properties. This is a very important parameter for cantilever as a chemical sensor, because k is subject to change when functionalized cantilever interacts with some media.

In the absence of external gravitational, magnetic, and electrostatic forces, cantilever deformation is unambiguously related to a gradient of mechanical stress generated in the device.

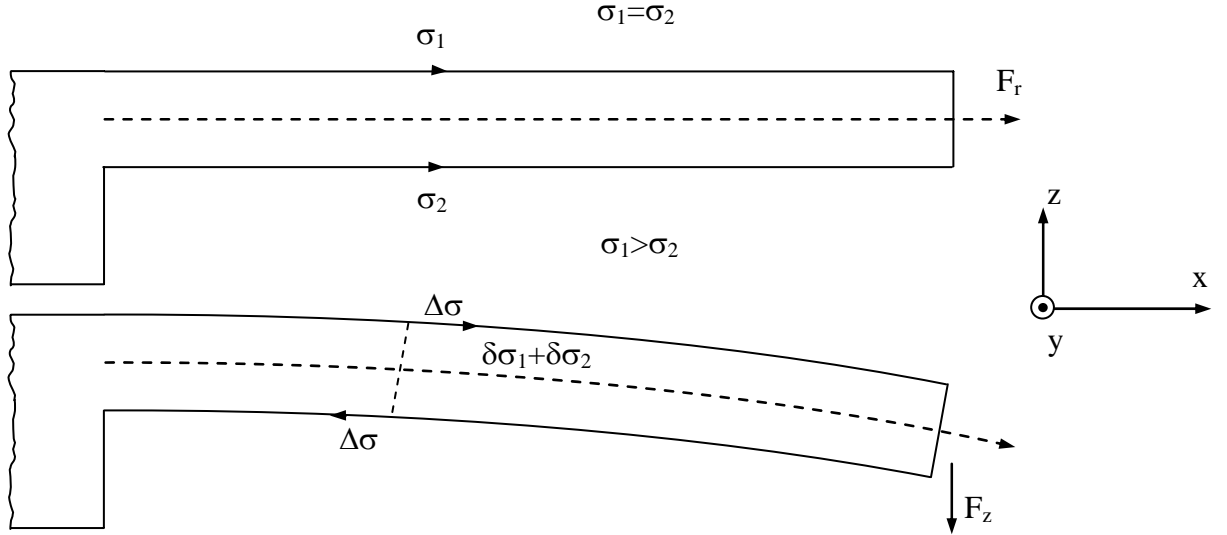


Fig. 6. Cross sectional drawing of a rectangular cantilever [79].

σ_1 and σ_2 – induced stresses on the top (σ_1) and bottom (σ_2) of the cantilever;

$$\Delta\sigma = \frac{d\sigma_1}{dz} + \frac{d\sigma_2}{dz} - \text{differential surface stress.}$$

Differential surface stress causes the cantilever with length l , width w , and thickness h to bend with the radius of bending R . A geometrical relation for R is [80]:

$$\frac{1}{R} = \frac{d^2z/dx^2}{[1 + (dz/dx)^2]^{3/2}} \approx \frac{3\Delta z}{2l^2}, \quad (2)$$

which for a small amount of bending may be simplified to [81]:

$$\frac{1}{R} \approx \frac{d^2z}{dx^2} \approx \frac{2\Delta z}{l^2} = \frac{M}{Y \cdot I}, \quad (3)$$

where R is furthermore related to the moment of the bent body (M), the moment of inertia (I) and the effective modulus of isotropic elasticity (Y) [81]:

$$Y = \frac{E}{1 - \nu^2}, \quad (4)$$

where E is Young's modulus and ν is Poisson's ratio for the substrate (for silicon $\nu = 0.27$).

The area moment of inertia for a rectangular cantilever can be calculated as:

$$I = \int_0^w \int_{-h/2}^{h/2} z^2 dz dy = \frac{wh^3}{12}, \quad (5)$$

where w is the width and h is the thickness of the cantilever.

If the bending moment is [79]:

$$M = \Delta\sigma \cdot w \cdot h/2, \quad (6)$$

then if cantilever length $l \gg w$, Hooke's law for small displacements can be re-written as:

$\frac{1}{R} \approx \frac{d^2 z}{dx^2} = \frac{M}{Y \cdot I} = \frac{\Delta\sigma \cdot w \cdot h \cdot (1-\nu^2) \cdot 12}{2 \cdot E \cdot w \cdot h^3}$, and finally we obtain "Stoney's equation", originally derived by Stoney and von Preissig [82, 83], which can in many cases accurately predict adsorbate-induced deformations of thin plates:

$$\boxed{\frac{1}{R} = \frac{6(1-\nu^2)}{Eh^2} \Delta\sigma}, \quad (7)$$

where R is the radius of microcantilever curvature, ν and E are Poisson's ratio and Young's modulus for the substrate, respectively, h is the thickness of the cantilever, and $\Delta\sigma$ is the differential surface stress. Knowledge of the radius of curvature R allows the tip displacement of a microcantilever with length l to be determined by:

$$\Delta z = \frac{1}{2} \frac{l^2}{R} = \frac{3l^2(1-\nu)}{Eh^2} \Delta\sigma. \quad (8)$$

The Stoney's equation can be also equivalently presented as:

$$\boxed{\Delta\sigma = \frac{Eh^2}{3l^2(1-\nu)} \Delta z}, \quad (9)$$

So, measuring the tip deflection like in AFM, one can derive the differential surface stress.

Now we are going to use Eq. (3) to calculate the spring constants for a cantilever. The cantilever is rigidly clamped on one side and is free on the other. It has a length, l , and a concentrated force, F , acting on the cantilever at a distance a from the clamped side. The moment, which is produced by the force acting on the cantilever, is given by [80]:

$$M = F(x - a). \quad (10)$$

By inserting Eq. (10) in (3) and solving the second order differential equation, the displacement Δz can be derived. Furthermore, by then setting $x=a=l$ we obtain:

$$\Delta z = -\frac{l^3}{3YI} F. \quad (11)$$

Now, we can insert Eq. (11) into Hook's law given by Eq. (1), and solve for k :

$$k = 3 \frac{YI}{l^3}. \quad (12)$$

Finally, assuming that $1-\nu^2 \cong 1$, and by substituting (5) in (12), the spring constant of a cantilever is calculated according to:

$$k = \frac{Eh^3w}{4l^3}. \quad (13)$$

Eq. (13) interrelates the cantilever's spring constant and its geometry along with its material properties. Hereafter, Eq. (13) will be used for calculation of spring constant k as measure of cantilever stiffness.

Such the way, the static mode considers bending of the cantilever through modulation of mechanical stresses due to either direct influence of the environment or thermal effects caused by this influence. In the latter case, the presence of analyte species can be detected due to the following phenomena:

- the heat associated with their adsorption on the transducer;
- the heat produced in the course of a subsequent chemical reaction on the cantilever surface.

Cantilever bending can also be driven by external gravitational, electrical or magnetic fields.

If the conversion of chemical energy into mechanical energy takes place directly, i.e. independently on the thermal effects, then the surface stress σ can be expressed by using the Shuttleworth equation [84]:

$$\sigma = \gamma + \frac{\partial \gamma}{\partial \varepsilon}, \quad (14)$$

where γ is the surface free energy. The surface strain $d\varepsilon$ is defined as the relative change in surface area $d\varepsilon = dA/A$. In many cases, the contribution from the surface strain term can be neglected and the free energy change approximately equals the change in surface stress.

In its own turn, the surface free energy γ (or interfacial tension) is interrelated with the amount of adsorbed molecules on the cantilever surface by the Gibbs adsorption equation [85]:

$$\Gamma = -\frac{C}{RT} \left(\frac{d\gamma}{dC} \right), \quad (15)$$

where Γ is excess of adsorption at an interface in a two-phase system, $d\gamma$ is the change in surface free energy and C is the concentration of the solute.

Eq. (14) and (15) are appropriate to describe molecular adsorption processes at different interfaces. Therefore, cantilever bending mechanism is compatible with many responsive phases and can function in both gas and liquid environments.

Despite the static cantilever bending is a result of direct adsorbate influence, it is rather difficult to estimate the adsorbed mass quantitatively because the surface coverage is basically not known. However, cantilever operation at its eigenfrequency, which is analysed in the next section, enables accurate calculation of the amount of molecules adsorbed.

2.2. Dynamic resonant mode

The dynamic mode of the cantilever operation considers motion of the cantilever beam, which can take place either with or without forced excitation. The forced excitation can be realised by alternated fields of electric, electromagnetic, thermal, or acoustic origin. Furthermore, minute sizes and mass of microfabricated cantilevers makes them susceptible to thermally induced noise, which has the same origin as Brownian motion of small particles in liquids. Therefore, cantilever sensors may operate in the resonant mode with or without external excitation.

The mechanically excited cantilevers require the presence of actuator, which causes the cantilever to vibrate. Practically, it can be achieved by either oscillating quartz crystal, which is in firm mechanical contact with the cantilever, or by integrated actuator employing bimorph effect, which is discussed in § 2.9.2.1. Normally, the actuator provides with periodic oscillations of the cantilever beam over certain frequency range near its natural or higher resonances. Alternatively, pulsed excitation of the cantilever or amplification of the Brownian motion of the cantilever beam (i.e. without forced excitation) gives also information on its frequency spectrum.

Gain-frequency or phase-frequency responses of the functionalized cantilever gathered over a time interval reflect chemical or biological stimuli exerted on the cantilever.

Resonance frequency shift of the cantilever under analyte exposition is mostly due to the additional mass loading, which is considered in the effective mass of a harmonic oscillator m_{eff} :

$$\omega = \sqrt{\frac{k}{m_{eff}}} . \quad (16)$$

However, adsorption-induced changes in the elasticity of the cantilever beam and damping of the cantilever (its Q-factor modulation) are other two significant mechanisms for resonance frequency modulation.

2.2.1. Eigenfrequencies of a vibrating cantilever

Dynamic resonant mode implies vibration of the cantilever beam, which is reflected by amplitude peaks in the output frequency spectrum of the cantilever. The eigenfrequencies spectrum contains peaks not only at the natural resonance of the cantilever, but also other peaks at the cantilever's higher resonance modes. Moreover, cantilevers excited with bimorph actuator exhibit additional satellite peaks at the half frequency of each eigenmode, as demonstrated experimentally in Fig. 7 and explained below in § 2.9.2.1.

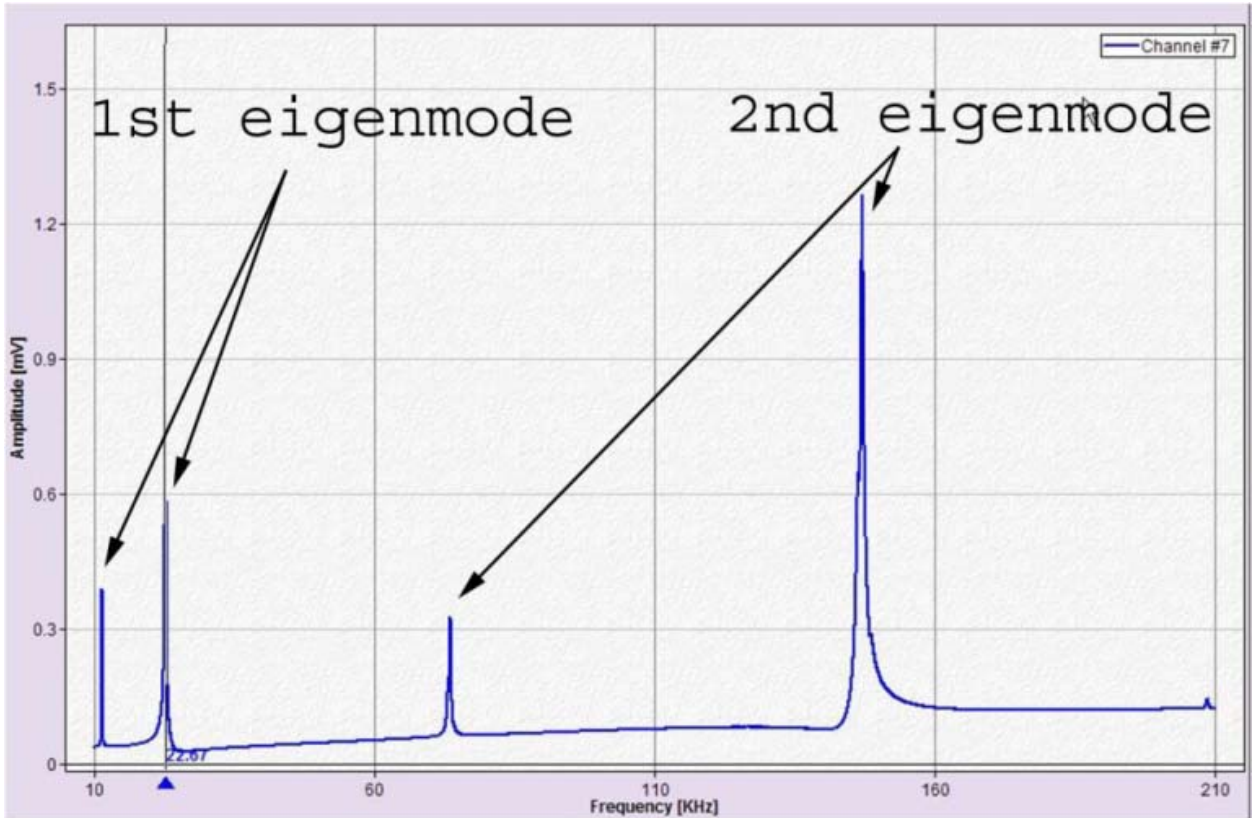


Fig. 7. Experimentally measured eigenfrequencies of an uncoated thermally excited cantilever.

Let's theoretically calculate eigenfrequencies of a *homogeneous and isotropic cantilever in vacuum*. Generally, the amplitude of the kinematic motion can have an influence on the eigenfrequency of the oscillator for the case of large cantilever deflections, where the motion of the beam is described by a nonlinear equation. However, we consider (and ensure experimentally) small beam deflections, where the response is linear.

First, we have the equation of motion of a beam in the transverse direction [53, 86]:

$$EI \frac{\partial^4 z(x,t)}{\partial x^4} + \rho A \frac{\partial^2 z(x,t)}{\partial t^2} = F, \quad (17)$$

where ρ and E are the mass density and the elastic modulus of the material of the lever, respectively, I is its moment of inertia, A is its cross-sectional area, F is an external force per unit length. For the rectangular cantilever we have $A=wh$ and $I = \frac{wh^3}{12}$, so that:

$$\frac{Eh^2}{12\rho} \frac{\partial^4 z(x,t)}{\partial x^4} + \frac{\partial^2 z(x,t)}{\partial t^2} = \frac{F}{\rho wh}. \quad (18)$$

Let's first assume $F = 0$:

$$\frac{\partial^4 z(x,t)}{\partial x^4} + \frac{12\rho}{Eh^2} \frac{\partial^2 z(x,t)}{\partial t^2} = 0. \quad (19)$$

Assuming time harmonic solutions of Eq. (19), we have:

$$z(x,t) = z(x)[\cos(\omega_n t + \theta)], \quad (20)$$

where ω_n is angular frequency of the n^{th} mode and θ is the phase shift. Then Eq. (19) can be rewritten as:

$$\frac{d^4 z(x)}{dx^4} - \kappa_n^4 z(x) = 0, \quad (21)$$

where the modal parameter

$$\kappa_n^4 \equiv \omega_n^2 \frac{12\rho}{Eh^2}. \quad (22)$$

Expression (21) is a fourth order differential equation, which when solved for the appropriate boundary conditions, will allow us to find the radial frequency ω_n . The general solution to Eq. (21) is:

$$z(x) = B_1 \sin \kappa_n x + B_2 \cos \kappa_n x + B_3 \sinh \kappa_n x + B_4 \cosh \kappa_n x, \quad (23)$$

where B_1 , B_2 , B_3 , and B_4 are arbitrary constants. Furthermore, the boundary conditions for an oscillating cantilever are [87]:

$$z(0) = \frac{dz(0)}{dx} = \frac{d^2 z(l)}{dx^2} = \frac{d^3 z(l)}{dx^3} = 0. \quad (24)$$

For the boundary conditions we get a homogeneous system of four linear equations for the unknown B_1 , B_2 , B_3 , and B_4 . This system has a nontrivial solution only if:

$$\cos \kappa_n l + 1/\cosh \kappa_n l = 0. \quad (25)$$

Through numerical calculation, the lowest values of $\kappa_n l$ can be calculated as:

$$\kappa_1 l = 1.8751, \kappa_2 l = 4.6941, \kappa_3 l = 7.8548, \kappa_4 l = 10.9956. \quad (26)$$

For $\kappa_n l \gg 1$ we get:

$$\kappa_n l = \pi(n - \frac{1}{2}). \quad (27)$$

Further, the eigenfrequencies of the cantilever are defined from the definition of κ (22) by:

$$f_n^{vac} = \frac{\kappa_n^2 h}{2\pi} \sqrt{\frac{E}{12\rho}}. \quad (28)$$

Finally, since we have already obtained tabulated values of $\kappa_n l$, Eq. (28) can be equivalently presented as:

$$f_n^{vac} = \frac{(\kappa_n l)^2 h}{2\pi l^2} \sqrt{\frac{E}{12\rho}}, \quad (29)$$

where $\kappa_n l$ value for the corresponding eigenmode should be taken from Eq. (26).

The eigenfrequencies are not dependent on w unless the cantilever oscillations are not damped by a medium. For silicon cantilever with $l = 450 \mu\text{m}$ and $h = 4 \mu\text{m}$ first three eigenmodes in vacuum were calculated with Maple ® to be equal:

$$\begin{aligned} f_1 &= \mathbf{27.065 \text{ kHz}}, \\ f_2 &= \mathbf{169.615 \text{ kHz}}, \text{ and} \\ f_3 &= \mathbf{474.930 \text{ kHz}}. \end{aligned}$$

Their ratios are independent on the cantilever dimensions, so that:

$$\frac{f_2}{f_1} = 6.267, \text{ and } \frac{f_3}{f_1} = 17.548.$$

As only the first eigenfrequency of a cantilever is experimentally measured, these values allow quick estimation of the higher modes position in the cantilever spectrum. It is helpful for experimental cantilever characterisation, because time-consuming scan over the whole cantilever spectrum can be avoided.

Dependencies for the 1st mode natural resonance frequency versus cantilever length (ranged between 300...600 μm ; for cantilever thickness $h = 4 \mu\text{m}$) and versus cantilever thickness (between 1...10 μm , for cantilever length $l = 450 \mu\text{m}$) are presented in Fig. 8:

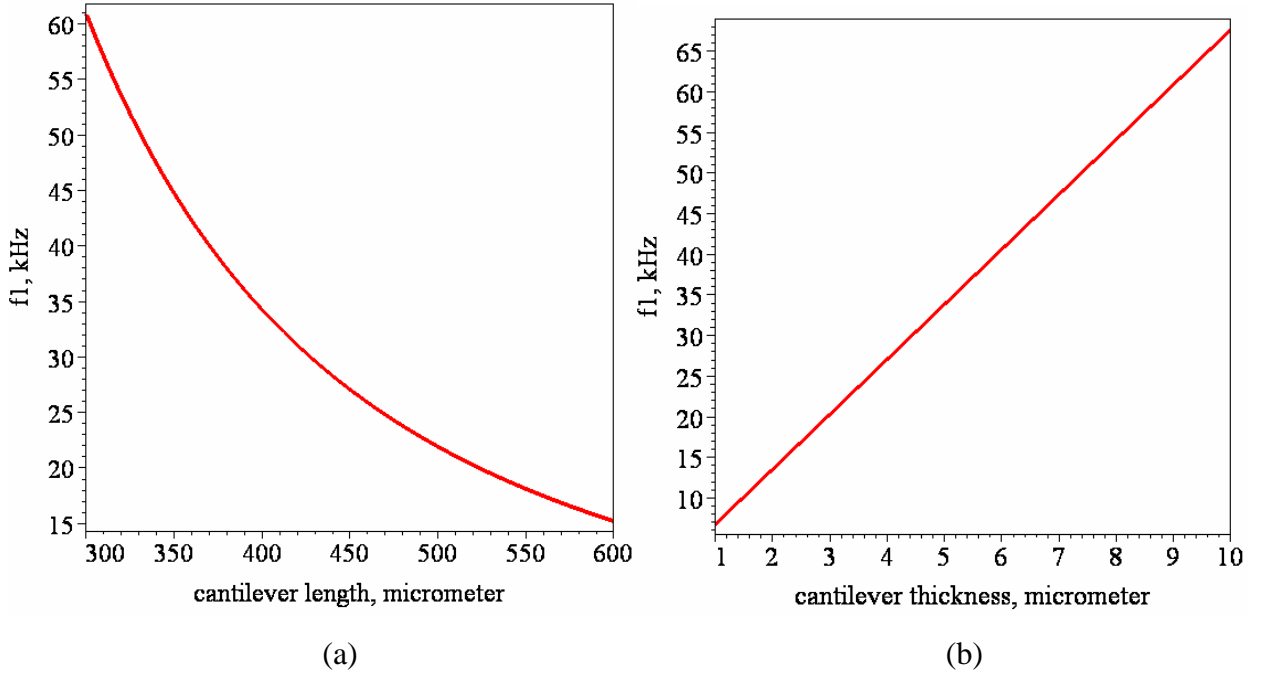


Fig. 8. Dependence of natural resonance frequency on the cantilever dimensions $f_1 \sim \frac{h}{l^2}$ versus cantilever length (a), and cantilever thickness (b).

Cantilever transducers operating in gases or in vacuum can be treated as weakly damped mechanical oscillators. As a first approximation, it can be assumed that the cantilever apex displacement is directly proportional to the force exerted on the cantilever apex. Then, a simplified model of a resonating cantilever transducer can be based on the Hook's law applied to a rectangular leaf spring with an effective suspended mass m_{eff} and a spring constant k , as has been already introduced in Eq. (16).

The static mode spring constant k can be expressed through the cantilever dimensions and its Young's modulus according to Eq. (13). The effective suspended mass of a cantilever can be related to the total mass of the suspended portion of the beam:

$$m_b = \rho h w l \quad (30)$$

through the relationship:

$$m_{eff} = n_n \cdot m_b, \quad (31)$$

where n_n is a geometric parameter of the n^{th} mode of the cantilever vibration.

Let's correspond Eq. (16) to (29). By definition of the spring constant, which is given by Eq. (13), and by using Eq. (30) and (31), Eq. (16) can be rewritten as:

$$f_n = \frac{1}{2\pi} \sqrt{\frac{Ewh^3}{4l^3 n_n \rho h w l}} = \frac{h}{4\pi d^2} \sqrt{\frac{E}{n_n \rho}} = \frac{\sqrt{12}}{2\sqrt{n_n}} \cdot \frac{h}{2\pi d^2} \sqrt{\frac{E}{12\rho}} = \sqrt{\frac{3}{n_n}} \cdot \frac{h}{2\pi d^2} \sqrt{\frac{E}{12\rho}}. \quad (32)$$

From (29) and (32) we have that:

$$(\kappa_n l)^2 = \sqrt{\frac{3}{n_n}}, \quad (33)$$

which equivalently means that:

$$n_n = \frac{3}{(\kappa_n l)^4}. \quad (34)$$

Using $\kappa_n l$ values from (26) we get the following geometric parameters for the effective masses of the rectangular cantilever in the first three modes of interest:

$$n_1 = \mathbf{0.24267}; n_2 = \mathbf{6.17891 \cdot 10^{-3}}; n_3 = \mathbf{7.88098 \cdot 10^{-4}} \quad (35)$$

Using these values (35), Eq. (16) gives us a simple approximation for the cantilever eigenmodes:

$$\boxed{f_n^{vac} = \frac{1}{2\pi} \sqrt{\frac{k}{n_n m_b}}}. \quad (36)$$

Eq. (36) along with calculated parameters n_n (35) will be used as a starting point for mass-sensitivity estimations carried out in the next section.

It is necessary to note that derived values of n_n (35) take into account both the effective spring constant and the effective mass changes. Actually, higher modes affect the suspended mass of the harmonic oscillator (Eq. (16)) negligibly in comparison with the influence of the cantilever clamping, which is defined by the geometric parameter n_n . The resonance frequency at higher modes increases due to a drastic increase of the effective spring constant. It follows from a multi-mode resonance model, as it is shown in [88]. However, it is attractive to use simple harmonic oscillator model (Eq. (16) or (36)) with static spring constant (Eq. (13)) and variable effective mass (Eq. (31)), which in its own turn takes into account both higher mode effects (through the geometric parameters n_n derived in (35)) and the added adsorbed mass. Hence, this work considers the cantilever effective mass as a phenomenological concept by analogy with the electron effective mass in semiconductor physics. It allows maintaining consistence with simple harmonic oscillator model for fast and explicit estimations on the cantilever resonances.

2.3. Mass detection theory

Now we have a basic theory on how the spring constant and the resonance frequency depend on the cantilever dimensions. Hence, we can derive an expression for the mass, which could be detectable by the cantilever. Assuming an effective suspended mass m_{eff} , which consists of both a concentrated and a distributed mass, let's consider the influence of an added (adsorbed or deposited) mass Δm on the resonance frequency of the cantilever. There are 3 cases, which should be considered to analyse gravimetric responses of resonating microcantilever transducers.

- 1) **$\Delta m = 0$.** The effective suspended mass m_{eff} is defined by the beam mass unambiguously according to Eq. (36). Thus, the modal frequencies are given by:

$$f_n^0 = \frac{1}{2\pi} \sqrt{\frac{k}{n_n \rho w h l}}. \quad (37)$$

- 2) **$\Delta m > 0$ and is concentrated (further referred to as Δm_{conc}).**

If the added mass is much smaller than the mass of the cantilever beam and it is concentrated at the beam apex (e.g. functionalization pad is deposited near the cantilever apex), the total eigenmode-dependent effective mass of the oscillator is supposed to be:

$$(m_{eff})_n = n_n \rho w h l + \Delta m_{conc}. \quad (38)$$

Then the corresponding eigenfrequency will be defined by:

$$f_n^{\Delta m_{conc}} = \frac{1}{2\pi} \sqrt{\frac{k}{n_n \rho w h l + \Delta m_{conc}}}. \quad (39)$$

Estimations according to Eq. (39) are graphically represented in Fig. 9.

By measuring the resonance frequencies before and after the mass change, the concentrated mass is then:

$$\Delta m_{conc} = \frac{k}{4\pi^2} \left[\frac{1}{(f_n^{\Delta m_{conc}})^2} - \frac{1}{(f_n^0)^2} \right]. \quad (40)$$

Eq. (40) suggests that the minimum detectable mass of the cantilever is directly proportional to the spring constant and inversely proportional to the difference of the resonance frequency squared, before and after the mass change.

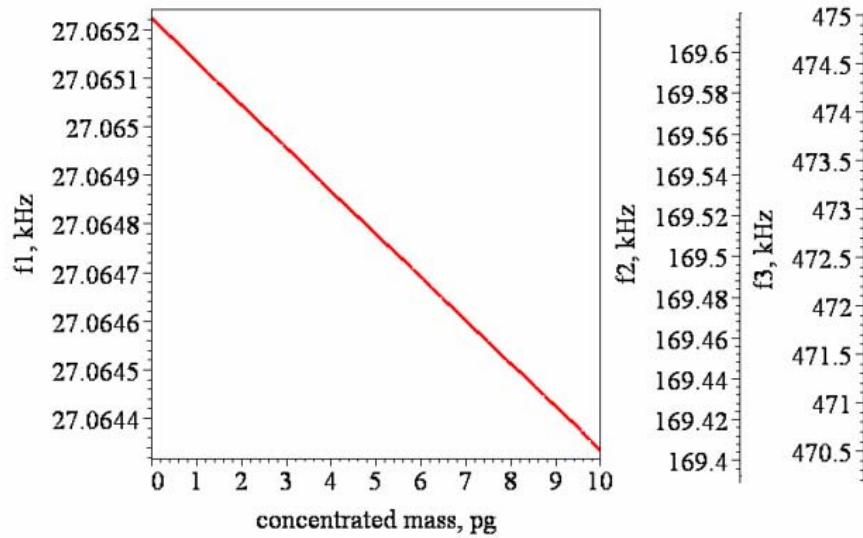


Fig. 9. Dependencies of the cantilever eigenfrequencies versus increment of adsorbed concentrated mass for first three eigenmodes.

As it can be assumed from Eq. (40), 1 Hz frequency shift for the given dimensions corresponds to the following added concentrated masses for the lowest 3 modes:

- 1st mode – 11.28 pg;**
- 2nd mode – 45.84 fg;**
- 3rd mode – 2.09 fg.**

Estimated mass changes versus corresponding frequency shifts ranged from 0 to 100 Hz are shown in Fig. 10.

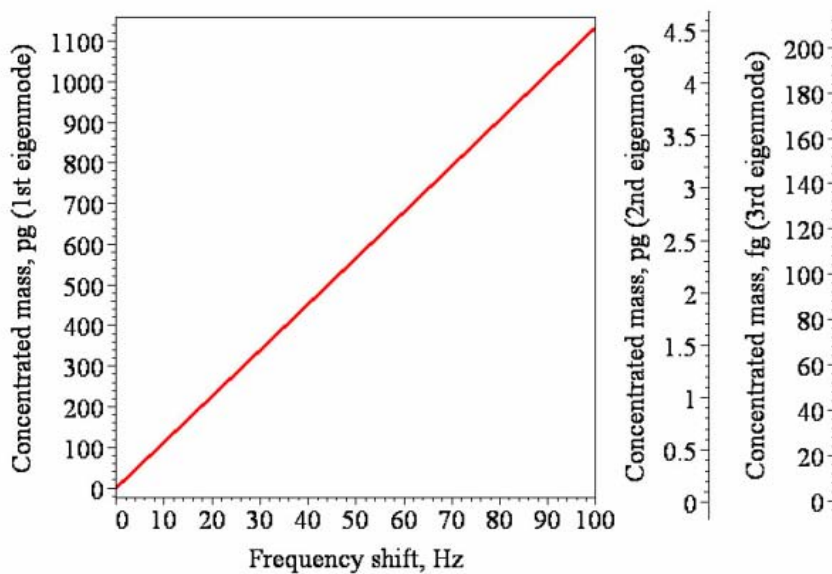


Fig. 10. Mass sensitivities versus frequency shift for the 1st mode [pg], the 2nd mode [pg], and the 3rd mode [fg].

In case that adsorbed mass is located beyond the cantilever apex, then the corresponding eigenfrequency calculation according to Eq. (39) becomes less straightforward, and FEM-simulations are needed. ANSYS-simulations exploring the frequency shift vs. position of the located mass are shown in Fig. 11.

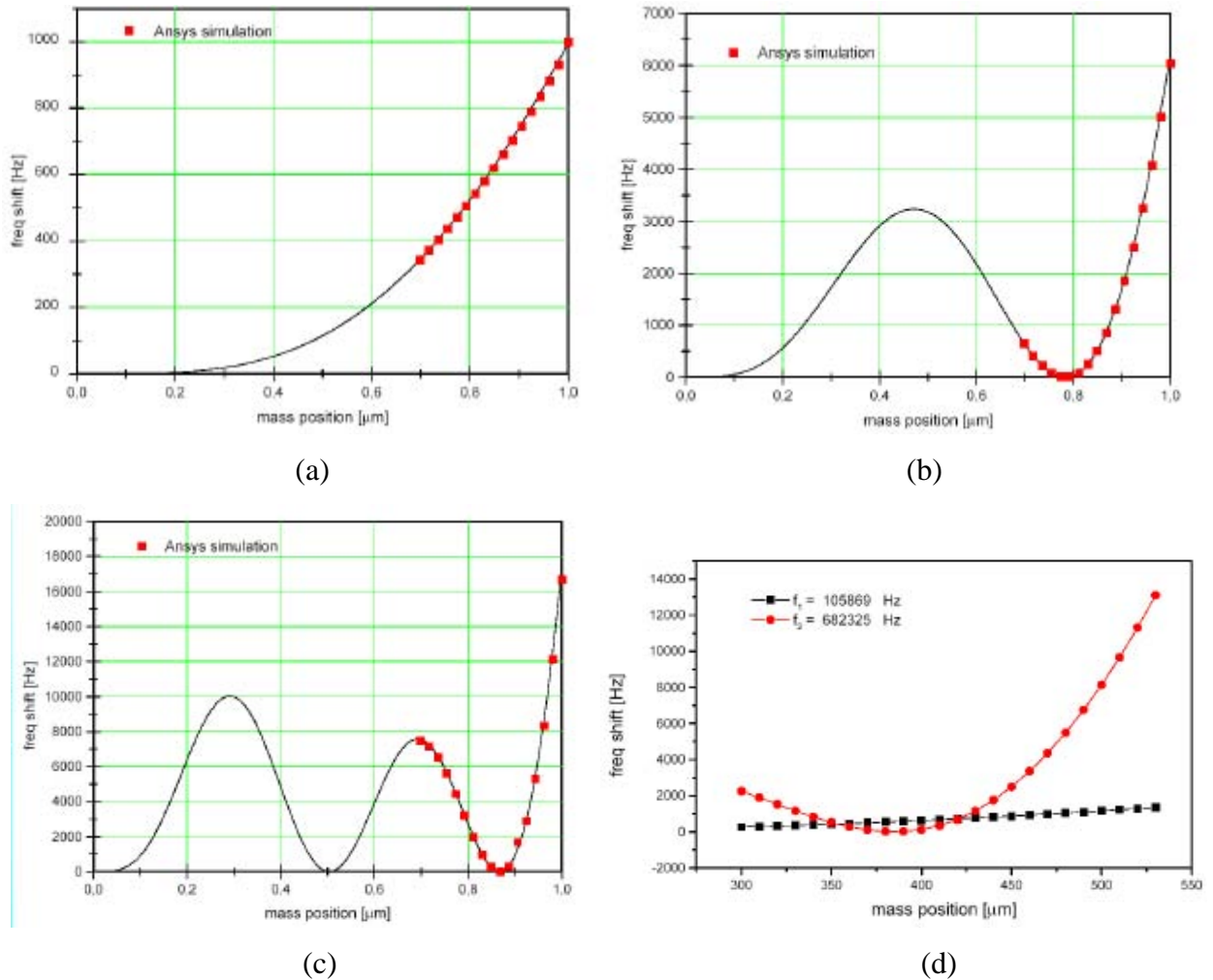


Fig. 11. ANSYS-simulations of cantilever's eigenfrequencies versus position of the located mass:

- (a) ideal cantilever, 1st eigenmode;
- (b) ideal cantilever, 2nd eigenmode;
- (c) ideal cantilever, 3rd eigenmode;
- (d) real cantilever, 1st and 2nd eigenmodes.

As follows from Fig. 11, located mass displacement from the cantilever apex results in the smooth sensitivity degradation for the 1st eigenmode (Fig. 11, a and d). However, the situation appears more complicated for higher eigenmodes (Fig. 11, b, c, and d): the sensitivity degrades smoothly only at the end part of the cantilever, then there are some periodic gaps, in which the cantilever is practically insensitive. Thus, if the adsorbed mass is located along the cantilever beam, one should take into consideration mass losses in general and these “blind gaps” in particular, especially by working at higher eigenmodes.

- 3) $\Delta m > 0$ and is distributed uniformly on the cantilever beam (further referred to as Δm_{distr}).

In the case of uniformly distributed mass, the effective modal mass can be approximated as:

$$(m_{\text{eff}})_n = n_n(\rho h w l + \Delta m_{\text{distr}}). \quad (41)$$

In the case of concentrated added mass, it is reasonable to assume that the spring constant k remains unaffected. However, there are some evidences that chemical interactions between a functionalized cantilever transducer and its environment appreciable affect the cantilever spring constant in case of distributed added mass thus making analysis of gravimetric responses less straightforward [59, 89, 90]. For instance, changes in the cantilever spring constant by over one order of magnitude from 0.5×10^{-3} to 7.5×10^{-3} N/m were observed in response to NaCl concentration increased from 0.05 to 0.8 M/L in aqueous solution [90]. Significant adsorption-induced variations of the spring constant can be observed with gelatine-coated cantilevers under exposure to water vapour as well as gold-coated cantilevers under exposure to mercury vapour. In the latter case, adsorbate-induced differential surface stress $\Delta\sigma$ (ref. to Fig. 6) was estimated to be 0.38 N/m [79]. A simplified taut string model may relate adsorbate-induced differential surface stress and the variations of the spring constant [79]:

$$\delta k = \frac{\pi^2 n}{4n_s} \Delta\sigma, \quad (42)$$

where $\Delta\sigma$ is the differential surface stress change of the microcantilever before and after the adsorption of analytes, n is the geometric parameter for the rectangular cantilever, and n_s is a geometrical factor, which accounts to the using of the taut string model.

Eigenfrequencies of the cantilever loaded with a distributed mass in the absence of damping can be approximated as:

$$f_n^{\Delta m_{\text{distr}}} = \frac{1}{2\pi} \sqrt{\frac{k + \delta k}{n_n \rho w h l + n_n \Delta m_{\text{distr}}}}. \quad (43)$$

The simulations according to Eq. (43) are depicted in Fig. 12. 100 pg of adsorbed distributed mass result in the resonance frequency shift of approximately 2 Hz for the 1st eigenmode, 15 Hz for the 2nd eigenmode, and 40 Hz for the 3rd eigenmode.

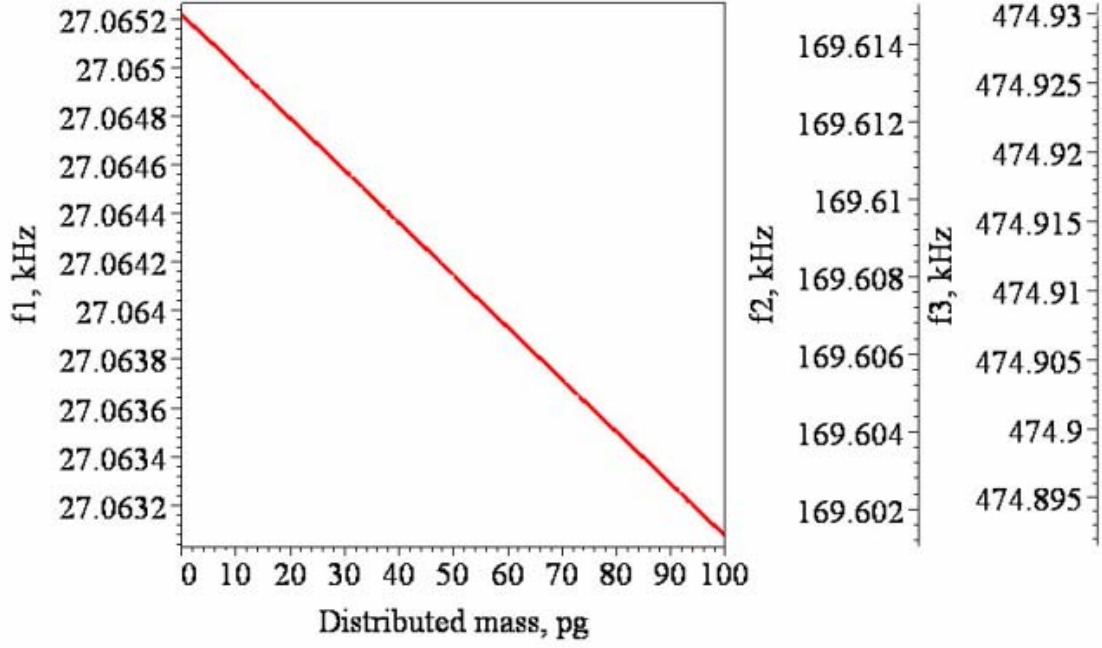


Fig. 12. First three eigenmodes for the uniformly loaded cantilever versus the distributed mass increment.

A total amount of the distributed mass, which influence on the elasticity of the cantilever, can be calculated according to:

$$\Delta m_{distr} = \frac{k}{4\pi^2 n_n} \left[\frac{1 + \frac{\delta k}{k}}{\left(f_n^{\Delta m_{distr}}\right)^2} - \frac{1}{\left(f_n^0\right)^2} \right] \quad (44)$$

It means that 1 Hz frequency shift for the given dimensions corresponds to the following added distributed masses for the lowest 3 modes:

- 1st mode – 46.49 pg;**
- 2nd mode – 7.42 pg;**
- 3rd mode – 2.65 pg.**

Assuming that the uniformly distributed mass has negligible impact on the cantilever stiffness so that the spring constant k remains unchanged, thus the resonance frequency shift up to 100 Hz (in first 3 eigenmodes) can be interpreted as distributed mass load according to Fig. 13.

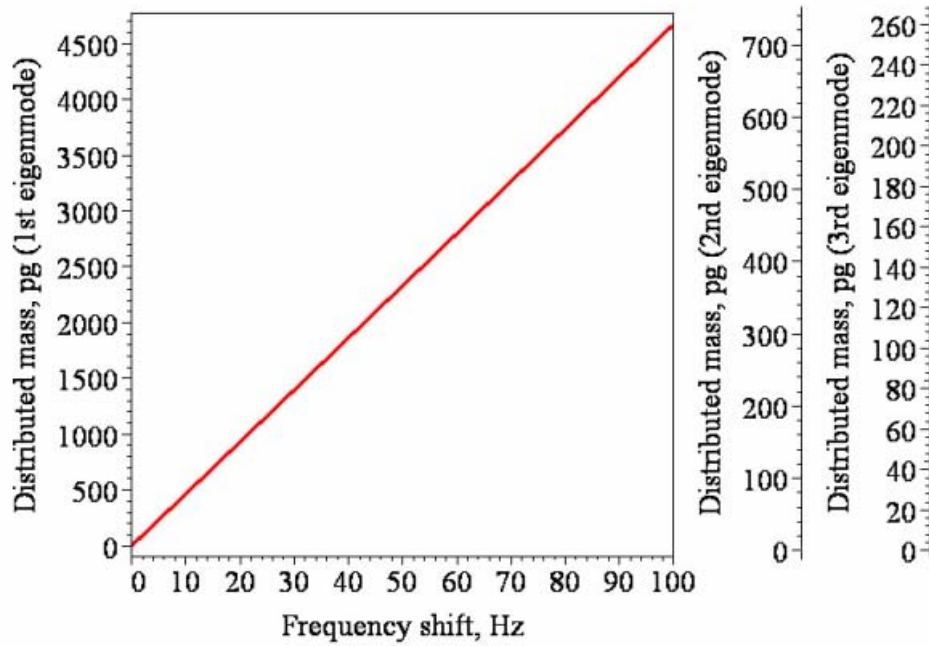


Fig. 13. Estimation of the uniformly adsorbed mass (in picogram) versus resonance frequency shift in first three eigenmodes.

Combined influence of both resonator parameter variations, i.e. cantilever stiffness and the load mass, has been simulated with Maple ®. The results are represented as 3D-graphs in Fig. 14, which show resonance frequency of the cantilever as function of small spring constant variations, δk (up to 0.1 % from its initial value of 4.41 N/m), and picogram-ranged load mass δm .

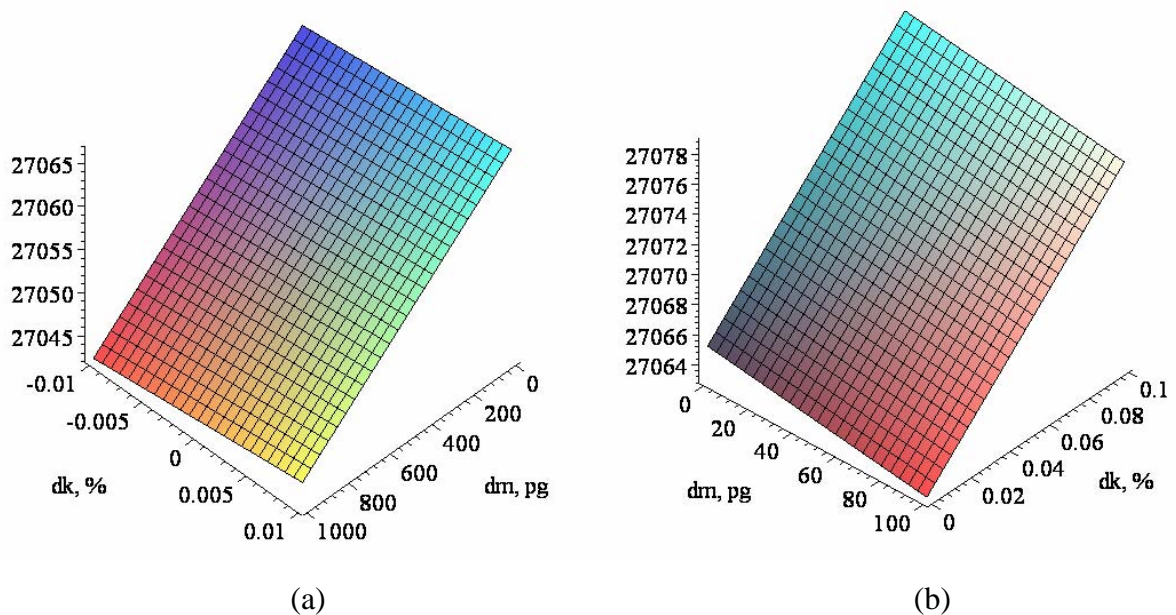


Fig. 14. Natural resonance changes due to primarily mass load (a), and the spring constant variations (b).

Fig. 14 illustrates that even small variations of the spring constant may significantly influence the resonance frequency shift (a) or even contradict the mass load effect (b). However, appropriate models of such influence and its quantitative measures are still lacking. A practically feasible technique to overcome such a hardly predictable influence would be the introduction of another similarly functionalized transducer type for referent purposes.

2.4. Experiments on higher order modes operation

Higher eigenmodes can potentially satisfy better mass resolution. In our experiment, a change of the relative humidity from 5 to 80% has resulted in a total resonance frequency shift of a cantilever functionalized with photoresist AZ1518:

$$19\ 850\ \text{Hz} - 19\ 730\ \text{Hz} = 120\ \text{Hz for the 1}^{\text{st}}\ \text{mode}$$

and

$$124\ 060\ \text{Hz} - 123\ 730\ \text{Hz} = 330\ \text{Hz for the 2}^{\text{nd}}\ \text{mode.}$$

Comparison of the mass sensitivity in different eigenmodes are also presented by Dohn [91] and are shown along with ANSYS simulations by Ivanov [7] of the one-dimensional cantilever beam in Fig. 15. The last column in Fig. 15 shows the estimated mass gain when operating in higher order modes.

ANSYS simulations [7]	f_{exp} (Hz)	f_{sim} (Hz)	Δf_{max} (Hz)	$\delta m_1 / \delta m_n$
	30712	31734	480	1
	192493	198815	2541	23
	539060	556486	6059	102
	1056640	1089920	9864	276

Fig. 15. ANSYS-simulations of four cantilever eigenmodes as an example of the mass sensitivity gain in higher order modes.

Two PMMA-coated cantilevers were checked by operating in first three eigenmodes under the influence of acetone vapours with different concentrations in constant total gas flow of 317 sccm. The experimental conditions and the set-up will be described in Chapter 3. in more details. Firstly, the cantilever's amplitude responses were found by scanning a wide frequency range at the exposure to dry nitrogen flow in order to embrace first three eigenmodes, as it is shown in Fig. 16. Third eigenmode is represented by its satellite peak only, because its base peak is above 1 MHz cut-off frequency of the electronics. The highlighted peaks have been found with 1 Hz resolution and their shift has been monitored under exposure to acetone vapours.

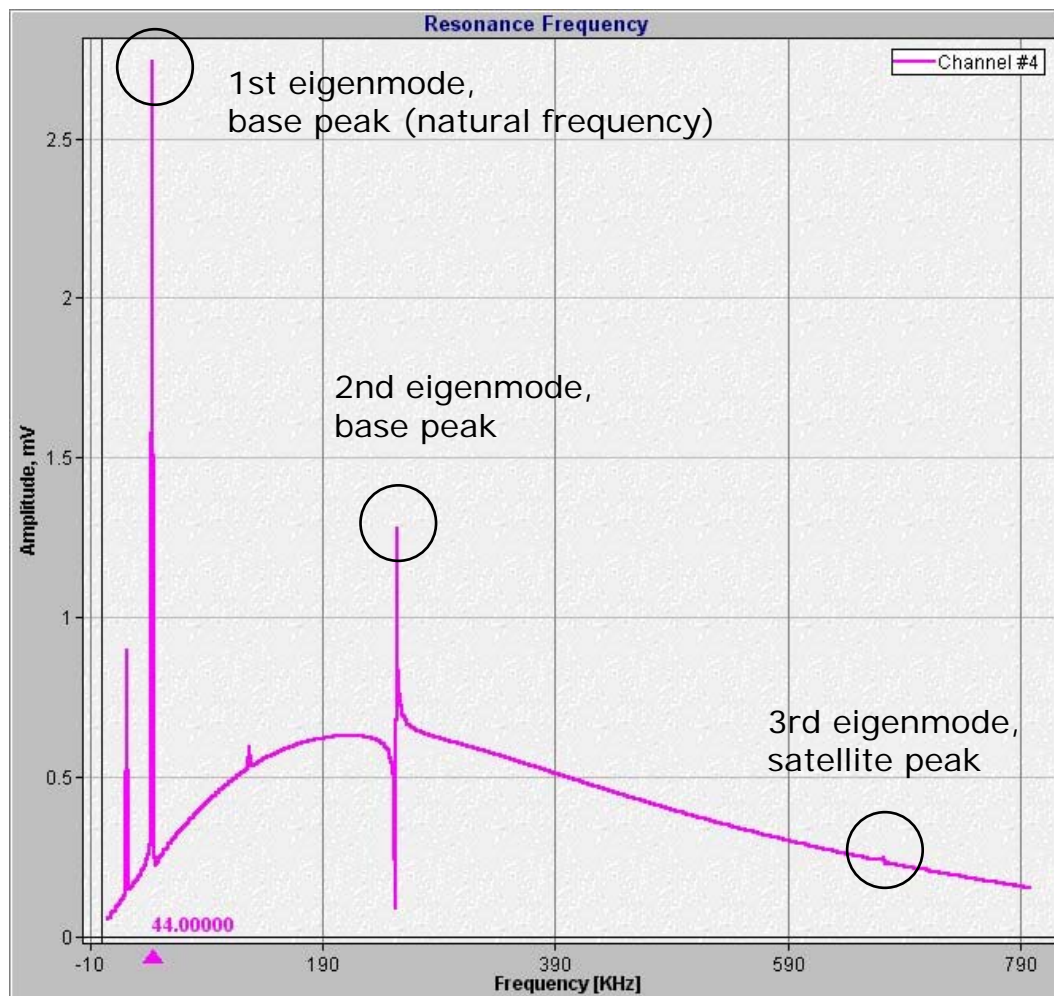


Fig. 16. First three eigenmodes of a PMMA-coated cantilever.

Third eigenmode is represented by its satellite peak only.

Fig. 17 shows transfer curves for the first three eigenmodes in comparison. The 3rd eigenmode is represented by its hardly resolved satellite peak, thus responses at this mode are not very reliable and linear. First and second modes on the contrary exhibit stable and linear responses.

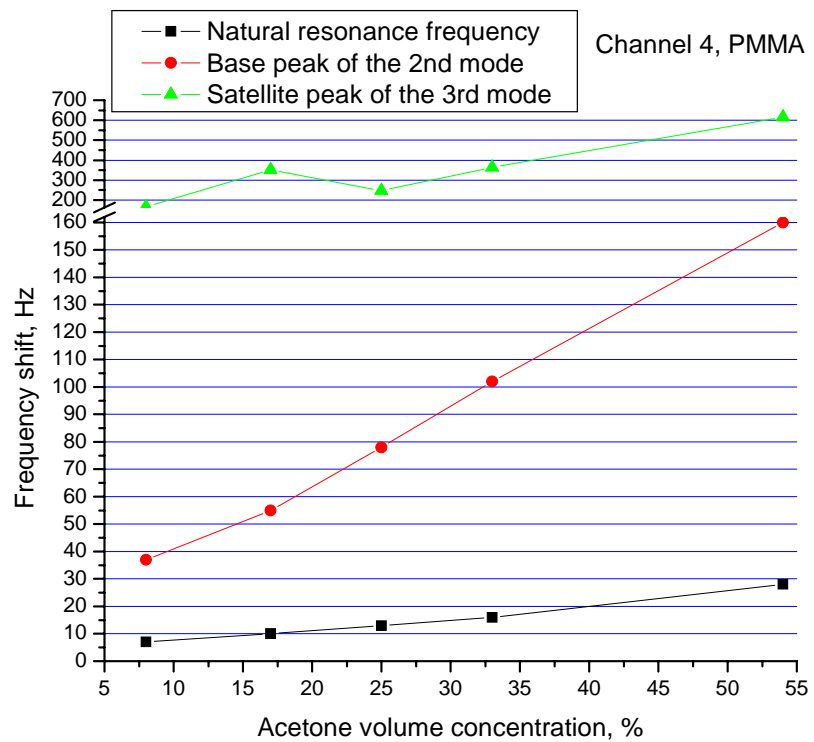
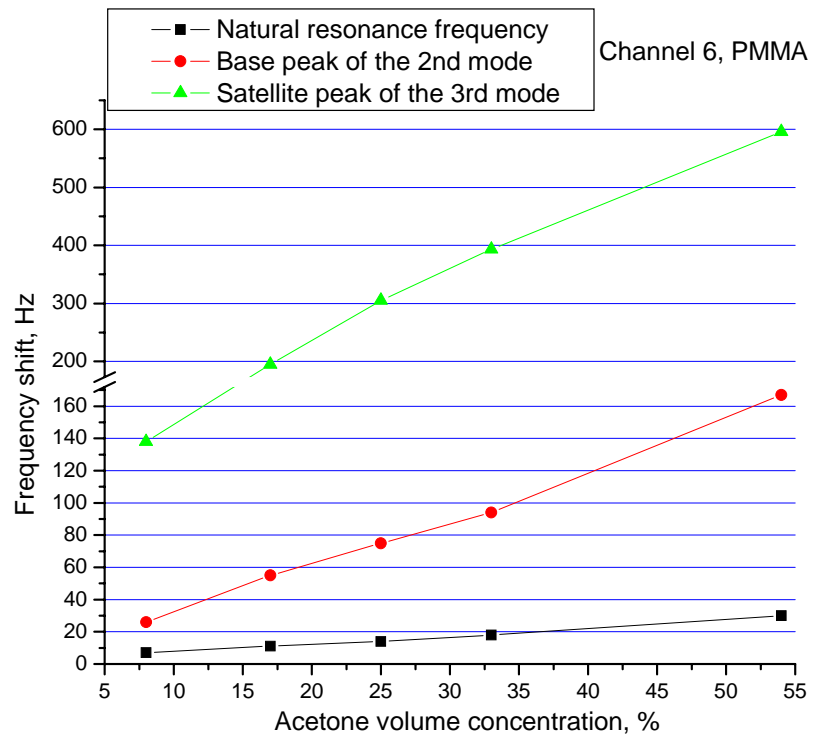


Fig. 17. Transfer curves for 2 different PMMA-coated cantilevers in first three eigenmodes under exposure to acetone vapours with different concentrations.

It is clearly seen from Fig. 17 that higher mode operation leads to higher sensitivity, because of steeper slope of the transfer curve. Two different PMMA-coated cantilevers show similar resonance frequency shifts for the analyte exposition, as it is seen in Tab. 3.

Eigenmode <i>n</i>	Cantilever at Channel 4			Cantilever at Channel 6		
	f_n^d , Hz	f_n^0 , Hz	Δf , Hz	f_n^d , Hz	f_n^0 , Hz	Δf , Hz
1	43 968	43 940	28	44 939	44 909	30
2	253 722	253 560	162	257 640	257 473	167
3	671 991	671 375	616	681 471	682 070	599

Tab. 3. First three eigenfrequencies changes of 2 different PMMA-coated cantilevers towards injection of 54 vol. % of acetone.

In conclusion to the mass sensitivity estimation it is worth to note a simple expression approximated for practical usage, where mass change is given through the frequency shift:

$$\Delta m = \frac{k_n}{4\pi^2} \left(\frac{1}{f_1^2} - \frac{1}{f_0^2} \right) \approx \frac{k_n}{4\pi^2} \frac{2\Delta f}{f_0^3}, \quad (45)$$

where k_n is the cantilever spring constant for each eigenmode, so that $k_{n+1} \gg k_n$.

Eq. (45) is given in assumption that variations in the spring constant k are negligible. This is true for most analyte-adsorbent interactions, except those with very high affinity of the adsorbate to the cantilever surface, e.g. mercury vapour to gold-coated cantilever, or water vapour to gelatine-coated cantilever. These examples suggest that if *wetting* phenomenon appears sufficient in adsorbate interactions with the cantilever surface, then at higher analyte concentrations, non-negligible variations in the spring constant can be anticipated. Obviously, lower analyte concentrations, which are near the mass resolution threshold, cannot influence the stiffness in any considerable manner.

2.5. Mass resolution limitations

The factors, which influence on the cantilever transducer sensitivity, are listed in Fig. 18. They are due to either variations of the effective mass or resonance frequency instability. In its own turn, the former is defined by the material and geometry of the resonator, and the latter is governed by fluctuations of quantum nature. Obviously, better mass sensitivity can be attained with lower effective mass of the resonator. However, nanoresonators are more susceptible to the fundamental noises as the device geometry is shrunked down to the sizes of detectable particles.

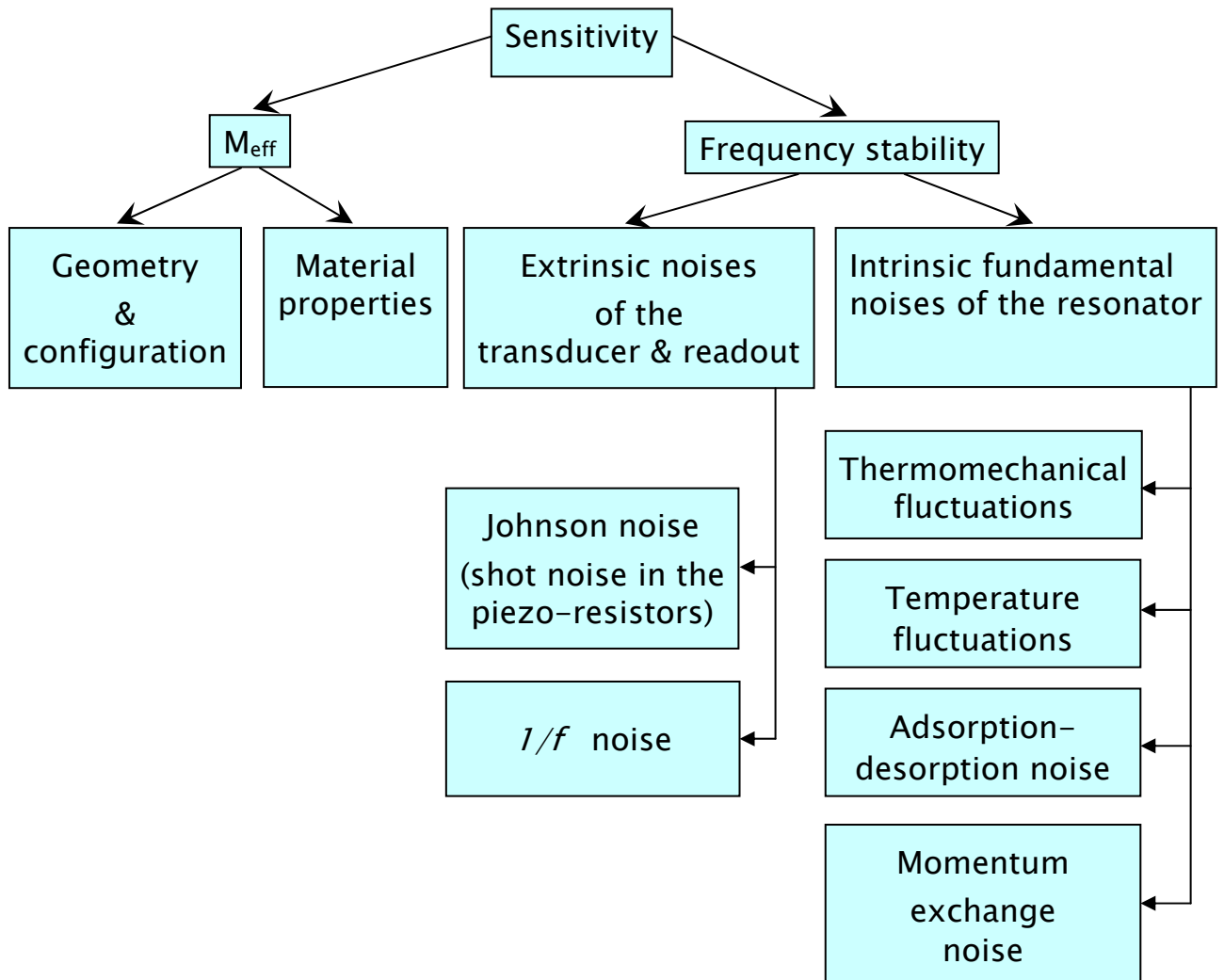


Fig. 18. Factors, which influence the mass sensitivity.

Generally speaking, intrinsic fundamental noises overviewed in § 2.5.1 are sufficient only for nanosized cantilevers and Dalton-range sensitivity limits. Sensing of single atoms would be hardly resolvable without device optimisation to diminish intrinsic noise influence. Real TASNANO piezo-resistive cantilevers are much more susceptible to the read-out unit noises, such as Johnson noise and $1/f$ noise. $1/f$ noise can be neglected by operating the cantilever in dynamic mode at frequencies higher than 10 kHz. In its own turn, Johnson noise has the highest impact, thus will be considered in more detail in § 2.5.2.

2.5.1. Intrinsic cantilever noises

Limitations for mass sensitivity due to the intrinsic physical noise mechanisms embrace thermomechanical fluctuations, temperature fluctuations, adsorption-desorption noise, and momentum exchange noise [92].

Thermomechanical fluctuations are a consequence of the fluctuation–dissipation theorem. They originate from thermally driven random motion of the mechanical device. Mass

sensitivity in the Dalton range (single atom sensitivity) is easily achievable, even for moderately large bandwidths. As device sizes are scaled downward while maintaining high resonance frequencies, M_{eff} and k_{eff} shrink in direct proportion. Devices with small stiffness (high compliance) are indeed more susceptible to thermal fluctuations, and consequently the measurement dynamic range is correspondingly reduced. Thermomechanical fluctuations in terms of mass are given by [92]:

$$\delta M = 2M_{eff} \sqrt{\frac{k_B T}{E_c} \frac{\Delta f}{Q \omega_0}}, \quad (46)$$

where ω_0 – fundamental resonance frequency; δM – the mass sensitivity; $E_c = M_{eff} \omega_0^2 \langle x_c^2 \rangle$ – maximum drive energy; $\langle x_c \rangle$ – maximum rms drive level still producing a predominantly linear response; $k_B T$ – thermal energy; Q – Q-factor; Δf – effective bandwidth; M_{eff} – effective mass of the resonator.

Temperature fluctuations are caused by small heat capacity of a nanomechanical resonator. Its susceptibility to such fluctuations depends upon the strength of its thermal contact to the environment. Since the resonator's dimensions and material parameters are both temperature dependent, temperature fluctuations will generate frequency fluctuations. Despite the role of thermal fluctuations in generating phase noise limitations to the mass sensitivity, single-Dalton sensing is readily achievable. Obviously, the smaller incarnations of NEMS are the most susceptible to temperature fluctuations. This progressively becomes more significant at elevated temperatures. This can be circumvented by lowering the device temperatures and by optimizing thermal contact (improved heat sink) between a NEMS with its environment. Temperature fluctuations are given by [92]:

$$\delta M = \frac{4M_{eff}}{\sqrt{\pi}} \left(-\frac{22,4c_s^2}{\omega_0^2 l^2} \alpha_T + \frac{2}{c_s} \frac{\partial c_s}{\partial T} \right) \sqrt{\frac{k_B T^2 \arctan(2\pi \Delta f \tau_T)}{g \tau_T}}, \quad (47)$$

where ω_0 – fundamental resonance frequency; δM – the mass sensitivity; $k_B T$ – thermal energy; Δf – effective bandwidth; l – cantilever length; C_s – the temperature dependent speed of sound; α_T – linear thermal expansion coefficient; g – thermal conductance; τ_T – thermal time constant; M_{eff} – effective mass of the resonator.

Adsorption-desorption noise is fluctuations in the resonance frequency induced by random, thermally driven adsorption and desorption of molecules. Gas molecules in the vicinity of a resonator – each with mass m – can adsorb upon the resonator's surface, mass load the device, and thereby change its resonance frequency. The adsorption-desorption cycle can most conveniently be modelled by a flux-dependent adsorption rate and a thermally activated

desorption rate. Adsorption–desorption processes will not preclude attainment of single-Dalton mass sensitivity. Adsorption–desorption noise becomes most significant in the temperature regime where the adsorption and desorption rates are comparable; hence, for a given device configuration, it can be minimized by judicious choice of operating temperature. Surface passivation to reduce the binding energy between the molecule and the surface should also be effective in this regard. Given that the adsorption–desorption noise is a surface effect, it becomes increasingly important as device sizes shrink. Adsorption-desorption noise in terms of mass is given by [92]:

$$\delta M = \frac{1}{2\pi} m \sigma_{occ} \sqrt{N_a \arctan(2\pi \Delta f \tau_r)}, \quad (48)$$

where ω_0 – fundamental resonance frequency; δM – the mass sensitivity; N_a – number of sites for adsorption; m – molecule mass; σ_{occ}^2 – variance in the occupation probability of a site; τ_r – correlation time for an adsorption-desorption cycle; Δf – effective bandwidth; M_{eff} – effective mass of the resonator.

Momentum exchange noise can be treated as consequences of momentum exchange, in a gaseous environment, between the nanomechanical resonator and the gas molecules that impinge upon it. Momentum noise appears to be an insignificant source of noise for NEMS operating in vacuum with residual pressure less than 0.1 Pa. Momentum exchange noise in terms of mass is given by [92]:

$$\delta M = 2M_{eff} \sqrt{\frac{k_B T}{E_c} \frac{\Delta f}{Q_{gas} \omega_0}}, \quad (49)$$

where ω_0 – fundamental resonance frequency; δM – the mass sensitivity; Q_{gas} – quality factor due to the gas dissipation; $E_c = M_{eff} \omega_0^2 \langle x_c^2 \rangle$ – maximum drive energy; $\langle x_c \rangle$ – maximum rms drive level still producing a predominantly linear response; $k_B T$ – thermal energy; Q – Q-factor; Δf – effective bandwidth; M_{eff} – effective mass of the resonator.

2.5.2. Extrinsic Johnson noise

Extrinsic Johnson noise introduces the most valuable contribution into the total noise. It is naturally a shot noise in the piezo-resistors comprising the read-out unit. The RMS-voltage of Johnson noise by definition is given by:

$$U_{noise} = \sqrt{4 \cdot k_B T \cdot R_{bridge} \cdot \Delta f}, \quad (50)$$

where, $k_B T$ – thermal energy, R_{bridge} is resistance of the piezo-resistive read-out, Δf – bandwidth.

Since $U_{signal} = U_{bridge} \pi \cdot \sigma$, then the *surface stress* and *differential surface stress* can be expressed correspondingly:

$$\sigma = \frac{1}{\pi} \frac{U_{signal}}{U_{bridge}}, \text{ and} \quad (51)$$

$$\Delta\sigma = \frac{t}{\pi} \frac{U_{signal}}{U_{bridge}}, \quad (52)$$

where U_{bridge} – voltage supplied to the Wheatstone bridge, U_{signal} – output bridge voltage for the stressed cantilever, $\pi = \frac{\pi_T - \pi_L}{2}$ is average coefficient of piezo-resistivity, t – thickness of the implanted shallow piezo-resistors.

The cantilever bending is interrelated with the output bridge voltage through Stoney's equation: $z_{signal} = \frac{3 \cdot l^2}{4 \cdot Y \cdot h^2} \Delta\sigma = \frac{3 \cdot l^2 \cdot t}{4 \cdot Y \cdot h^2 \cdot \pi} \frac{U_{signal}}{U_{bridge}}$, so that:

$$z_{signal} = \frac{3l^2 t (1 - \nu^2)}{2(\pi_T - \pi_L) E h^2} \frac{U_{signal}}{U_{bridge}}, \quad (53)$$

where z – cantilever deflection, l – cantilever length, h – cantilever thickness, $Y = \frac{E}{1 - \nu^2}$ – effective modulus of elasticity, E – Young's modulus, and ν – Poisson's ratio.

Finally, Johnson noise can be expressed in terms of z-deflection as:

$$z_{noise} = \frac{3l^2 t (1 - \nu^2)}{(\pi_T - \pi_L) E h^2} \frac{\sqrt{k_B T \cdot R_{bridge} \cdot \Delta f}}{U_{bridge}}. \quad (54)$$

The deflection caused by noise should be obviously smaller than the effective deflection component, i.e. $z_{noise} \leq z_{signal}$. TASNANO-cantilevers have the resistance change better than $\Delta R/R = 6 \cdot 10^{-5}$ per nm deflection, which in terms of output voltage corresponds to 1 μ V if $U_{bridge} = 1$ V.

2.6. Noise subtraction using a referent channel with uncoated cantilever.

A feasible technique to improve signal pattern of a chemical sensor is differential subtraction of its signal from the signal of a referent transducer, which is not functionalized, but is placed at same environmental conditions. Such the way, the signal from the referent transducer, which is in our case an uncoated cantilever, is also modulated by environmental

noises, e.g., temperature or gas flow fluctuations. Fig. 19 shows stacked signals from uncoated cantilever, cantilever coated with PMMA and their differential signal. The signals were gathered at the same time interval. Injection of 500 ppm of ethanol vapours was performed after 77 min of steady-state operation in closed Teflon measurement cell (Fig. 50) at ambient conditions. Ambient temperature was equal to 26.4 °C. The duration of ethanol vapour exposure was 17 min.

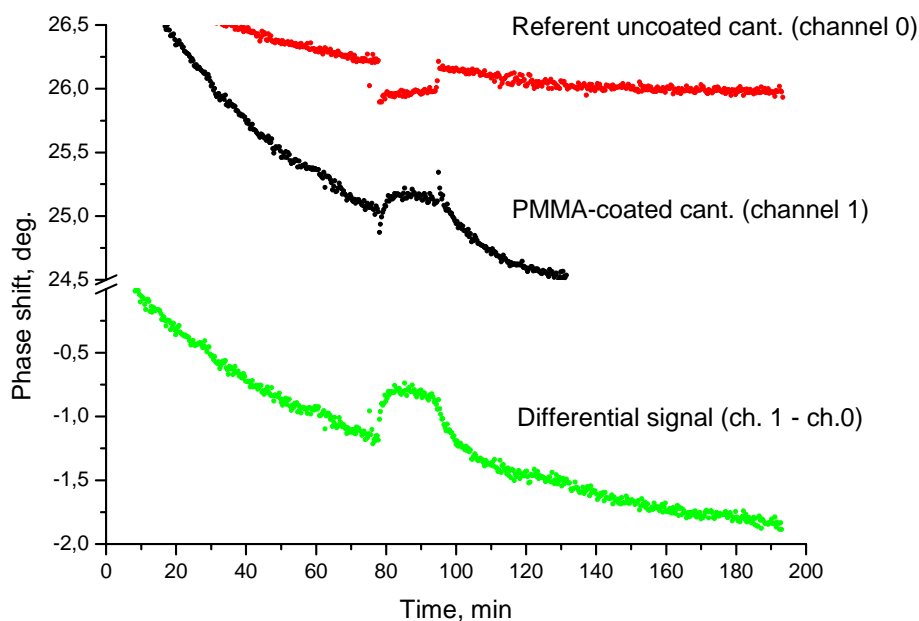


Fig. 19. Practical improvement of the signal pattern by differentiating the signals of the PMMA-coated cantilever (black dots) and the referent (uncoated) cantilever (red dots). The resulting signal is shown below (green dots).

The differential signal has higher amplitude of the response, i.e. 0.4 deg. instead of 0.3 deg. of the initial phase shift gathered from the PMMA-coated cantilever. These values correspond to 0.96 Hz and 0.72 Hz of the resonance frequency shift respectively. Moreover, the signal subtraction technique removed the spikes related to the gas injection and purging with the syringe. Finally, the processed signal looks more distinctly, and is therefore more appropriate for analysis.

2.7. Temperature dependencies

A change in temperature will affect the spring constant and the resonance frequency due to the thermal expansion of the material and due to the temperature dependence of the elastic constants, such as Young's modulus. The definition of Young's modulus (E) is the ratio of stress (σ) to elastic strain (ε_{el}):

$$E = \frac{\sigma}{\varepsilon_{el}} = \frac{F/S}{\Delta l/l_0}, \quad (55)$$

where F/S is the force per area and $\Delta l/l_0$ is the relative elongation due to the materials response to the stress. It is clear that when the material contracts, due to a temperature drop, F/S increases since the area decreases. This leads to an increase of Young's modulus when the temperature drops.

The temperature dependence of Young's modulus in silicon is governed by the following equation [87]:

$$E(T) = 0.1681873 \cdot T^4 - 449.0539 \cdot T^3 + 464875.9 \cdot T^2 - 2.319830 \cdot 10^8 \cdot T + 2.061456 \cdot 10^{11} \quad (56)$$

During linear thermal expansion or contraction, of any rectangular body, all the geometrical dimensions change with a factor:

$$a = (1 + \alpha \cdot \Delta T) \quad (57)$$

due to a temperature change, ΔT . Here, α is the thermal expansion coefficient of the material. Note that ΔT is positive for increases in temperature and negative for decreases in temperature.

For most materials the expansion coefficient is very small, approximately 10^{-6} K^{-1} (for silicon $\alpha_{\text{Si}} = 2.3 \cdot 10^{-6} \text{ K}^{-1}$), and the relative change in E is approximately 10^{-4} K^{-1} . Thus, the dependence of the resonance frequency on temperature is mainly through Young's modulus. Therefore, we would expect an increase in the resonance frequency, f , and in the spring constant, k , as the temperature decreases. Maple-simulation confirms this theoretical prediction. An increase in resonance frequency is clearly seen in Fig. 20 as the temperature decreases.

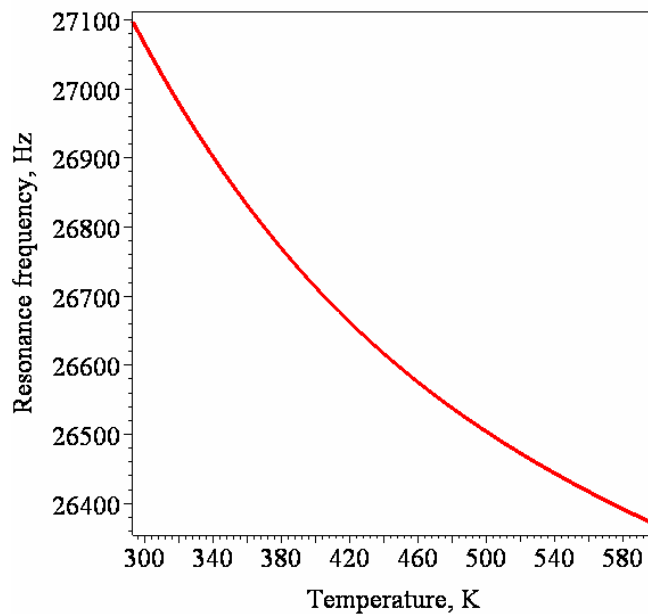


Fig. 20. Simulated resonance frequency of silicon cantilever vs. temperature.

Drift of the resonance frequency and the phase shift was always observed by actuating the cantilever with integrated heater, e.g., as it is shown in Fig. 21. A cantilever with integrated thermal heater ($R = 14.7 \text{ Ohm}$) coated with vinylchloride-vinylacetate copolymer was actuated by supplying alternative voltage 0.7 V and constant bias 0.2 V . The actuation during 5 sec. was continuously being repeated in every 43 sec. Such a way, accumulated heat is dissipated slower than the cool-down time, which is required for tiny cantilever.

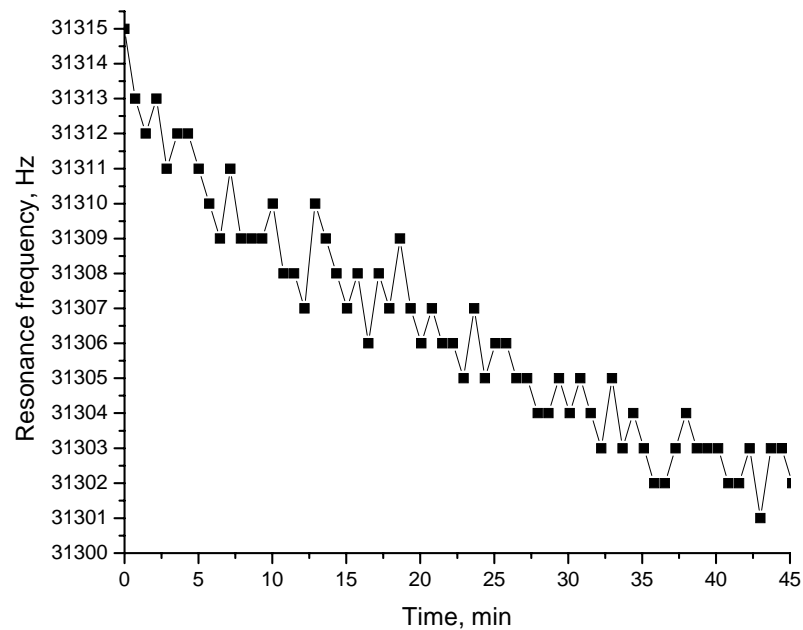


Fig. 21. Experimentally measured resonance frequency drift due to the heating.

The total resonance frequency shift 15 Hz is observed after 45 min of operation time. This account for approximately 5°C increase of the cantilever temperature, which is rather realistic. The piezo-resistive read-out is also very temperature-dependent, however its Wheatstone-bridge design suppresses this influence, because all 4 resistors are subjected to the same temperature. Further experiments and discussion on the topic is given in §§ 2.9.1.1 “Integrated piezo-resistive read-out” and 2.9.2.1 “Integrated bimorph actuator”. Obviously, the baseline drift should be taken into account by renewing its value just before each exposition to the analyte.

2.8. Pressure dependencies

When the resonator is in an atmosphere of gas particles, the particles damp the motion of the resonator. The pressure exerts a reactive force on the resonator, which can be thought of as gas particles moving with the resonator enlarge the effective mass of the resonator. The resonance frequency is inversely proportional to the square root of the resonator’s effective

mass, $f_{res} \propto \sqrt{1/m_{eff}}$. This indicates that as the pressure drops the effective mass approaches the actual resonator mass. Thus, the resonance frequency will rise to a certain level and then will flatten out.

The damping force due to airflow, squeeze force, internal friction, and support loss can be, respectively, calculated by using a bead-model approximation of the Navier-Stokes equation, a narrow-bearing approximation of the Reynolds equation, structural damping theory, and a two-dimensional theory of elasticity [93]. In case of negligible viscous effects, the eigenmode frequencies in damping media f_n^{media} can be unambiguously corresponded to the eigenfrequencies in vacuum f_n^{vac} by following relation [94]:

$$\frac{f_n^{media}}{f_n^{vac}} = \left(1 + \frac{\pi \rho_{media} w}{4 \rho_{cant} h} \right)^{-\frac{1}{2}}, \quad (58)$$

where ρ_{cant} and ρ_{media} are densities of the cantilever beam material and the damping media, respectively; w is the cantilever beam width, and h is its thickness. This simple approximation was derived under assumption of a uniform isotropic rigid rectangular cantilever, which length greatly exceeds its width, and the beam deflections are far smaller than any length scale in the beam geometry.

A more detailed discussion of various damping mechanisms in microcantilever transducers related to external as well as intrinsic dissipation phenomena is given in § 2.8.1; experimental results on damping effects and their analysis with Eq. (58) are considered in § 2.8.2.

2.8.1. Q-factor of microcantilevers

Eq. (45) is often used as a good approximation in estimating the mass sensitivity of weakly damped mechanical resonators of various shapes and sizes, such as a microcantilever in air. However, more accurate calculations of the microcantilever resonance frequencies should take into account the dissipation of the resonator mechanical energy into thermal energy through various mechanisms related to inelastic phenomena in solid-state cantilever and viscous properties of the surrounding media (gas or liquid phase). In analogy to other types of resonators, the mechanical quality factor (or Q-factor) is commonly used to quantify energy dissipation in microcantilevers.

If W_0 and ΔW are, respectively, the mechanical energy accumulated (total energy stored) and dissipated (total energy lost) in the cantilever per vibration cycle, then the Q-factor can be defined as [9]:

$$Q = 2\pi \frac{W_0}{\Delta W}. \quad (59)$$

The Q-factor is inversely proportional to the damping coefficient γ and can be alternatively related to time constant τ_d of exponentially decaying oscillator amplitude during a ring-down process [9]:

$$Q = \pi\tau_d f_{res}. \quad (60)$$

The oscillation amplitude of a cantilever conforms to Gaussian distribution in the frequency domain and depends on the Q-factor as it is shown in Fig. 22 and simulated in § 2.9.3.2 “Simulation of microcantilever’s amplitude and phase spectra”.

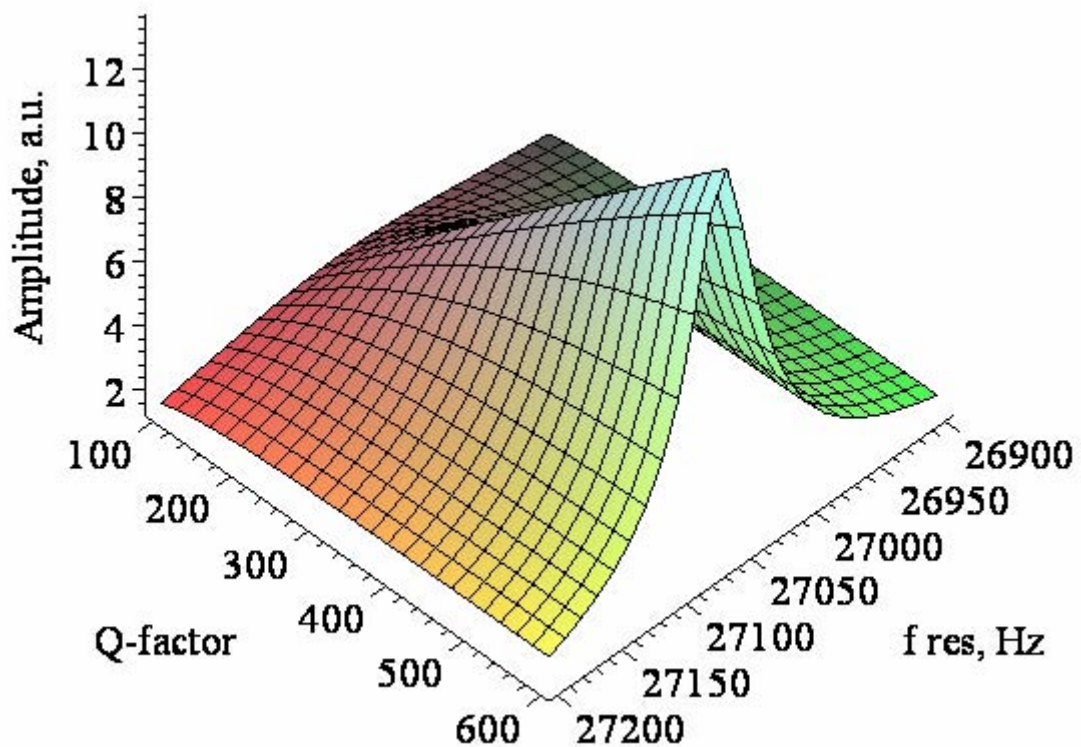


Fig. 22. How the oscillation amplitude depends on the frequency and the Q-factor. The resonance frequency is equal to 27.065 kHz.

Based on the spectral analysis (see Fig. 22 and Fig. 23), the Q-factor is frequently used to characterize the degree of the resonance peak sharpness. This means that a large and sharp resonance peak denotes a high Q-factor. This signifies the importance of the Q-factor for chemical sensors, since a sharp resonance peak is needed to accurately measure a resonance frequency change for monitoring the sorption processes.

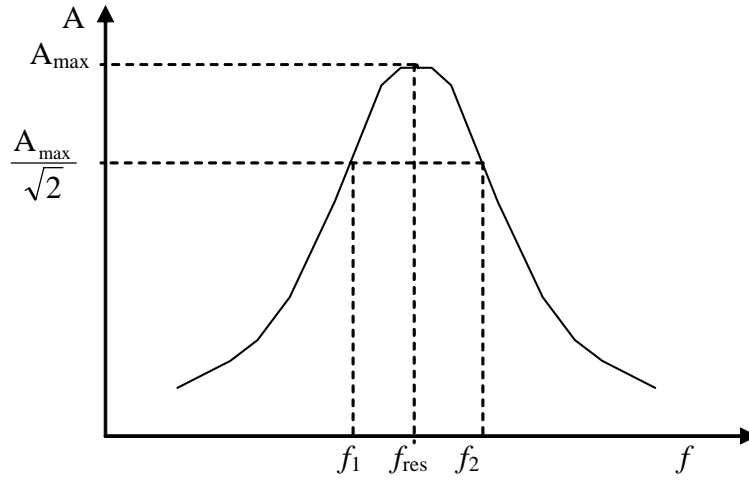


Fig. 23. Determination of Q -factor. $Q = \frac{f_{res}}{f_2 - f_1}$

Q -factor can be practically determined as resonance frequency f_{res} , which corresponds to the maximum oscillation amplitude A_{max} as illustrated in Fig. 23, divided by the bandwidth Δf_{-3dB} determined at the - 3 dB amplitude level $\frac{A_{max}}{\sqrt{2}}$ (sometimes the bandwidth is calculated at the half amplitude of the resonance frequency):

$$Q = \frac{f_{res}}{\Delta f_{-3dB}}. \quad (61)$$

Q -factor of microcantilevers is mainly affected by:

- viscous and acoustic damping, Q_a ;
- clamping (or support) loss, Q_s ;
- internal material loss, Q_i .

The total Q -factor can be related to the individual energy dissipation sources by:

$$\frac{1}{Q_{tot}} = \frac{1}{Q_a} + \frac{1}{Q_s} + \frac{1}{Q_i}, \text{ et cetera.} \quad (62)$$

Usually the lowest Q -factor, which determines the total Q -factor in Eq. (62), is the one limited by **viscous and acoustic damping** Q_a . This means that the pressure and atmosphere in the vicinity of the cantilever has a large influence on the total Q -factor, and the Q -factor increases as the total ambient pressure decreases. Obviously, increased damping of a microcantilever oscillator by the medium translates into lower Q -factor values as compared to the same oscillator in vacuum. Models of drag forces exerted on solid bodies in fluids can be

used to evaluate viscous damping effects [94]. A very important distinctive feature of viscous damping is that the damping force is proportional to the linear velocity of the vibrating cantilever, as will be represented in Eq. (80).

Q-factors of rectangular microcantilevers in air are typically in the range of 100 to 1000 while cantilever transducers in aqueous solutions rarely have Q-factors above 10. Very strong viscous damping in liquids makes resonant operation of microcantilevers, and, in turn, measurements of adsorbed mass using microcantilever sensors, rather challenging. In order to overcome the difficulties of resonant cantilever operation in liquids, cantilever transducers can be used as a part of a self-oscillating system with a positive feedback. Quality factor enhancement via driving force control has been substantially described by Tamayo et al. [95, 96].

The other damping mechanisms, involving clamping loss and internal friction within the microcantilever, were reviewed in recent studies [97]. As a rule, these dissipation mechanisms are associated with damping forces independent of the linear cantilever velocity.

Clamping loss Q_s (to the chip substrate through the cantilever support) has an insignificant contribution to the total dissipation in the case of longer microcantilever with high length-to-width and width-to-thickness ratios. Q-factors as high as 10^5 were reported for torsional butterfly-shaped resonators fabricated from single-crystal silicon [98].

Damping due to internal material parameters Q_i , such as crystal structure, lattice defects, etc. comprise **internal material loss**, Q_i .

The material of the resonator structure can substantially contribute to the total Q-factor though internal losses, which reduce the Q_i value. It has been reported that low-level impurity single-crystalline silicon resonators have Q-factors of approximately 10^6 in vacuum, while highly boron doped single-crystalline silicon resonators typically have a Q-factor of approximately 10^4 [99]. This reduction of two orders of magnitude is due to the boron impurities, which cause structural defects. In theory a perfect crystal structure has no losses and the higher the defect concentration the larger the internal losses. For instance, polysilicon, which is not a crystalline structure, generally has lower Q_i value (approximately $10^2 \dots 10^3$) than single-crystal silicon [12].

Internal friction can be particularly linked to thermoelastic dissipation, motion of lattice defects, phonon-phonon scattering, and surface effects [100, 101]. The thermoelastic dissipation and phonon-phonon scattering limit Q-factors as high as 10^6 to 10^8 , which can hardly be observed experimentally due to the contribution from other dissipation mechanisms present in real MEMS.

It is important to emphasize that both the resonance behaviour of any microcantilever and its off-resonance thermal noise given by Eq. (46) are critically dependent on the Q-factor.

Therefore, the Q-factor is one of the important characteristics of cantilevers operating in both resonance and static regimes.

2.8.2. Experimental results on damping phenomena

The measurement cell was connected to the Pfeiffer vacuum pump (Mod.: DUO 2,5 AC), which was able to exhaust the atmosphere down to 2...10 Pa, depending on the number of the cantilevers installed. Fig. 24 shows a cantilever amplitude and phase dependencies at both low and ambient pressures. The vacuuming time was 1 hour and 20 min.

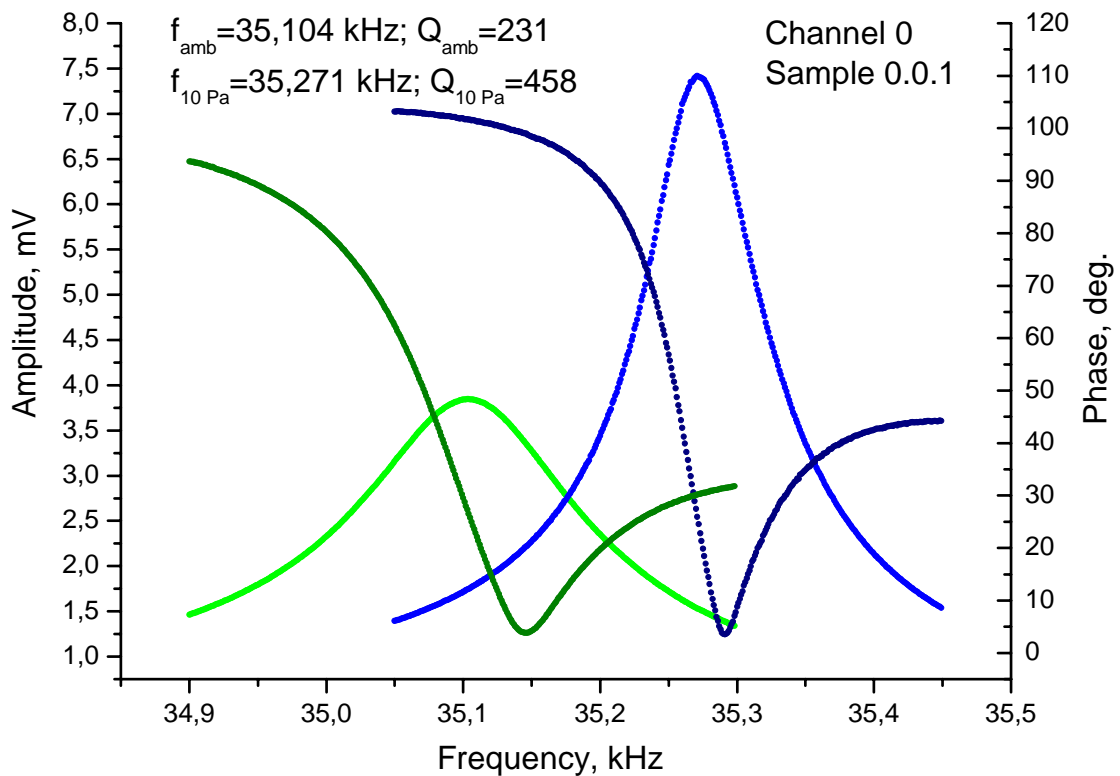


Fig. 24. Experimentally measured amplitude and phase spectra of an uncoated cantilever under ambient pressure (left) and 10 Pa (right).

It is clearly seen from Fig. 24 that resonance frequencies were shifted about 150 Hz to the right in vacuum. This can be explained by both lower damping effect and also forced desorption of adsorbed molecules (first of all water molecules) normally presented at ambient conditions at the cantilever surface. The damping changes are derived from calculated Q-factors, which were increased in vacuum (almost 2 times for uncoated cantilevers and 1.3...1.8 times for polymer-coated cantilevers).

The resonance frequency shift due to viscous and acoustic damping, which is strictly dependent on the width of the cantilever beam, can be simulated according to Eq. (58). The density of humid air as the damping media in Eq. (58) can be calculated as a mixture of ideal gases:

$$\rho_{air} = \frac{p_d}{R_d \cdot T} + \frac{p_v}{R_v \cdot T}, \quad (63)$$

where p_d and p_v are partial pressure of dry air and pressure of water vapour respectively, $R_d = 287.05$ J/(kg·K) and $R_v = 461.495$ J/(kg·K) are specific gas constants for dry air and for water vapour respectively, T is absolute temperature. In its own turn, the vapour pressure of water p_v may be calculated from the saturation vapour pressure p_{sat} and relative humidity Rh :

$$p_v = Rh \cdot p_{sat}, \quad (64)$$

where the saturation vapour pressure can be approximated as:

$$p_{sat} = 0.061078 \cdot 10^{\frac{7.5T - 2048.625}{T - 35.85}}. \quad (65)$$

Partial pressure of dry air p_d can be found as:

$$p_d = p_{abs} - p_v, \quad (66)$$

where p_{abs} denotes absolute pressure in the cantilever cell.

Thus, at given experimental conditions (temperature 299.5 K, absolute pressure 99300 Pa, and relative humidity 32 %), the density of humid air is calculated to be 1.15503 kg/m³. It is worth to note that density of dry air calculated at same pressure and temperature outputs 1.15498 kg/m³, and therefore influence of water vapour (second term in Eq. (63)) can be neglected. Lowering of the eigenmode frequencies in air in respect to the corresponding cantilever eigenfrequencies in vacuum has been simulated according to Eq. (58) and depicted in Fig. 25.

In particular, if resonance frequency of the cantilever from Fig. 24 is 35104 Hz at ambient conditions, its resonance frequency in vacuum is estimated to be 35359 Hz. The experimentally measured value is, however lower: 35271 Hz. It can be explained by the facts of residual damping and mass load of the cantilever beam at the experimentally measured residual pressure 10 Pa.

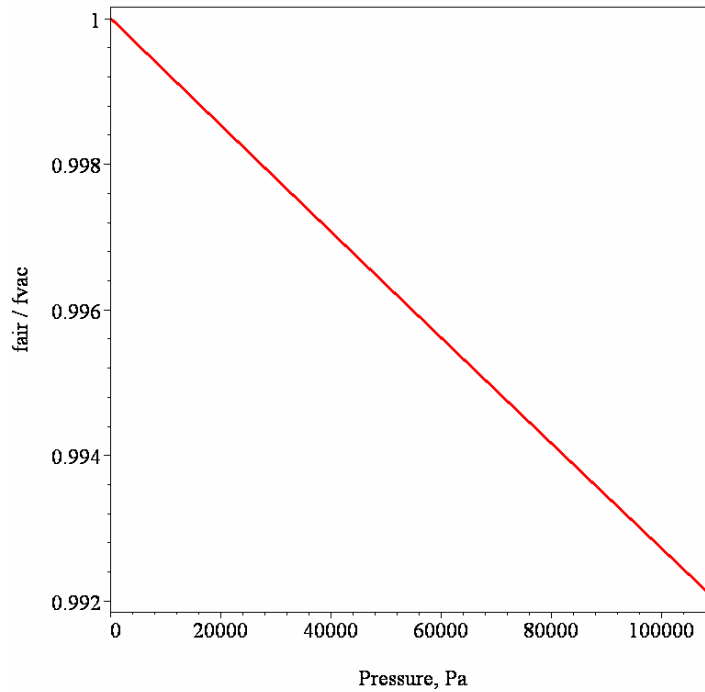


Fig. 25. Lowering of the resonance frequency in air atmosphere in respect to the cantilever resonance frequency in vacuum.

A steeper slope of the phase curve observed at higher Q-factors (e.g., in vacuum) makes the cantilever more sensitive not only in amplitude modulation, but also in the phase shift mode, which will be discussed in detail in § 2.9.3.1.

2.9. Actuation and detection techniques for microcantilevers

2.9.1. Detection methods

The following detection methods are applicable for measuring static deflection and/or dynamic motion of microcantilever transducers:

- **Capacitive detection** implies measuring the capacitance between two separated electrodes with motion-modulated distance between them [102].
- **Optical detection** is used in most AFM microscopes and cantilever-based (bio-)chemical sensors, which operate in static bending mode. The movement of the cantilever is detected by a reflected laser beam focused on the resonator and a position-sensitive detector.
- **Piezo-electric detection** technique requires deposition of piezo-electric material, such as ZnO, on the cantilever. Due to a piezo-electric effect, transient charges are induced in the piezo-electric layer when the cantilever is deformed [103].

- **Strain gauge** with deflection-induced resistance modulation can be employed by, e.g., discontinuous gold film evaporated onto interdigitated electrodes in the area of maximal stress. By applying a bias voltage between the electrodes, the tunnelling current is modulated with the tunnelling gap distance changes between the nanoparticles. Our experiments have shown gauge factors of such nanoparticle (discontinuous) films in the range of about 200...300, which has not been reported as a microcantilever read-out elsewhere.
- **Piezo-resistive detection** requires the presence of one or more piezo-resistors on the cantilever. The idea is that when the cantilever bends, the resistance of the piezo-resistor changes due to the stress in the material. This is a very attractive technique since both single-crystal Si and poly-Si are good piezo-resistive materials at the right doping level. Moreover, on-chip read-out detector based on piezo-resistive principle avoids using of a traditionally implemented expensive and cumbersome laser and optical equipment, and the need of its adjustment. Piezo-resistive read-out of the TASNANO cantilevers is described in the next paragraph.

2.9.1.1. Integrated piezo-resistive read-out

Piezo-resistive effect in single-crystal silicon, which depends on the crystal orientation, dopant type and the doping level, denotes variation of its local resistivity under mechanical stress. Higher sensitivity is observed for ultra-shallow p-type piezo-resistors aligned in $\langle 110 \rangle$ crystal direction. Piezo-resistive read-out of our cantilevers comprises 4 ion-implanted piezo-resistors, which are combined in the Wheatstone-bridge configuration. They are placed in the area of maximal mechanical stress on the cantilever surface, and therefore are able to the most optimal modulation of the constant bias voltage U_{bridge} (Fig. 26).

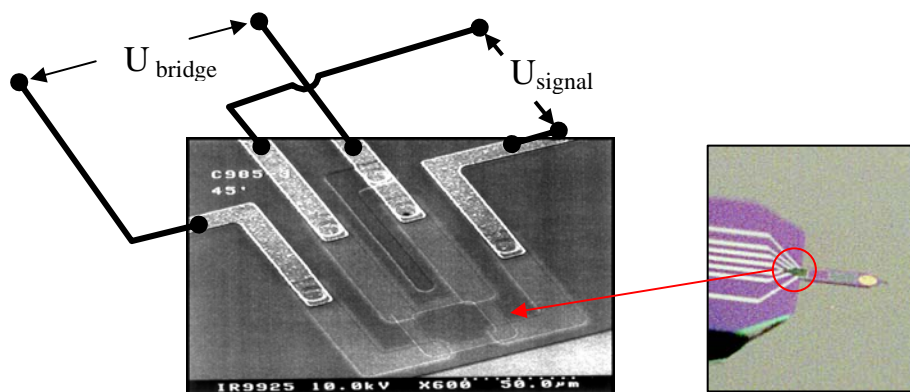


Fig. 26. Electron micrograph of the read-out unit (a) and its position on the cantilever (b).

The values of the implanted piezo-resistors can be defined by:

$$R = \frac{\rho_r L_r}{A_r}, \quad (67)$$

where R is the resistance value of each resistor in the bridge, ρ_r is the resistivity of the doped silicon, L_r is the length of the resistor and A_r is the cross-sectional area of the resistor.

Modulated output voltage U_{signal} provide us with information about cantilever deflection or its oscillation frequency (DC component of the of the stressed cantilever or AC component of the oscillated cantilever correspondingly). The main reason to implement piezo-resistive read-out technique is possibility to miniaturise the cantilever-based sensor. Moreover, absence of adjustments and expenses inherent in laser scheme, compatibility with standard CMOS-technology, easy temperature control and compensation, and ability to operate in non-transparent media are other incontrovertible advantages of the implemented read-out technique. Fig. 27 shows schematic diagram of the read-out unit.

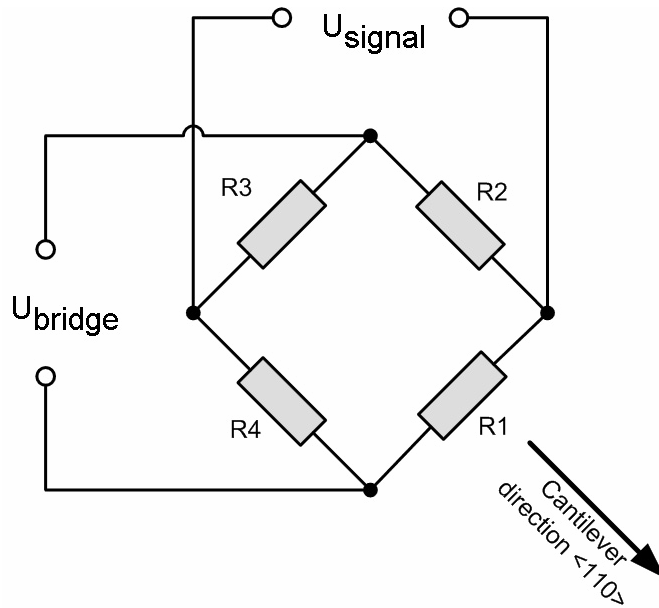


Fig. 27. Schematic diagram of the read-out unit.

For the depicted circuit the output signal is governed by the equation:

$$U_{\text{signal}} = U_{\text{bridge}} \frac{\Delta R_1 + \Delta R_3 - \Delta R_2 - \Delta R_4}{4R}. \quad (68)$$

Since a balanced bridge circuit has $\Delta R_i = 0$, the output signal is also zero. However, some discrepancy of the resistances R_i in real Wheatstone bridges results in $U_{\text{signal}} > 0$, which is called “offset voltage”. Bending of the cantilever results in the resistances variations:

$$\Delta R_1 = \Delta R_3 = \pi_T \sigma R, \quad (69)$$

and

$$\Delta R_2 = \Delta R_4 = \pi_L \sigma R, \quad (70)$$

where σ is mechanical stress in the material, $\pi_T = -66.3 \cdot 10^{-11} \text{ Pa}^{-1}$ denotes the transversal piezo-resistive coefficient (i.e. mechanical stress perpendicular to the resistor), $\pi_L = 71.8 \cdot 10^{-11} \text{ Pa}^{-1}$ is the longitudinal piezo-resistive coefficient (i.e. stress parallel to the resistor). These values of π are valid for a doping level of approximately 10^{17} cm^{-3} [6].

Eq. (68)-(70) lead to the following expression for the output signal:

$$U_{\text{signal}} = U_{\text{bridge}} \frac{\pi_T - \pi_L}{2} \sigma. \quad (71)$$

The signal from the oscillating cantilevers consists of an AC and a DC components. The resonance frequency of the cantilevers is determined by demodulation of the amplified AC component of the sensor signal. The Wheatstone bridge design, where all 4 resistors are placed on the cantilever, also ensures better thermal stability and easy offset voltage compensation.

2.9.2. Excitation methods

Electrostatic excitation uses two electrodes, where one of the electrodes is the cantilever. By applying an alternating voltage between the driver plate and the cantilever, a periodic force is exerted on the cantilever, thus actuating it. This technique is very good when working in vacuum, since air would damp the motion on the resonator. Otherwise, one has to ensure easy airflow around the resonator. Electrostatic excitation is especially attractive in combination with capacitive detection method.

Dielectric excitation also uses two electrodes that are separated by a dielectric material, thus the whole structure is the cantilever. Here, just like with electrostatic actuation, one applies an alternating voltage between the upper and bottom layer electrodes. This voltage will pull the two layers together, thus deforming the dielectric layer causing lateral stress, which will actuate the cantilever. An important advantage of this method is avoiding of any external structure, because the actuator is fully integrated onto the cantilever. However, the resonator has to be multi-layered, which increases the thickness and complexity of the resonator and thus the minimum detectable mass.

Integrated piezoelectric excitation is to sandwich a piezoelectric material, such as single-crystalline quartz, between two metal contacts, which is then placed on a silicon

cantilever. By applying an alternating voltage across the piezoelectric material, one can actuate the cantilever. The drawback of this technique concerns compatibility issues with conventional silicon technology. Modelling of integrated piezoelectric excitation technique is presented in [103].

External piezoelectric excitation utilizes the cantilever holder, which is placed (usually glued) upon a commercial quartz crystal. The drawback is that on-chip integration is not provided.

Resistive heating excitation implies expansion of the cantilever material due to the stress exerted by local rise of the temperature around the integrated heating resistor. Usually the resistor is an integrated diffused resistor, or poly-Si that is deposited on the resonator.

Optical heating excitation implies thermal expansion of the cantilever material by heating with a focused laser beam or light source. The spot size of a typical optical laser is around 10 μ m, which limits the minimum size of the resonator.

Bimorph-effect excitation is similar to the resistive heating, but the cantilever bends mostly because of the different thermal expansion coefficients of the cantilever material and the heater. TASNANO-cantilevers contain integrated heater, which is considered in the next paragraph.

2.9.2.1. Integrated bimorph actuator

The stresses on the cantilever surface may be induced not only by adsorption, but also thermally. Simple models are applicable to thermally induced stresses and concomitant deformations of microcantilevers made of two layered materials with different coefficients of thermal expansion. Theoretical evaluation of bimetal thermostats reported in [104] provided an analytical expression for the radius of curvature of a bimaterial cantilever as a function of a temperature change. This deformation resulting from unequal thermal expansion of each layer has been used extensively as an operation principle of thermostats and often referred to as the bimetallic effect. Fig. 28 is a conceptual drawing of the cantilever-integrated bimorph-effect actuator. Taking into account the length of the cantilever l , the respective deflection of the tip can be expressed as:

$$\Delta z = \left[\frac{l^2}{2R} \right] = 3K\Delta Tl^2, \quad (72)$$

where

$$K = \frac{(\alpha_1 - \alpha_2)(h_1 + h_2) \frac{1}{h_2^2}}{4 + 6\left(\frac{h_1}{h_2}\right) + 4\left(\frac{h_1}{h_2}\right)^2 + \left(\frac{h_1}{h_2}\right)^3 \left(\frac{E_1}{E_2}\right) + \left(\frac{h_2 E_2}{h_1 E_1}\right)}, \quad (73)$$

where h_1 and h_2 are the thicknesses of the two layers of the bimaterial plate, E_1 and E_2 are the Young's moduli, and α_1 , and α_2 are the thermal expansion coefficients for the materials of these layers, respectively. Tab. 4 summarizes some important materials' properties [105].

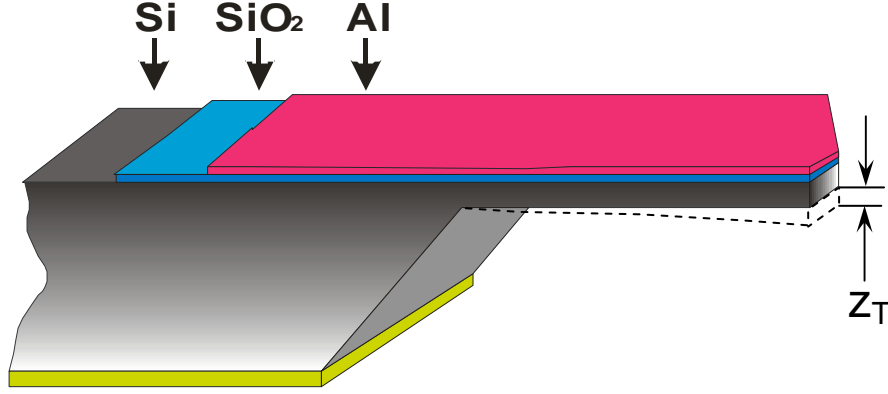


Fig. 28. Multilayered structure of the bimorph-effect cantilever.

Material	Si	SiO ₂	Al
Young's modulus, E, GPa	170	75	70
Thermal expansion coefficient, α , K ⁻¹	$2.6 \cdot 10^{-6}$	$0.25 \cdot 10^{-6}$	$23 \cdot 10^{-6}$

Tab. 4. Young's moduli and thermal expansion coefficients for silicon, silicon dioxide, and aluminium.

More recently, various modifications of Eq. (72) have been used to predict thermally induced deflections of microscopic bimaterial cantilevers [106, 107]. In order to evaluate calorimetric sensitivity of a bimaterial cantilever, Barnes *et al.* [107] combined Eq. (72) with the expression for a thermal flux along the cantilever and found that the deflection of the cantilever tip Δz is given by:

$$\Delta z = \frac{5}{4} K \frac{l^3}{\lambda_1 h_1 + \lambda_2 h_2} P, \quad (74)$$

where λ_1 and λ_2 are the thermal conductivities of the two layers and P is the absorbed power.

Femto-Joule level calorimetric sensitivity of conventional AFM cantilevers demonstrated experimentally by Barnes *et al.* [107] is consistent with the theoretical predictions made using Eq. (74).

Thermally actuated cantilevers employed in the presented work have the meander-shaped aluminium heater positioned as it is shown in Fig. 3, where the thickness of silicon is normally 3...5 μm , SiO_2 : 0.5...2 μm , and aluminium layer: 0.8...1.5 μm .

Generally, the actuator supply voltage may consist not only of AC component, but also DC component, which is further referred to as “bias voltage”. For cantilevers actuated with an external oscillating quartz resonator, the bias voltage introduces no effect, as it is shown in Fig. 29.

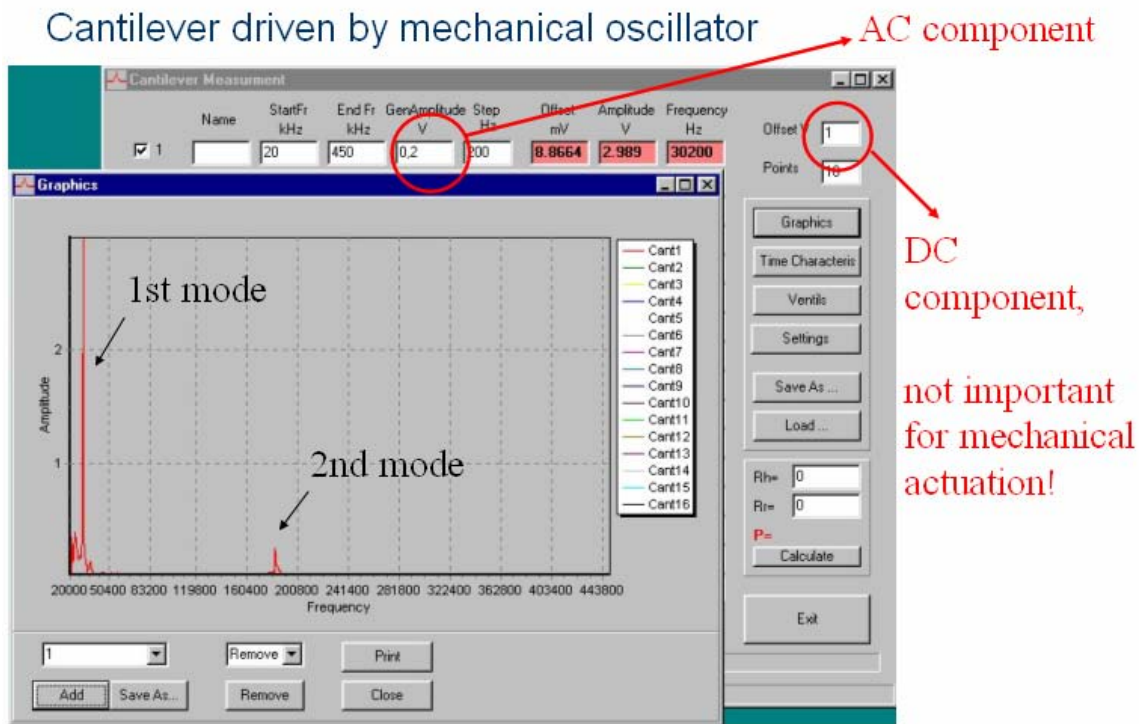


Fig. 29. Screenshot of a cantilever response spectrum gathered under mechanical actuation.

On the contrary to the mechanical actuation, the bias voltage of the input signal (to put this in another way, its DC component, U_{DC}) supplied to the integrated heater plays a significant role for the cantilever operation. First of all, it leads to the appearance of additional peaks in the read-out spectrum of the cantilever in all eigenmodes, as explained by Eq. (75) and Fig. 30. Let's consider the origin of the spectrum modification by the example of the first mode. The input power supplied to the heater can be written as:

$$\begin{aligned}
 P &= \frac{U_{heater}^2}{R_{heater}} = \frac{1}{R_{heater}} (U_{DC} + U_{AC} \cdot \cos \omega t)^2 = \frac{1}{R_{heater}} (U_{DC}^2 + 2U_{DC}U_{AC} \cos \omega t + U_{AC}^2 \cos^2 \omega t) = \\
 &= \frac{1}{R_{heater}} \left(U_{DC}^2 + \frac{U_{AC}^2}{2} + \frac{U_{AC}^2}{2} \cdot \cos 2\omega t + 2 \cdot U_{DC} \cdot U_{AC} \cdot \cos \omega t \right)
 \end{aligned} \tag{75}$$

Eq. (75) suggests that there should be one steady and two frequency-dependent components in the output spectrum of the thermally excited cantilever. Therefore, if U_{DC} is set to zero, the corresponding eigenfrequency peak defined by $\cos \omega t$ component in Eq. (75) will disappear, as it is illustrated in Fig. 30 for natural resonance frequency. The difference in the two presented screenshots is only whether $U_{DC} = 1$ V (left side) or $U_{DC} = 0$ V (right side). Alternative input voltage remains the same ($U_{AC} = 2$ V) in both cases.

$$P = \left(U_{DC}^2 + \frac{U_{AC}^2}{2} + \frac{U_{AC}^2}{2} \cdot \cos 2\omega t + 2 \cdot U_{DC} \cdot U_{AC} \cdot \cos \omega t \right) \frac{1}{R_{heater}}$$

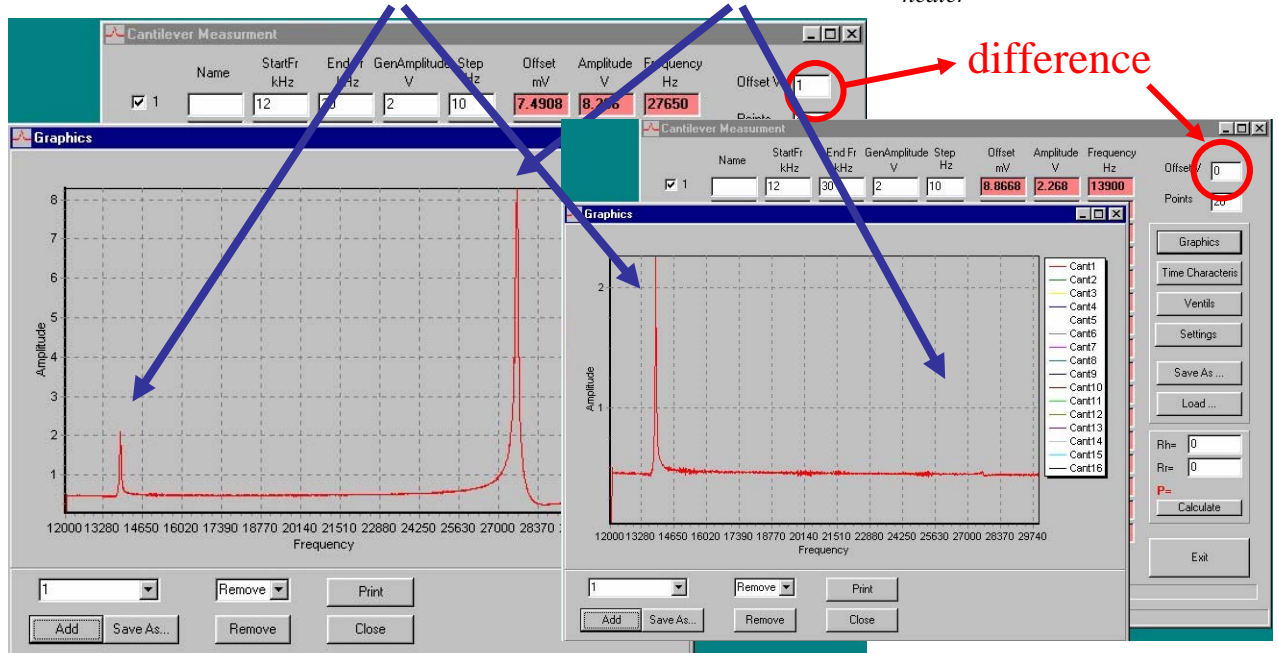


Fig. 30. First eigenmode's output spectrum of thermally excited cantilever with (left), and without (right) bias voltage U_{DC}

As one can conclude from Eq. (75) and Fig. 30, output frequency spectrum of the first eigenmode of the thermally excited cantilever contains not only natural resonance peak, but also satellite peak at its half-frequency. Moreover, natural resonance peak disappears if the bias voltage $U_{DC} = 0$ (see Eq. (75)).

The DC component of the input power has also stronger influence on the resonance frequency drift in comparison with the AC component. Fig. 31 shows resonance frequency peaks for four different supply voltage combinations.

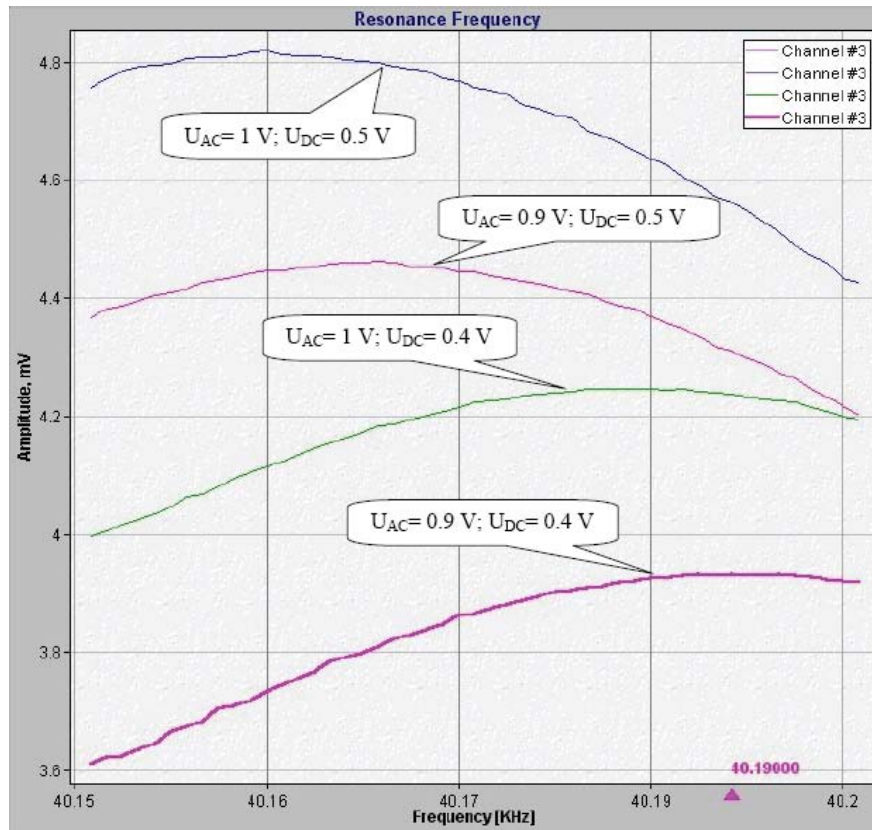


Fig. 31. Resonance frequency variations under different actuator supply voltages.

Lowering of the resonance frequency at higher voltages occurs due to the thermally induced changes in cantilever stiffness, first of all because the Young's modulus of silicon decreases with heating (see Fig. 20). Influence of the heating on the piezo-resistive read-out should be relatively smaller because (i) there is a heavy heat sink by silicon bulk material, (ii) the read-out and the heater are spaced apart, and (iii) all 4 piezo-resistors are placed to be at nearly the same temperature. It is clearly seen that increase of the DC bias at 0.1 V has stronger effect than the same variation of the AC component. That is obvious, because the effective voltage of the AC component is $\sqrt{2}$ times lower. The input effective power dissipated at the heater is then:

$$P = \frac{(U_{AC}/\sqrt{2} + U_{DC})^2}{R_{heater}}. \quad (76)$$

According to the design of our measurement system (see Chapter 3.), DC component is two times higher than bias voltage entered through the program interface: $U_{DC} = 2 \times \text{Bias [V]}$. On the other hand, the entered bias voltage should be two times lower than AC component: $\text{Bias [V]} = \frac{U_{AC}}{2}$ in order to avoid signal distortions in the preamplifier. Taking into account these considerations, Eq. (76) can be re-written to the following empirical expression for the dissipated power:

$$P = \frac{(U_{AC}/\sqrt{2} + U_{DC})^2}{R_{heater}} = \frac{2.914 \cdot U_{AC}^2}{R_{heater}}. \quad (77)$$

For instance, if $U_{AC} = 0.5$ V and $U_{DC} = 0.25$ V, the power dissipated at a heater $R = 14.7$ Ohm (averaged value) will be then $P = 50$ mW.

Influence of AC and DC component of the actuation signal was measured for single cantilever coated with styrene-acrylonitrile copolymer (SAN) at ambient conditions (Fig. 32). This experiment also confirms stronger influence of the DC component on the measured signal through the heating of the cantilever beam.

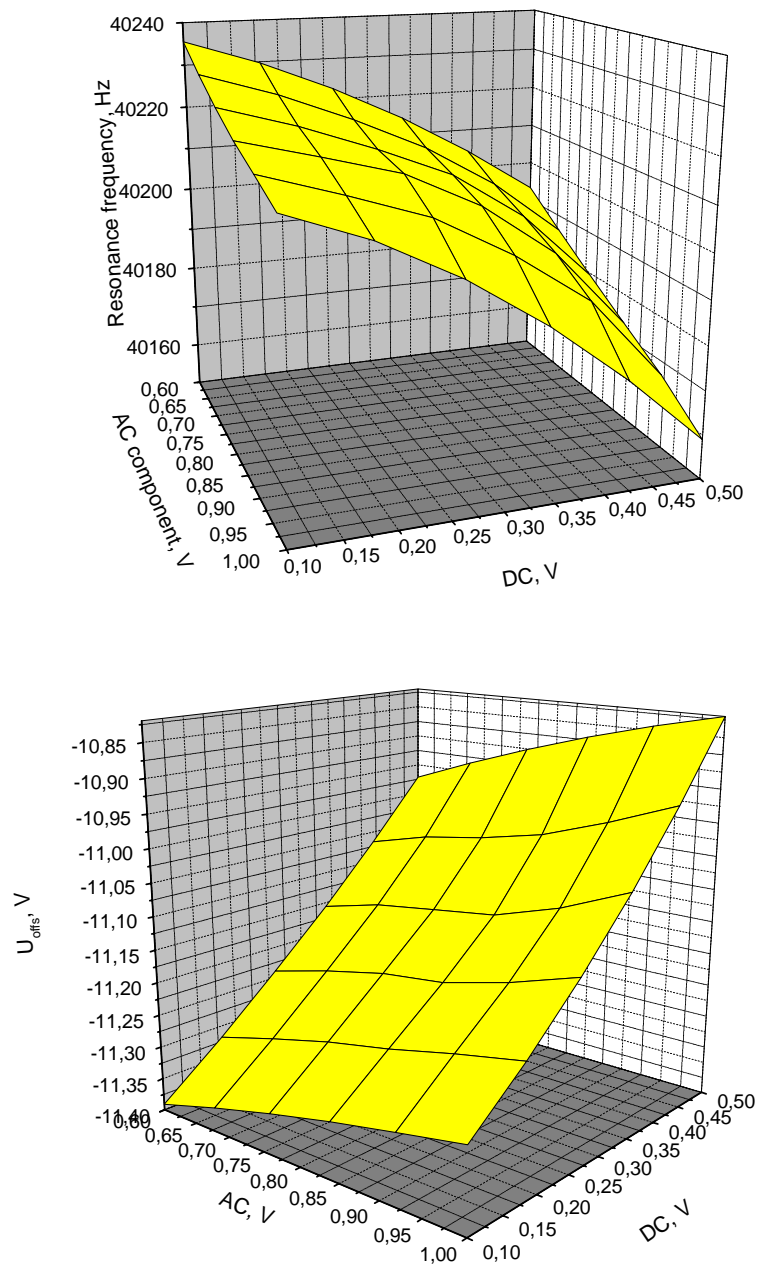


Fig. 32. Resonance frequency (a) and offset voltage (b) measured versus AC and DC component of the actuation signal of a cantilever coated with styrene-acrylonitrile copolymer (SAN).

Accumulated heat and consequent changes in Young's modulus of the silicon cantilevers (refer also to § 2.7 and Fig. 20) result in the resonance frequency shift to its lower values. Fig. 32 (a) shows experimentally derived frequency shift up to 80 Hz by varying DC and AC components of the voltage fed to the actuator within their total operable ranges. It means that temperature influence has generally stronger impact on the cantilever's resonance behaviour, thus the initial baseline measured in time domain has to be monitored before each experiment. The output offset voltage, which is a measure of the cantilever bending, is also temperature-dependent, thus it is more influenced by the DC component of the input signal (Fig. 32, b). As Fig. 32 (b) implies, the bimorph-actuated cantilever bends in rather linear manner in respect to the voltages supplied to the actuator. Nature of the offset voltage and its application as an additional read-out parameter is discussed in the next paragraph.

2.9.3. Piezo-resistive detection principles: offset voltage, frequency shift, phase shift

Measure of static cantilever bending using piezo-resistive Wheatstone bridge read-out can be derived through the offset voltage, which is DC component of the output signal of the bridge U_{signal} . The offset voltage is originated from resistance misbalances of the resistors comprising the Wheatstone bridge due to both technological mismatches and variations in response to mechanical stress. The more cantilever is stressed, the more offset voltage is shifted from its normal value. Many our experiments show that offset voltage shift versus analyte concentration is not as linear as resonance frequency shift. That is why we mostly relied on the resonant mode operation. Our measurement system design enables simultaneous measurement of offset voltage and resonance frequency so that both dynamic and static cantilever behaviour can be monitored simultaneously (Fig. 33).

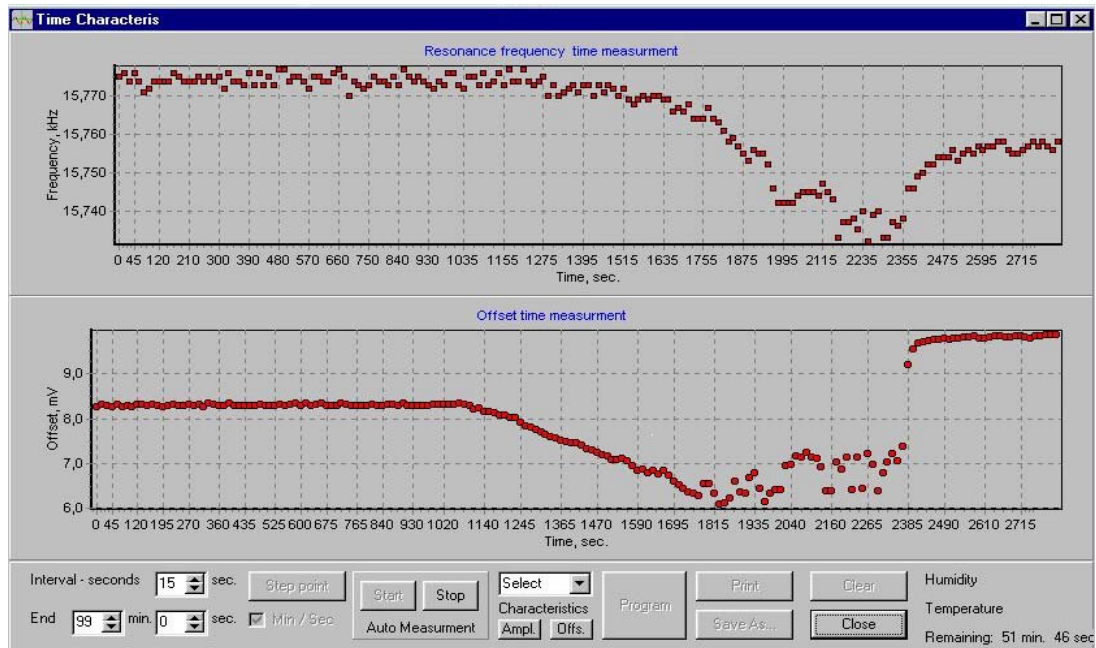


Fig. 33. Variations of the resonance frequency and offset voltage for thermally actuated cantilever coated with thin layer of photoresist AZ1518 under exposure to ethanol vapours with variable time-dependent concentrations (from 0 to 93%).

Many experiments carried out in the frame of this work on differently functionalized cantilevers confirmed rather adequate and linear responses in terms of the resonance frequency shift. The resonance frequency is monitored by scanning certain frequency range, where the AC component of the bridge's output signal is anticipated to reach its maximum. The scanning implies a discrete increment of the actuation frequency. Such a way, practical resonance detection is always a compromise between the scanning time and the frequency resolution. In this work, the compromise has been found as approximately 1...1.5 min to scan the consequence of 8 cantilevers versus 1 Hz scanning frequency increment. Despite automated resonance tracking function, which additionally reduced the scanning range, was introduced into the system, neither the scanning time nor the resolution were appropriate for measuring fast transition processes or defining the sensitivity thresholds. Introduction of the phase shift detection principle made it possible to overcome both the limitations without any additional drawback. Finally, 8-cantilever array has been scanned for approximately ten seconds with sensitivity resolution of approximately 0.25 Hz in the frequency equivalent.

2.9.3.1. Principle of phase-shift detection in cantilever sensors

Resonance frequency of a cantilever is experimentally defined by scanning frequency range near the resonance, converting AC component of the Wheatstone bridge output signal into

DC voltage, and defining the frequency, where this voltage reaches its maximum (Fig. 35). The widely used amplitude detection methods exhibit some disadvantages related to approximately large time constant of the amplitude variations $\tau_{AM} \approx \frac{2 \times Q}{f_0}$, and approximately small amplitude changes at the resonance frequency f_0 . In the phase shift mode, the change of the signal phase relative to the actuation signal, is measured. This phase shift occurs mostly due to resisting force, which slows down cantilever oscillations such the way that the response signal is delayed to the actuation signal, as it is shown in Fig. 34.

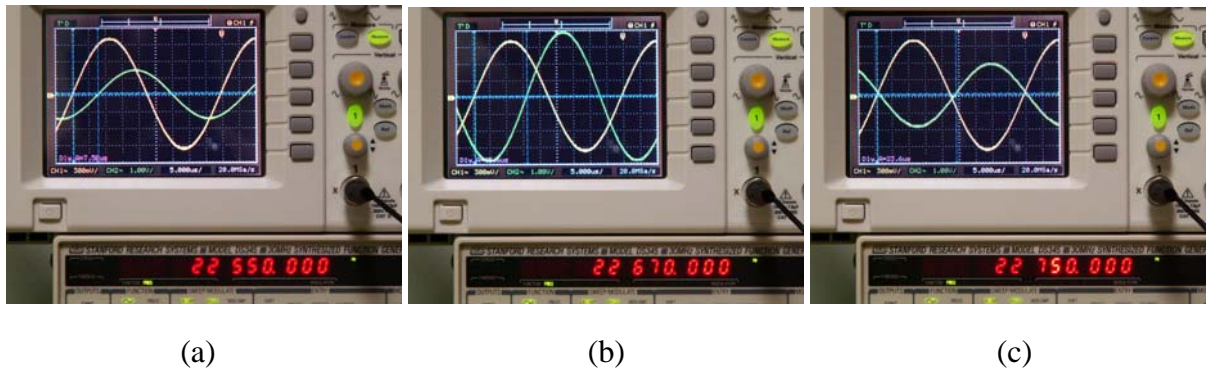


Fig. 34. Phase shift between the actuation and read-out signals: oscillation below the resonance frequency (a); oscillation at the resonance (b); oscillation above the resonance (c).

The phase shift occurs on a time-scale of $\tau_\phi \approx \frac{1}{f_0}$, and the phase is changed in linear manner around the resonance frequency. These two benefits make the phase shift detection method very promising, especially if both high speed and high sensitivity are required. As one can see from Fig. 35, which represent experimentally measured data, steep phase slope (Fig. 35, b) makes phase detection method more susceptible to the input stimuli than some uncertainty of the amplitude peak detection (Fig. 35, a). Higher Q-factors result in sharper amplitude peaks as well as steeper phase slope. Such the way, higher Q-factors provide a better sensitivity to the input stimuli (adsorbed mass, pressure, temperature, etc.)

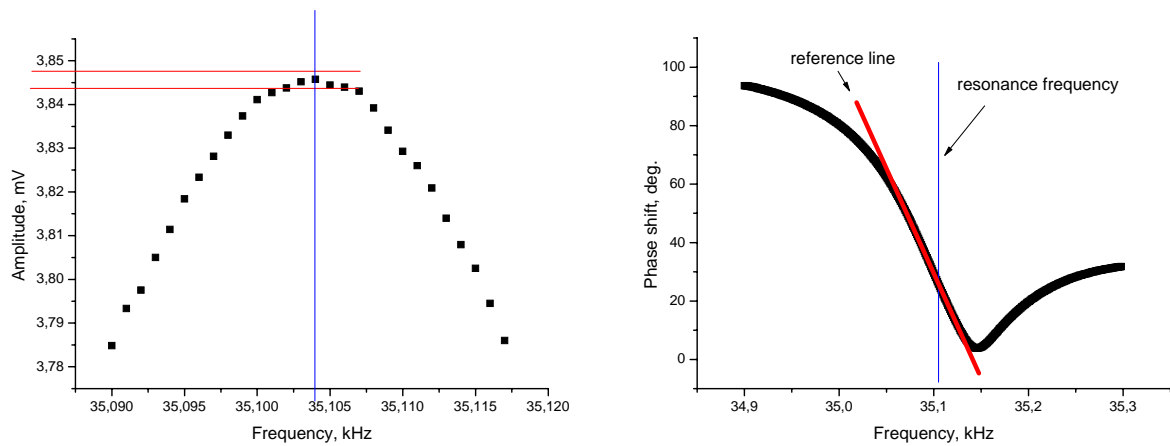


Fig. 35. Experimentally obtained data for amplitude (a) and phase (b) detection methods.

Fig. 36 presents the typical amplitude and phase characteristics of an ideal resonance system.

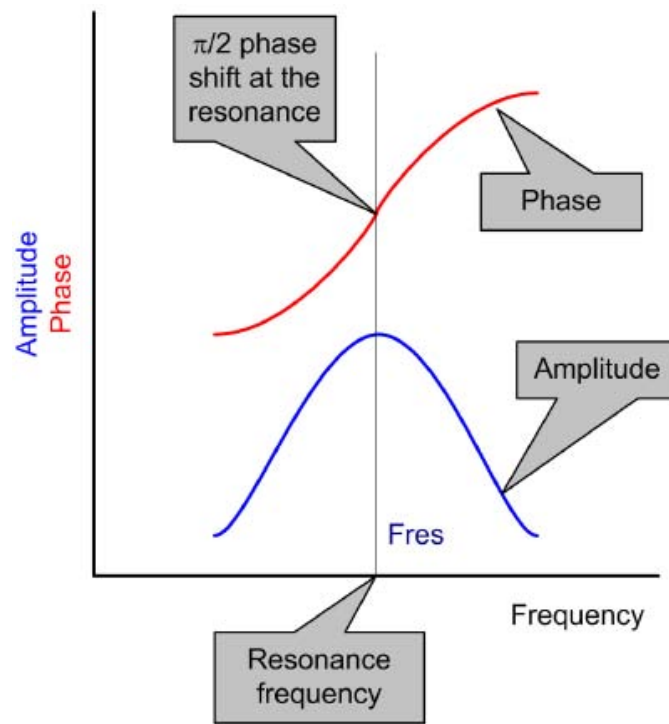


Fig. 36. Amplitude and phase curves of an ideal resonance system.

Here, the red curve represents the phase shift between excitation signal and output signal of the resonance system. In our case, the excitation signal is the signal from DDS generator (including output buffer if any); the output signal of the system is taken from the piezo-resistive bridge. It is clearly seen that within some certain range around the resonance frequency, the phase shift is rapidly and linearly changed. In an ideal resonance system, this phase shift is $\pi/2$ at the resonance.

Based on this behaviour, a very simple detection principle can be developed: the cantilever is forced to oscillate at some fixed central frequency (which can be equal, or near to the resonance frequency). The output from the cantilever and the output from the oscillator are fed to the phase comparator (Fig. 37).

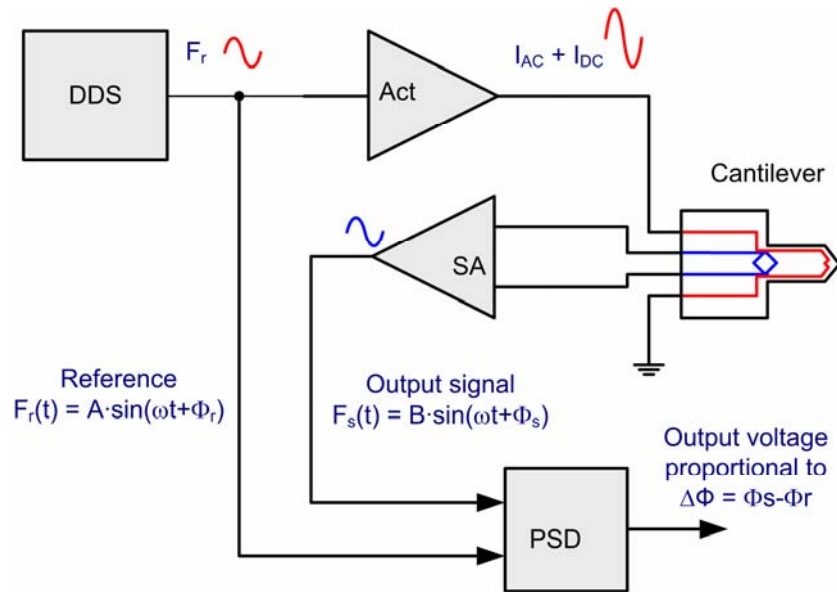


Fig. 37. "Phase-shift" based detection system. Designations: DDS – Direct Digital Synthesis Generator; Act – Actuator Driver; SA – Sensor Amplifier; PSD – Phase Shift Detector.

Due to the force acting on the sensor, both the resonance curve, and phase shift curve are shifted. As the reference frequency is fixed, the output of the phase shift detector is changed. The principle is illustrated in Fig. 38.

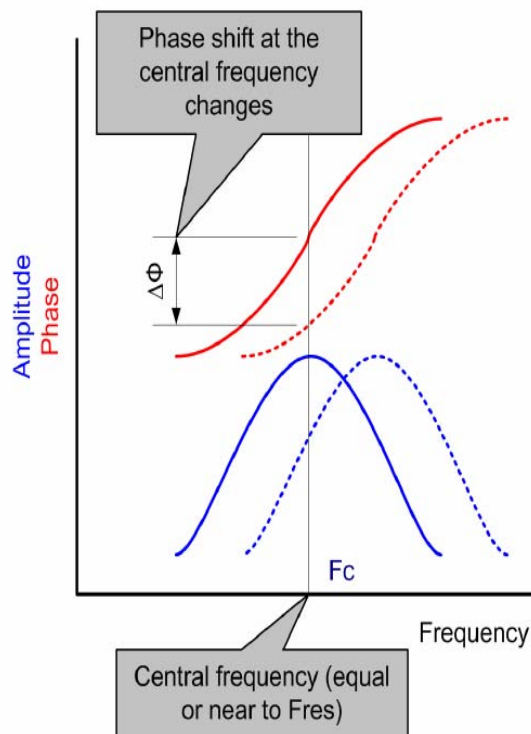


Fig. 38. Principle of phase-shift detection.

In Fig. 38, the solid lines represent initial amplitude/phase curves; the dashed ones represent the shifted amplitude/phase curves. The measured phase-shift is clearly seen. Real resonance systems show similar behaviour; the main difference is: at the resonance, the phase difference between the excitation and output could be different from $\pi/2$.

Fig. 39 presents the amplitude/phase characteristics of cantilever with piezo-resistive read-out and integrated thermal actuator taken from the real measurements using setup described in Chapter 3.

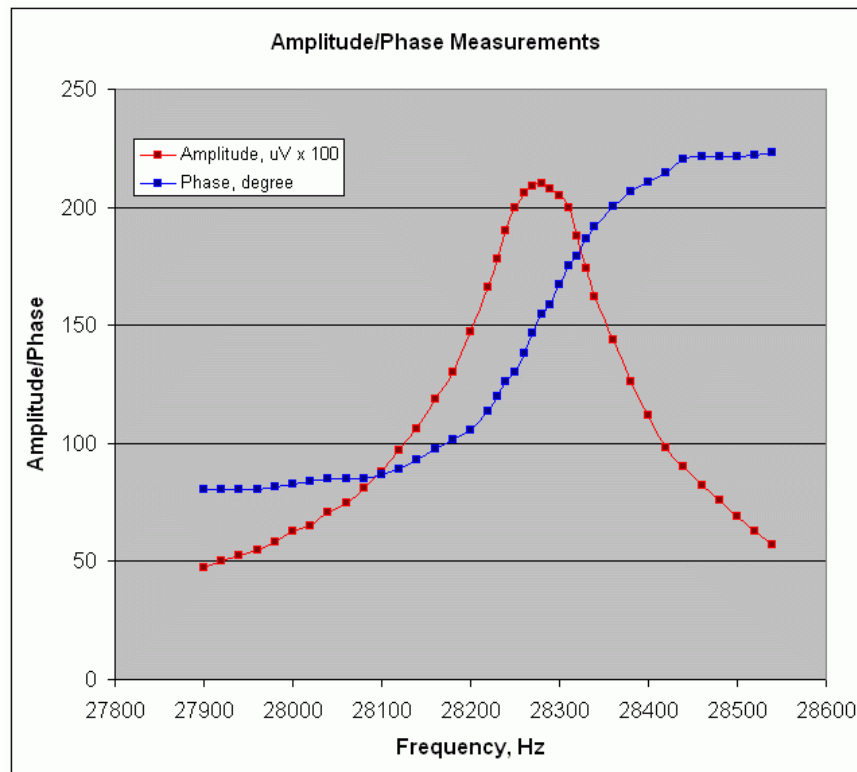


Fig. 39. Amplitude/Phase curves of a cantilever with piezo-resistive read-out and thermal actuator.

As it is seen from the picture, the phase shift between actuator and sensor output at the resonance is approximately 110 degrees, but the behaviour of the sensor is the same as in the ideal resonance system:

- the sensor exhibits a strong phase shift around the resonance;
- the phase-shift curve is one-to-four quadrant symmetrical with respect to the resonance frequency line;
- the phase-shift change is linear in some narrow region around the resonance.

In fact, the phase-shift curve is transposed by some additive constant phase difference, as shown in Fig. 40.

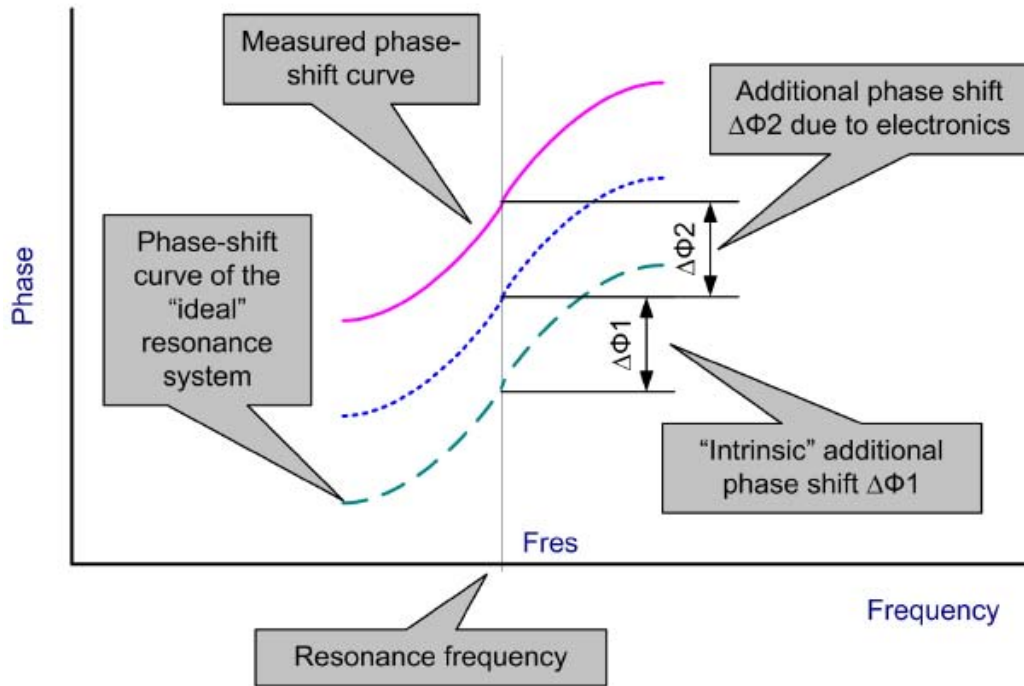


Fig. 40. Phase-shift curve of the real system (electronics + sensor).

The additive phase difference is sum of two components:

- “Intrinsic” additional phase shift, due to the physical effects in the sensor, and
- “Measurement” phase shift, due to the measurement electronics (buffers, amplifiers, filters, etc).

“Intrinsic” phase shift of a cantilever is simulated with Maple ® in the next paragraph, whereas experimentally measured “extrinsic” phase shift is on average 60 degrees. To put it differently, the initial baseline of the phase shift measured in time domain is retentively (!) equal to 30° instead of 90° for an ideal harmonic oscillator. However, high stability and additive feature of this error does not hinder any measurements.

2.9.3.2. Simulation of microcantilever’s amplitude and phase spectra

Simulated amplitude and phase spectra in respect to the variations in damping and the spring constant are shown in Fig. 41.

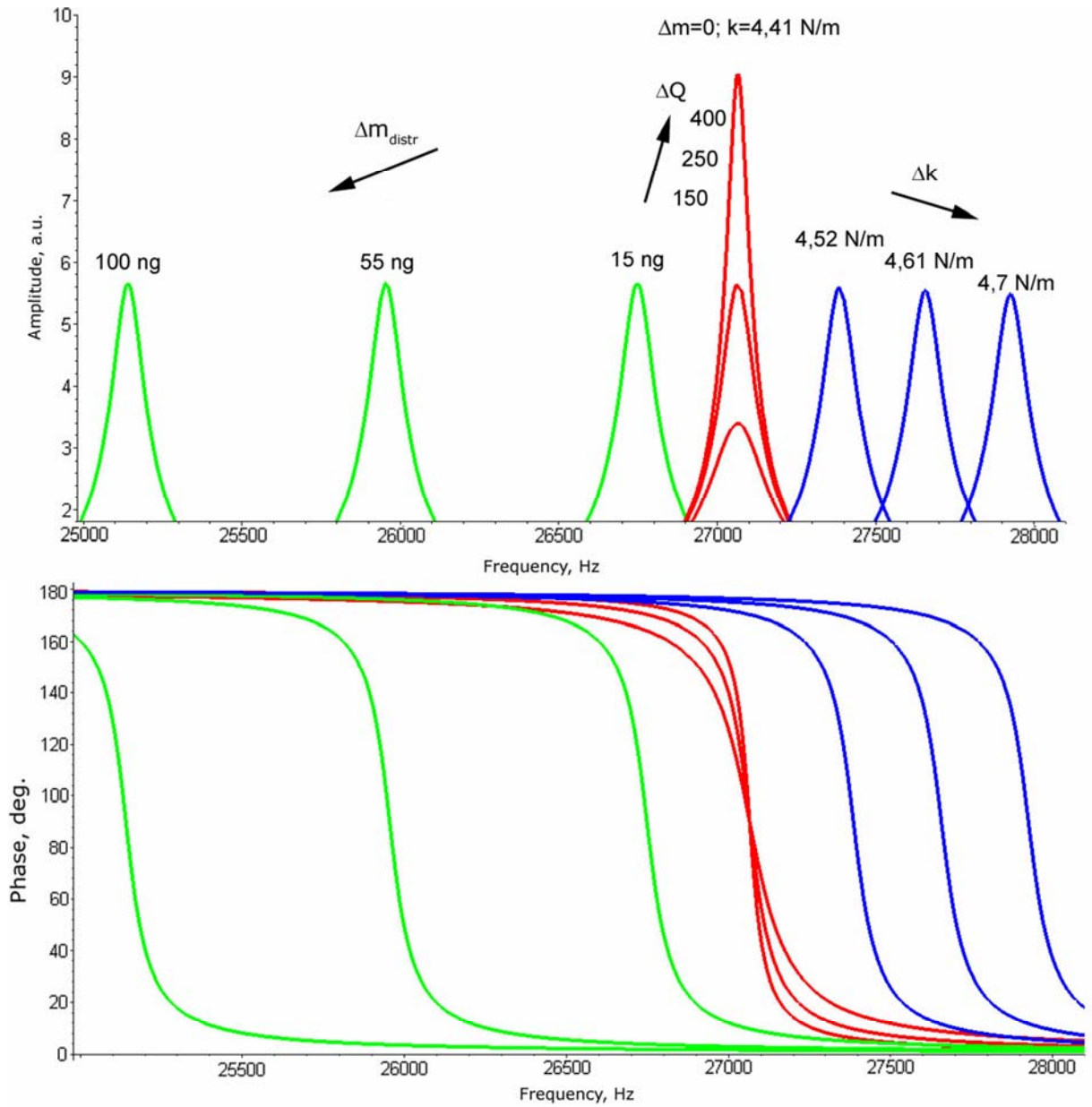


Fig. 41. Simulated amplitude (a) and phase (b) spectra for different damping (ΔQ), distributed mass load (Δm), and spring constant (Δk) variations. The plots were simulated for a rectangular silicon cantilever $450 \times 150 \times 4 \mu\text{m}$ (beam mass is 629 ng) forced to oscillate at the temperature 300 K; quality factors $Q_1=150$, $Q_2=250$, $Q_3=400$; added distributed masses 0, 15, 55, and 100 ng; and the spring constants 4.41, 4.52, 4.61, 4.7 N/m respectively.

These responses can be obtained by considering forced oscillations of a cantilever beam with an outer harmonic force:

$$F_{out} = F_0 \cos \omega t. \quad (78)$$

Let's assume that other forces acting on the cantilever beam are:

- backmoving force, which is proportional to the beam displacement through the spring constant:

$$F_b = -k \cdot z; \quad (79)$$

- resisting force, which is proportional to the speed of the beam movements through the coefficient of resistance (coefficient of viscous friction):

$$F_r = - \gamma dz/dt. \quad (80)$$

Then according to the second Newton's law the governing equation for the beam movement will be:

$$m_{eff} \frac{d^2 z}{dt^2} = F_0 \cos \omega t - kz - \gamma \frac{dz}{dt}. \quad (81)$$

Designating

$$\frac{k}{m_{eff}} = \omega_0^2; \quad (82)$$

$$\frac{\gamma}{m_{eff}} = 2\beta, \quad (83)$$

where β is damping factor (amplitude of damped oscillations is $A(t)=A_0e^{-\beta t}$); and

$$\frac{F_0}{m_{eff}} = F_{eff}, \quad (84)$$

Eq. (81) can be re-written as:

$$\frac{d^2 z}{dt^2} + 2\beta \frac{dz}{dt} + \omega_0^2 z = F_{eff} \cos \omega t. \quad (85)$$

The solution of Eq. (85) for steady-state oscillations can be found as:

$$Z = A \cos (\omega t + \varphi). \quad (86)$$

Finally, the amplitude and phase spectra can be correspondingly derived as:

$$A = \frac{F_{eff}}{\sqrt{(\omega_0^2 - \omega^2)^2 + 4\beta^2 \omega^2}}; \quad (87)$$

$$\varphi = \arctg \left(- \frac{2\omega\beta}{\omega_0^2 - \omega^2} \right). \quad (88)$$

Sometimes it is useful to have Eq. (87) and (88) in terms of coefficient of resistance γ , effective mass m_{eff} and the spring constant k . Using substitutions (82), (83), and (84) we have:

$$A = \frac{F_0}{\sqrt{(k - m_{eff}\omega^2)^2 + \gamma^2\omega^2}}; \quad (89)$$

$$\varphi = \text{arctg}\left(-\frac{\gamma\omega}{k - m_{eff}\omega^2}\right). \quad (90)$$

Let's re-write expressions (87) and (88) in terms of Q-factor. By definition, the quality factor is:

$$Q = \frac{\omega}{2\beta} = \frac{\sqrt{\omega_0^2 - \beta^2}}{2\beta}. \quad (91)$$

It means that in terms of Q-factor:

$$\beta = \frac{\omega_0}{\sqrt{4Q^2 + 1}} \cong \frac{\omega_0}{2Q}; \quad (92)$$

$$\gamma \cong \frac{m_{eff}\omega_0}{Q} = \frac{\sqrt{m_{eff}k}}{Q}. \quad (93)$$

Resonance frequency is lower than natural resonance due to the damping:

$$\omega_{res} = \sqrt{\omega_0^2 - 2\beta^2} \cong \omega_0\sqrt{1 - \frac{1}{2Q^2}}, \quad (94)$$

and

$$A_{res} = \frac{F_0}{2\beta\sqrt{\omega_0^2 - 2\beta^2}}. \quad (95)$$

Eq. (78)-(95) consider two-dimensional cantilever without taking into account its width, which is not applicable for the cantilever, which is moving through a dense medium. Therefore, acoustic damping model must obviously include influence of the cantilever width. The acoustic damping model with experimental results has been presented in §2.8.2. "Experimental results on damping phenomena".

For small damping the Eq.s (87) and (88) can be equivalently re-written as:

$$A \approx \frac{F_{eff}}{\sqrt{(\omega_0^2 - \omega^2)^2 + \left(\frac{\omega_0 \omega}{Q}\right)^2}}; \quad (96)$$

$$\varphi \approx \arctg\left(-\frac{\omega_0 \omega}{Q(\omega_0^2 - \omega^2)}\right), \quad (97)$$

or in terms of the distributed effective mass and the spring constant:

$$A \approx \frac{F_0}{\sqrt{\left(k - m_{eff}(2\pi f)^2\right)^2 + m_{eff}k\left(\frac{2\pi f}{Q}\right)^2}}; \quad (98)$$

$$\varphi \approx \arctg\left(\frac{2\pi f \sqrt{m_{eff}k}}{Q(4\pi^2 f^2 m_{eff} - k)}\right). \quad (99)$$

These expressions were plotted in Fig. 41 (a) and Fig. 41 (b) respectively. From the continuity condition, the phase in Fig. 41, b is scaled to be smooth from 180° to 0°.

In that way, the present paragraph provides with a clear visual demonstration on how the resonance frequency and the phase shift are theoretically dependent on the cantilever stiffness, its effective mass, and its Q-factor. If an increased damping changes the amplitude peak sharpness in obvious manner, and also influences as less steeper slope of the phase curve. Experimental results, which compare amplitude modulation and phase modulation modes, are presented in the next paragraph.

2.9.3.3. Calibration of the phase-shift response

In the frame of this work, we worked in both frequency shift and phase shift modes. However, the phase shift mode appeared more advantageous due to shorter conversion time, much lower noises, much higher sensitivity and resolution. Comparison between frequency shift and phase shift modes is presented in Fig. 42.

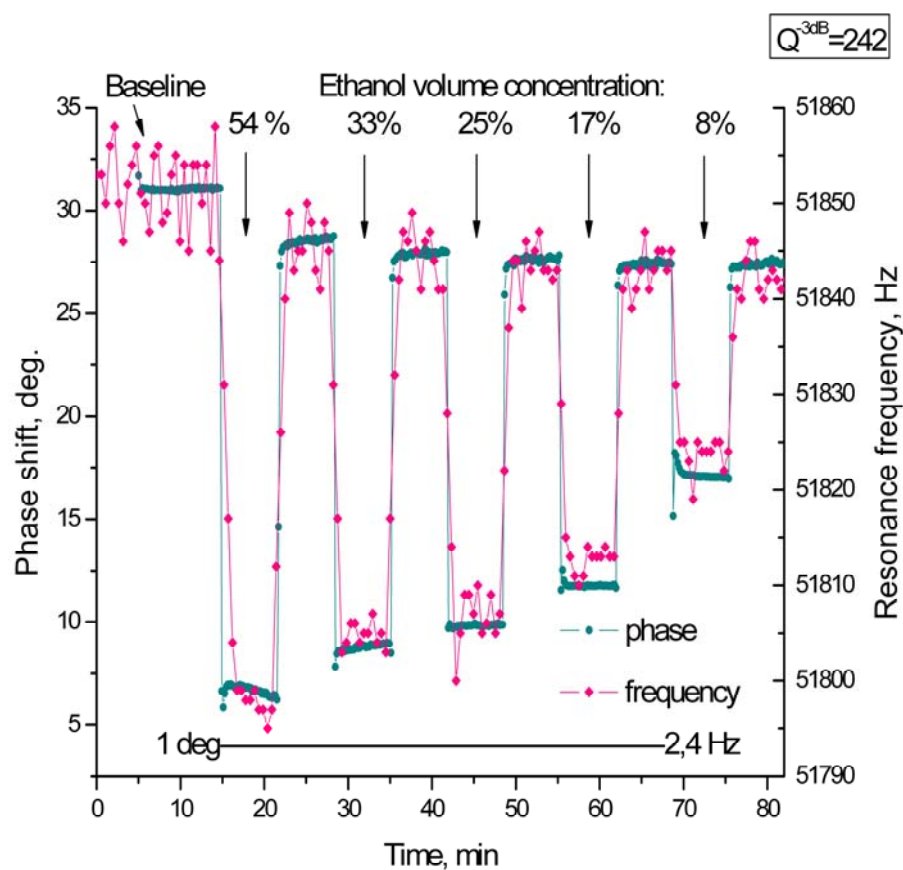


Fig. 42. Resonance frequency and phase shift of calixarene-coated cantilever under varying ethanol concentration.

It is clearly seen that phase shift mode provides more reliable and predictable responses than resonance frequency measurements. This set of experiments allows also quantitative estimation for the mass sensitivity in the phase shift mode. Mass resolution in terms of resonance frequency shift can be estimated by using models discussed above. However, straightforward simulation of the mass sensitivity in the phase shift mode is rather complicated. That is why we deduced “phase sensitivity” by comparison with the “frequency sensitivity”. For a large number of experiments 1 degree of the phase shift on average corresponds to 2.5 Hz of the frequency shift. This important value has been deduced not only by measurements of the same cantilever in 2 modes, but also by comparison 2 different cantilevers (taken from different batch wafers), but with same coatings under same experimental conditions.

In summary, the resonant operation of cantilever transducers encompasses three mechanisms:

- 1) adsorbate-induced mass-loading;
- 2) chemically induced changes in the cantilever stiffness;
- 3) mechanical damping by the viscous medium.

All the mechanisms are reflected in the resonance frequency changes, which in most cases (when the cantilever's spring constant remains unaffected) is an equivalent of the adsorbed mass. Phase shift mode is in its own turn an equivalent of the resonance frequency shift. However it offers several very important uncompromising advantages over the latter method, namely:

- experimentally achieved 25 times better mass resolution and sensitivity threshold;
- no quantisation noises due to the smooth signal acquisition procedure;
- acquisition time applicable for measurement of fast transition processes.

Therefore, most data devoted to the investigation of functionalized cantilevers and their sorption properties, will be presented in the phase shift domain. Experimental set-up for these measurements is described in the next chapter.

Chapter 3.

Experimental set-up

The experimental setup serves for sensors investigation in either gas flow mode or gas single injection mode as well as in vacuum.

Experimental setup consists of 2 independent parts - gas handling system and electrical control and measurement system, which meet one another in the measurement cell.

General view of the experimental set-up is shown in Fig. 43, and its schematic diagram is shown in Fig. 44.

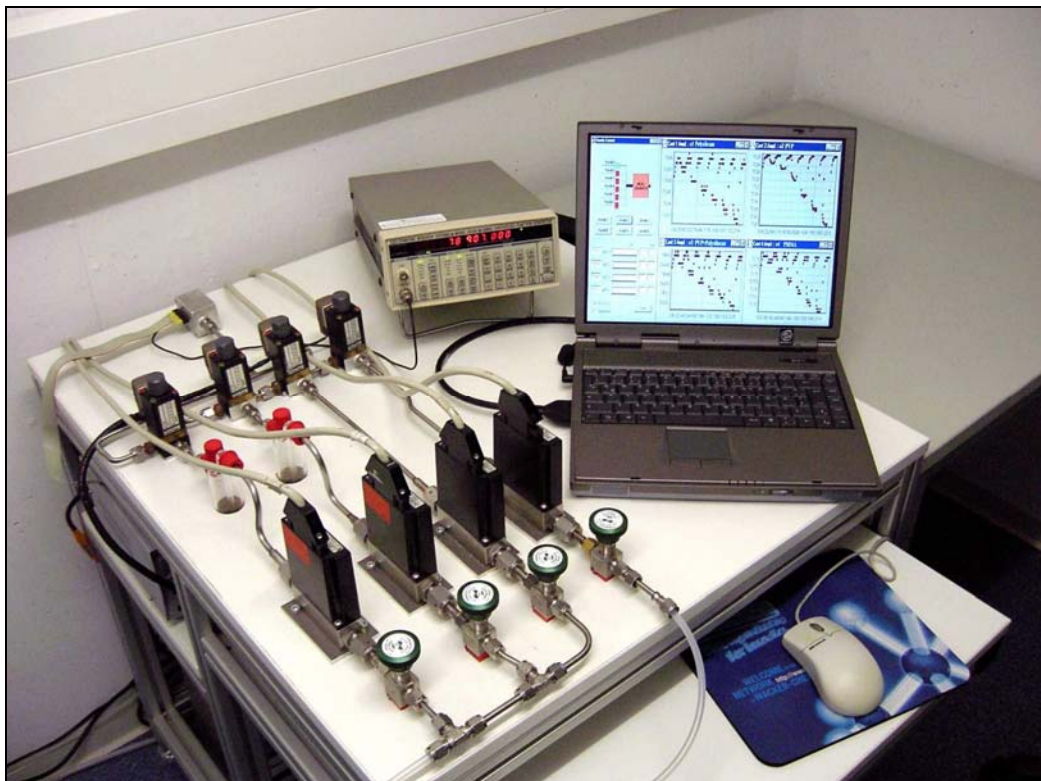


Fig. 43. General view of the experimental set-up.

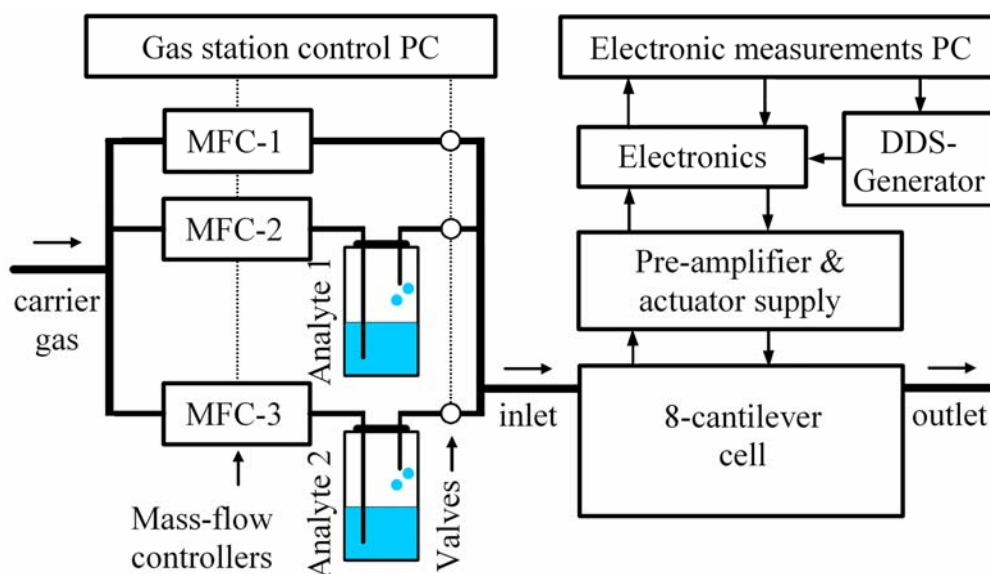


Fig. 44. Schematic diagram of the experimental set-up.

The gas sampling station, which is presented in Fig. 44 by mass-flow controllers (MFCs) and analyte evaporators, is described in § 3.4. The electrical control and measurement system is reviewed in § 3.5. Next three paragraphs consider evolutionary development and correspondingly three generations of the cantilever measurement cell.

3.1. Measurement cell for single cantilever investigations

A versatile gas cell has been designed and manufactured for the automatic measurement set-up (Fig. 45). This unit was initially developed as a versatile measurement cell for investigation of different chemical gas sensors. The cell is a cylinder made of aluminium with length 100 mm, inner diameter 35 mm and outer diameter 60 mm. All the internal filling of the cylinder is reconfigurable depending on the needs.



Fig. 45. A versatile gas flow cell for single cantilever investigations.

The cell has a very flexible design and adjustable volume (Fig. 46). Its cylindrical shape allows sensor arrangement in the area of maximal gas flow turbulence. It enables also easy implementation of helical heater around the cantilever cell (if necessary). The adjustable volume (up to 96 cm³) has been achieved by using of replaceable cork-shaped flanges with different

lengths of the cylindrical filling (Fig. 46), which decreases the initial cantilever cell volume (96 cm^3) to a certain extent. The opposite flange Fig. 47 serves for mounting of the cantilever holder, etc. All the internal sidewalls have been smoothly polished in order to decrease sorption effects on them. The cantilever holder has been mounted on a quartz crystal oscillator. This approach allows microcantilever actuation by means of either quartz oscillations or integrated thermo-actuator. Such the way, the cantilever cell enables relatively easy adaptation for a wide range of measurement tasks and conditions, including operation at different analyte concentrations, partial pressures etc.

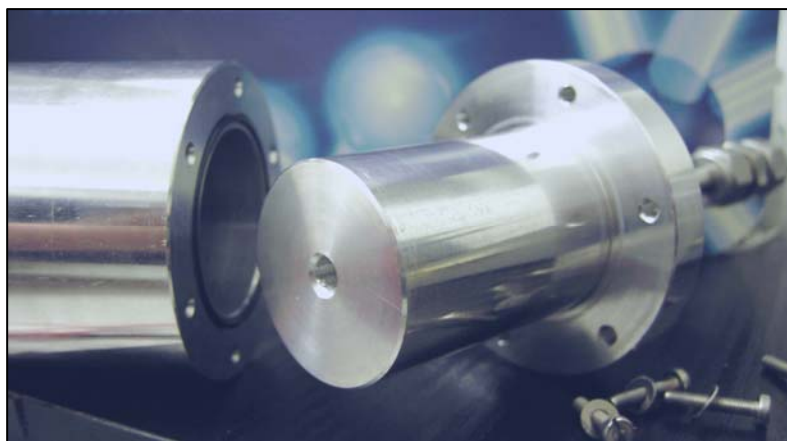


Fig. 46. Replaceable cork-shaped flanges adjust the internal volume.

The described experiments were carried out with a 50 mm long cylinder at the terminated flange, i.e. the cell volume was 48 cm^3 . The opposite flange contains microcantilever holder glued on an oscillating quartz crystal, electrical connectors, and the relative humidity sensor (Rh-sensor), as depicted in Fig. 47.

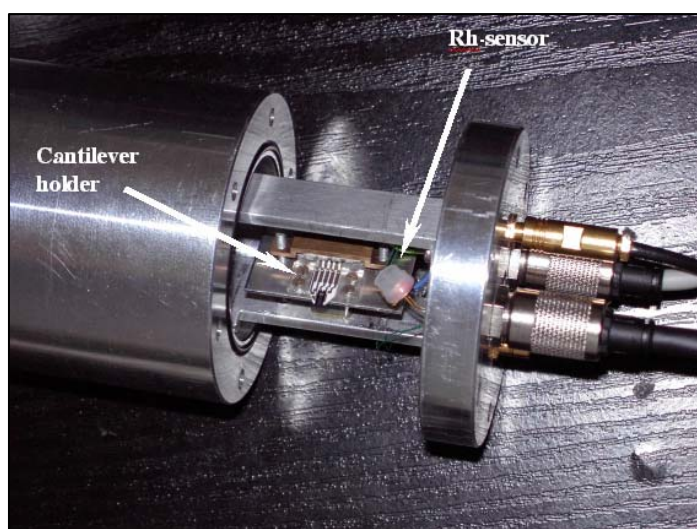


Fig. 47. The opposite flange with cantilever holder, piezoelectric actuator, relative humidity sensor (Rh-sensor), and electrical connectors.

The cell has been equipped with referent relative humidity sensor MiniCap 2 by Panametrics ®. The sensor is based on thin polymer film, which changes its dielectric constant under exposure to water vapours with different concentrations. The resulting sensor capacity changes are proportional to relative humidity variations. The sensor capacity is then converted into voltage and pre-amplified with outer electronic circuitry.

The output signals from the cell are acquired by 12-channel PC card PC20TR by BMC Messsysteme GmbH ®. Software utility (Fig. 48) has been developed, which simplifies relative humidity monitoring in either manual or fully automatic mode. Left program panel shows last measured relative humidity value and the corresponding voltage at the PC20TR input. The graph reflects relative humidity value (in %) versus time (in seconds) passed since the beginning of the measurement (pressing the “Reset” button). When operating in manual mode (“Step by step” option is selected), each pressing onto the “Start” button results in registration of current timer value and the corresponding Rh-value. These data are stored for the subsequent analysis. Pressing the “Start” button in the automatic mode runs subsequent measurement procedure with given time interval (in seconds). Such the way, real-time Rh-monitoring is possible. This mode allows also decreasing sudden humidity fluctuations by averaging Rh-values: each registered Rh-value is arithmetical mean value of a given number of immediate one-by-one measurements.

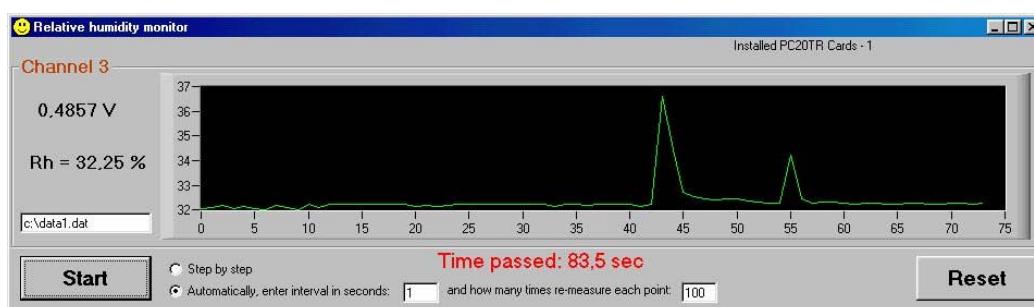


Fig. 48. Relative humidity monitor utility.

The capacitive Rh-sensor has small sizes and linear response. It has been calibrated according to VelociCalc Plus multi-parameter ventilation meter by TSI ®.

3.2. Measurement cell for 4 cantilever array investigations

Four functionalized cantilevers were assembled as a multi-array module on a ceramic (Al_2O_3) chip holder with screen-printed bond pads. The cantilevers were fixed to the holder by epoxy resin and bonded by aluminium wires to the electrical contacts. The cantilever array module was glued onto oscillating quartz crystal and placed into the aluminium cantilever cell (10 cm^3) with analyte inlet and outlet (Fig. 49).

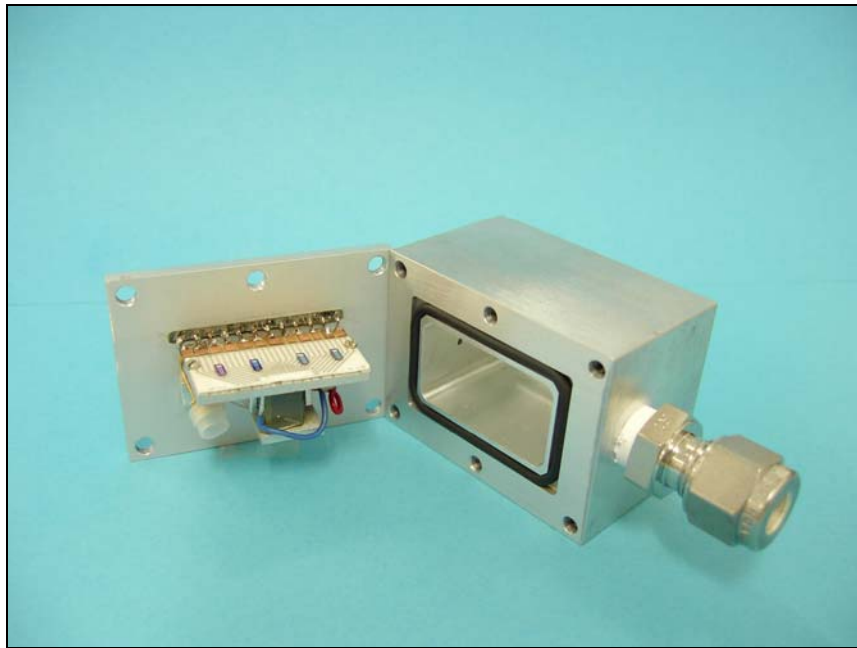


Fig. 49. Cantilever cell for 4 cantilevers.

3.3. Measurement cell for 8 cantilever array investigations

In the next generation of our measurement cell we refused of quartz actuator. Thus, only integrated thermal actuation is possible. Eight cantilevers bonded on double-sided PCBs are placed into Teflon cell, as it is shown in Fig. 50. Teflon, or polytetrafluoroethylene (PTFE), has very low surface energy (non-sticking), is very apolar, is highly chemically resistant, and shows low friction.

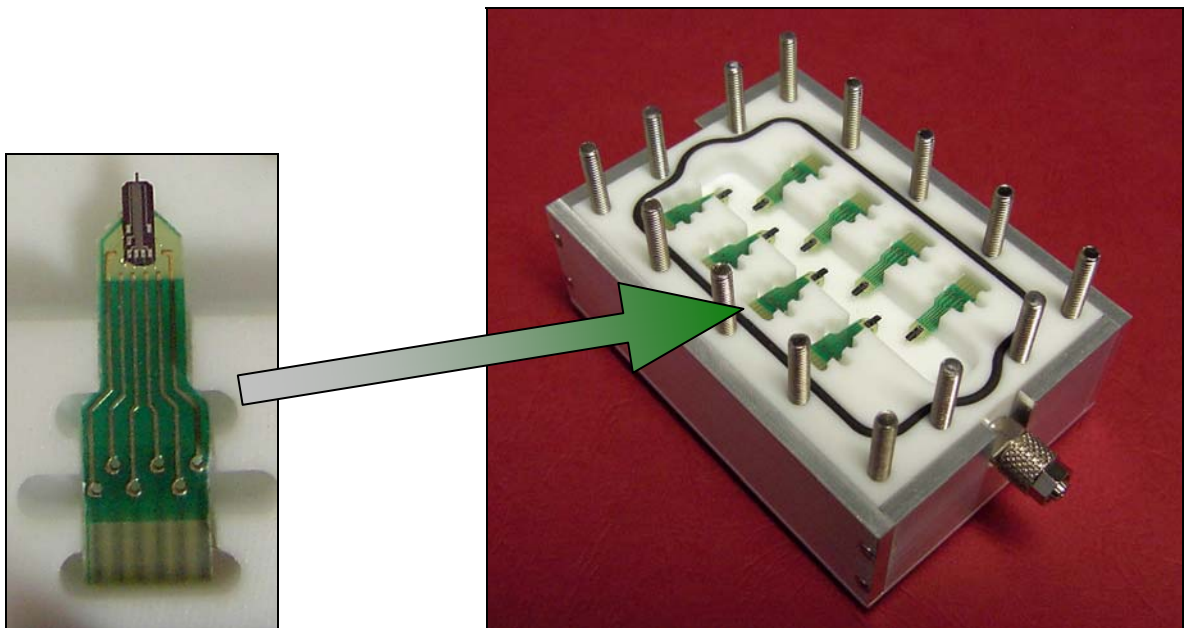


Fig. 50. Advanced Teflon measurement cell applicable for either gas single injection or gas flow mode.

The measured volume of the cell is 6.5 cm^3 . Such low volume in combination with practically non-adsorptive material Teflon[®] makes possible lossless investigation of the sensors not only in gas flow mode, but also in single injection mode with ppm resolution. Rubber O-ring and 14 bolts to the cell's cover enable perfect isolation from the environment. For instance, vacuum with residual pressure 2 Pa was achieved with this cell. The cell is attached to the preamplifier board through DB37 connector. Short interconnections on the specially designed PCB as well as good screening of the connector and the outer aluminium case prevent sensor signals from distortions and noises (Fig. 51).

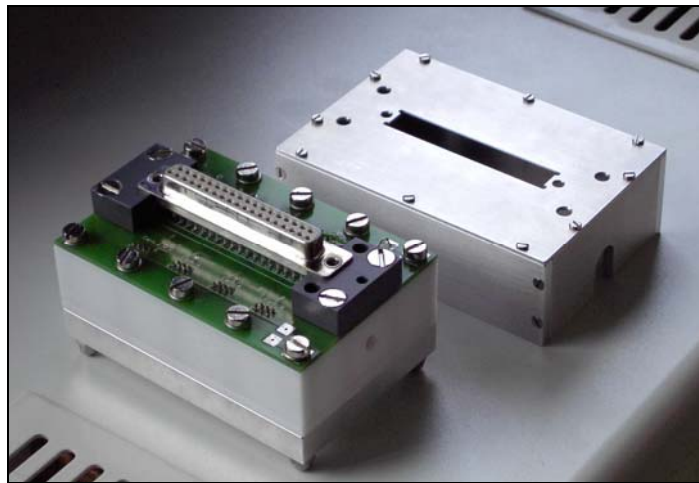


Fig. 51. Electrical part of the measurement cell.

The cantilever holders have reliable contacts to the underlying PCB because of the golden spring contacts to the piezo-resistive Wheatstone bridge and the integrated thermal heater, as it is shown in Fig. 52.

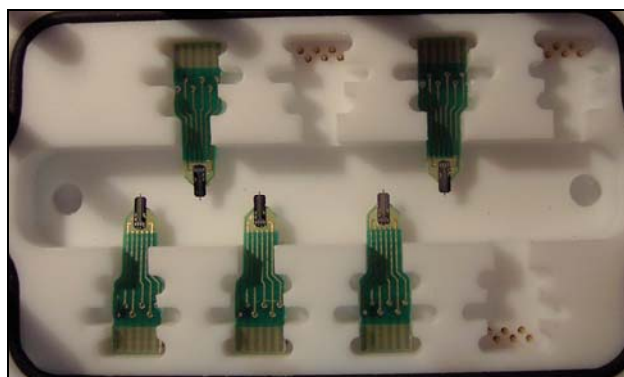


Fig. 52. Golden spring contacts to the cantilever units.

For the single injection experiments we used two Teflon screw corks for the inlet-outlet. One-side cork is a solid terminator, and the other has a through hole with a diameter of 0.9 mm,

which fits perfectly to the corresponding syringe's needle. Saturated vapour of an analyte is diluted in a hermetic Teflon capacity to the needed ppm-range concentration. Then analyte vapour of known concentration is injected into the measurement cell, as shown in Fig. 53.

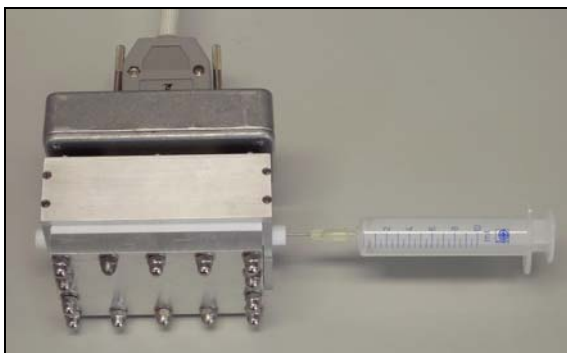


Fig. 53. Single injection of gaseous analyte into the cell.

The cell is also operable in gas flow mode in conjunction with our gas station (Fig. 54).



Fig. 54. The cantilever cell operating in gas flow mode.

3.4. Gas sampling station

The gas handling system is used for programmed exposure of functionalized cantilevers to various gaseous analytes in gas flow mode.

By using of three software-driven mass-flow controllers Tylan FM-260 (further referred to as MFCs) in the gas handling system we are able to mix dry nitrogen as a carrier gas of an analyte with additional nitrogen flow as a dilutant in order to achieve the desired concentrations of the individual analytes or their binary mixtures. Two ml of each liquid analyte (e.g., water, methanol or 2-propanol) are filled into separate bubblers (evaporators), and the carrier gas

extracts and transfers the analyte vapours to the gas mixer and then to the inlet of the measurement cell.

Each MFC channel is additionally equipped with electromagnetic valve for reliable shutting of the not used channels off.

To investigate the influence of the individual analyte concentrations on the cantilever responses, we vary the analyte gas flows from 140 ml/min to 25 ml/min in five steps. The total gas flow rate (analyte vapours flow and dilution nitrogen flow) through the cantilever cell per exposure is kept constant at 150 ml/min during all experiments. This means, for example, that for the measurements with “93% analyte”, 140 ml/min dry nitrogen saturated with analyte vapours was mixed with 10 ml/min of dry nitrogen, coming through the bypass. Most of the conducted experiments can be illustrated by the following technique. Analyte volume concentration in the cantilever cell (a portion of the analyte in total gas flow) was being injected for each analyte according to the operation diagram, which is shown in Fig. 55.

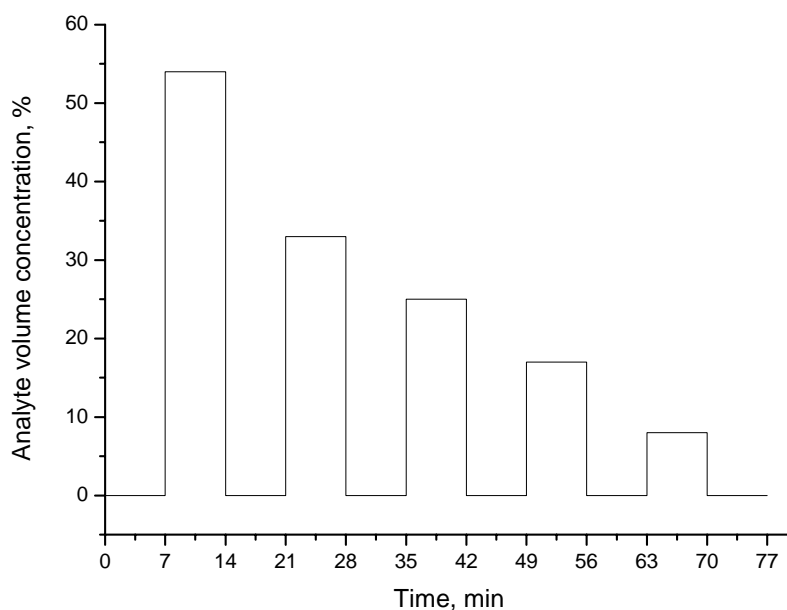


Fig. 55. Typical operation diagram for the MFC.

Such the way, purging the measurement cell with carrier gas (N_2) is interlaced with analyte injections with decreasing volume concentrations.

By exposure to binary mixtures, the total gas flow is achieved by simultaneous passing of the controlled carrier gas flow through the separate evaporators with the individual analytes and then mixing the analyte flows with a controlled flow of nitrogen. The sensors were tested with four binary mixtures for each combination of analytes using analyte gas flows between 5 ml/min and 50 ml/min.

The software for driving the MFCs included two program steps for each analyte concentration. The first step was purging of the analyte cantilever cell with dry nitrogen for 300 s to establish the steady baseline resonance frequency of the cantilevers. During the second step, the analyte vapours were introduced into the cantilever cell for the same time (300 s) to expose the functionalized cantilevers.

3.5. Measurement electronics and acquisition software

This part of the measurement set-up has been developed in collaboration with Microsystems Ltd. (Varna, Bulgaria) for the following purposes:

- control of the cantilever sensor operation at different modes;
- signal measurement and processing;
- programming the experiment, control of the experimental environment;
- data transfer, data store and post-processing.

Both external and integrated actuation is supported. The resonance frequency shift of the functionalized cantilevers for most experiments was estimated with an accuracy of ± 1 Hz (system design enables 0.01 Hz accuracy).

The general view of the acquisition hardware is shown in Fig. 56.

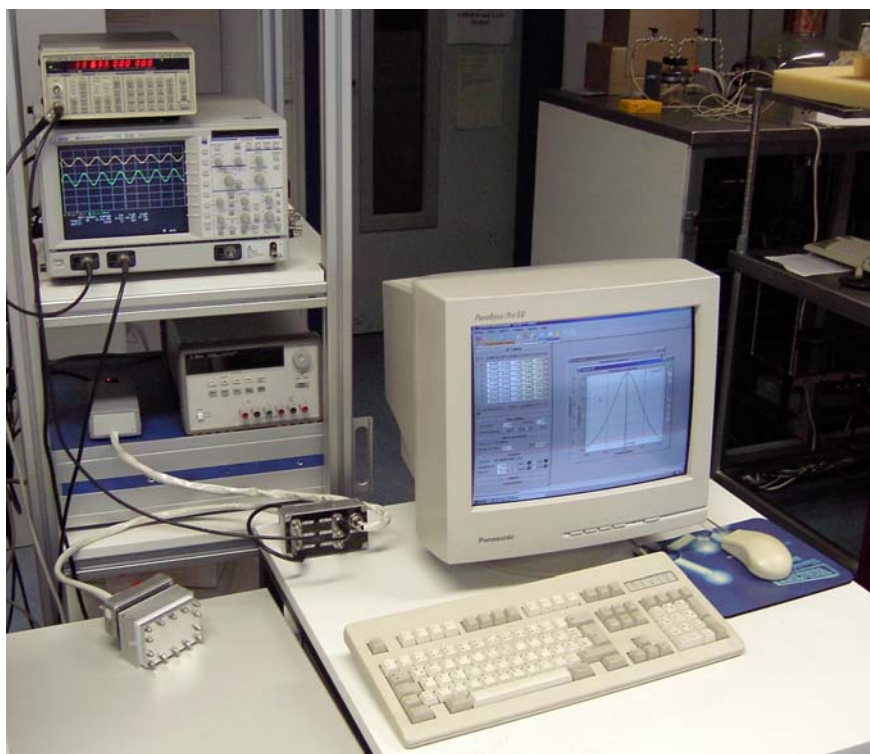


Fig. 56. General view of the acquisition hardware.

The hardware consists of the following building blocks:

- preamplifier block, which is attached directly to the Teflon measurement cell through the DB37 connector (see Fig. 57);



Fig. 57. Pre-amplifier attached to the cantilever cell.

- control electronics and signal processing module, which is shown in Fig. 58;



Fig. 58. Control electronics and signal processing module.

- PC-based data acquisition card PC20TR by BMC Messsysteme GmbH (12-bit multifunction card with 16 analog inputs and 100 kHz sampling rate);
- functional generator from Stanford Research System (Model DS345).

The block diagram of the developed electronics is shown in Fig. 59.

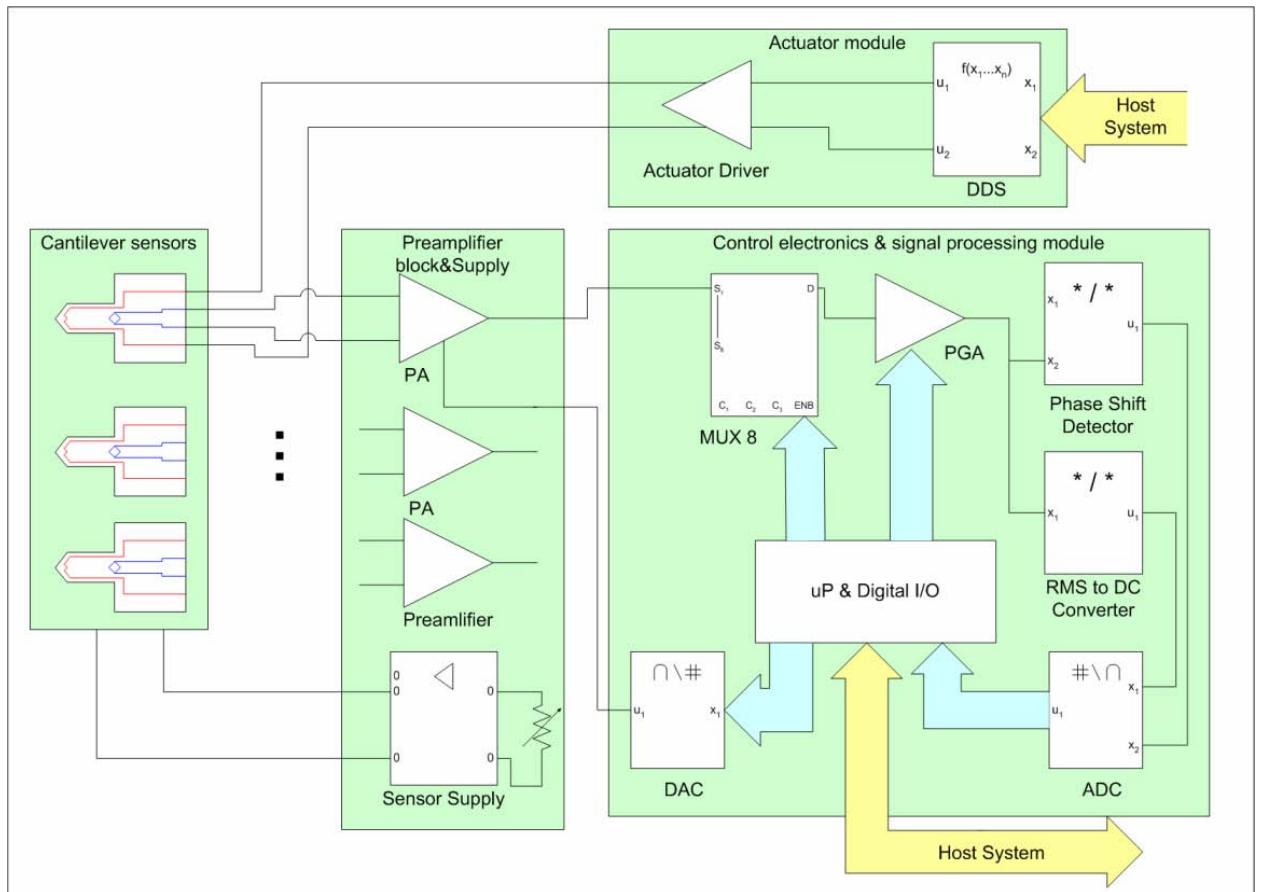


Fig. 59. Block diagram of the acquisition and control electronics.

The following basic building blocks of the acquisition and control electronics have been developed:

- Input stage electronics for 8 single piezo-resistive cantilevers. This module comprises very low noise selective preamplifiers (input noise below $10 \text{ nV/Hz}^{1/2}$), programmable gain amplifiers, and high-stability sensor supply.
- Actuator module for single cantilever and array cantilevers thermo-actuation. Very high accuracy (0.01 Hz) and frequency stability (0.001 Hz) of the sensor vibration have been achieved using Direct Digital Synthesis (DDS).
- Automatic offset compensation circuitry.
- Phase sensitive detectors and signal rectifiers for resonance frequency detection and tracking. Flexible, application-specific plug-in modules have been designed.
- Precise ADC (up to 24-bit resolution) and DAC (up to 16-bit resolution) modules.
- “On board” and host system control software.

The compact, module-architecture data acquisition system enables thorough characterization of the cantilever sensors. The input electronic stages and dedicated plug-in

modules provide the sensor operation control, signal measurement and pre-processing. The data is transferred to the host system for post-processing and storage.

Such a way, the modular architecture of the measurement system consists of the following blocks:

- Preamplifier module:
 - 8-channel amplifier (low noise, DC stable, fixed gain 39 (50), BW ~500 KHz)
 - Temperature stabilized sensor bridge supply
- Main module:
 - Actuator driver (high-output current voltage source)
 - 8 + 2 channel MUX
 - Programmable Gain Amplifier (4 programmable gains)
 - 2 universal slots for replaceable plug-in modules (RMS-to-DC converter etc)
- External DDS generator
- External ADC/DAC PC card
- PC software for resonance frequency measurements

The software task-dependent interfaces are shown in Fig. 60 and Fig. 61.

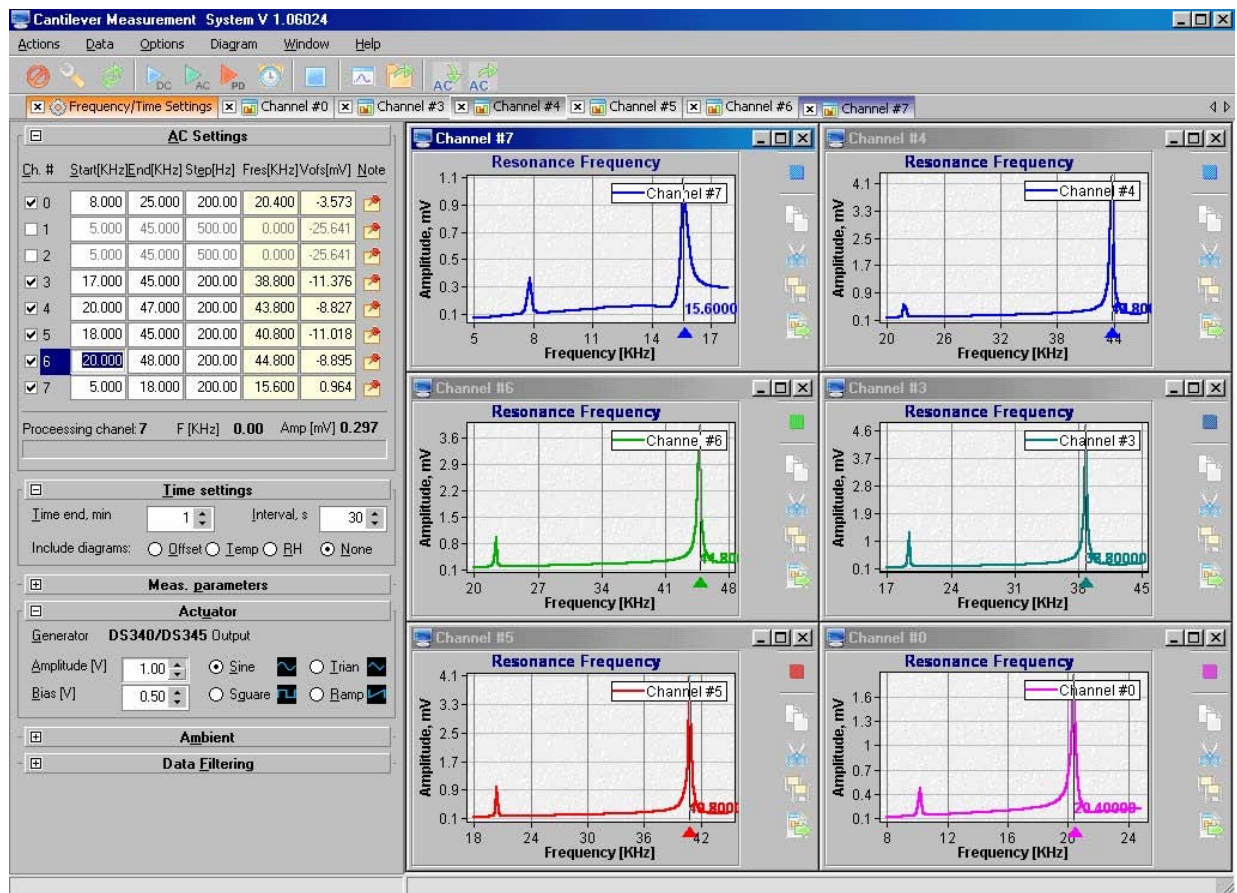


Fig. 60. Screen-shot of the software working panel with 6 cantilevers scanned over a frequency range.

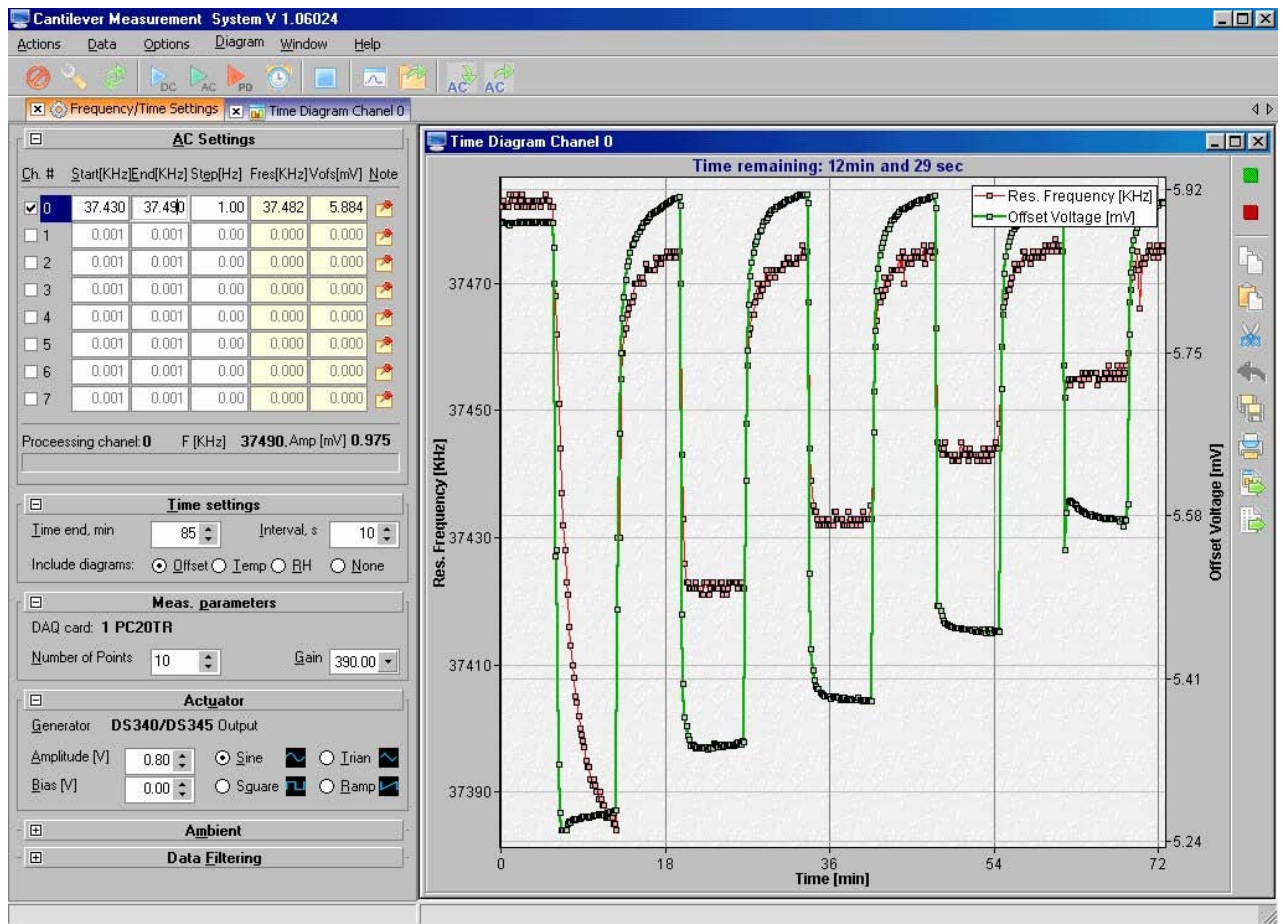


Fig. 61. Screen-shot of simultaneous measurements of resonance frequency and the offset voltage within a cantilever.

Fig. 60 illustrates first resonance mode of 8 cantilevers found in the specified frequency range with the specified Gain accuracy (frequency step). The AC and DC component of the actuator signal is also set up through the program interface.

Fig. 61 illustrates single cantilever operation in time domain under environmental variations. Both resonance frequency and offset voltage are monitored. This enables simultaneous measurements of the cantilever in static bending and resonance modes. The interval between the neighbouring points is controlled as well as the number of consequent measurements (“Number of Points”) for each graphically represented point. Several tens of such consequent measurements are then averaged in order to decrease random fluctuations. For noisy signals “Data filtering” may be involved either during the measurement or as a post-processing algorithm.

Implementation of these complex solutions made it possible to carry out a wide range of experiments described in next chapters.

Chapter 4.

Sorption-induced effects and their influence on the cantilever operation

Cantilever application as a (bio-)chemical sensor is naturally based on the cantilever interaction with its environment. The interaction includes thermal effects, viscous damping, and a range of sorption-induced effects, such as mass-loading, modulation of mechanical stresses, and changes in elasticity of the cantilever. These sorption-induced effects, which are considered in the present chapter, play principal role in nanomechanical gas sensing and recognition.

Adsorption-induced modulation of mechanical properties of thin (~1 mm) plates has been considered and described elsewhere [108]. These classical models have been revisited since the application of MEMS and NEMS.

One of the first gas sensor applications of commercial V-shaped silicon nitride microcantilevers has been historically reported for detection of mercury vapour in [59]. Microcantilevers used therein were functionalized with gold and tested in both static deflection and dynamic resonant modes of operation. Due to the wettability effect of Au towards Hg, spring constant of the layered cantilever structure became significantly affected, which led to higher resonance frequency of the cantilever under exposure to $30 \mu\text{g}/\text{m}^3$ of mercury vapour added to nitrogen carrier gas. This interesting “inverse” phenomenon demonstrates the importance of deep consideration of interaction effects between the functionalized cantilever surface and the analyte, which is to certain extent covered in the present chapter. Later experiments confirmed that if the clamping region of a cantilever (which primarily defines the cantilever stiffness) remains without gold, mercury vapour did lower the resonance frequency. Then the added mercury mass can be calculated according to rather straightforward model given by Eq. (40).

Despite of very inert chemical properties of gold, gold-coated cantilevers not only provide a platform for dosimetric (or cumulative) mercury vapour sensing, but also they can be employed for sensing mercaptans (or thiols), i.e. chemical compounds with one or several –SH groups. For instance, another described example of gold-coated cantilever application includes

detection of 2-mercaptoethanol vapour at concentrations down to 50 ppb in static deflection mode [109].

Another example of selective interaction between metal-coated cantilever and gaseous analyte can be demonstrated due to high solubility of H in Pd and Pd-based alloys. Real-time (reversible) hydrogen sensing with palladium-coated cantilevers has been achieved in [65]. Alpha platinum oxide has been utilised for dosimetric hydrogen sensing in [110].

The present chapter introduces sorption models and also gives specific examples of the sorption-induced effects on the cantilevers with inorganic coatings.

4.1. Overview of sorption models

All solid substances (*adsorbents*) are capable to attract molecules of gases (*adsorbates*) to their surfaces. Solid surface of a cantilever transducer is typically modified (*functionalized*) in order to control (usually increase) affinity to the targeted analyte. Interaction of gases and vapours with solids may be either a surface effect (*adsorption*, Fig. 62, a) or bulk effect (*absorption* Fig. 62, b), which depends on the particular material and the volatile analyte. *Adsorption* refers to the collecting of molecules by either external surface or internal surface (walls of capillaries or crevices) of solids (Fig. 62, a and c). *Absorption*, with which it is often confused, refers to processes in which a substance penetrates into the actual interior of crystals, of blocks of amorphous solids, or of liquids. The word *sorption* is used to indicate the process of the taking up of a gas or liquid by a solid without specifying whether the process is adsorption or absorption.

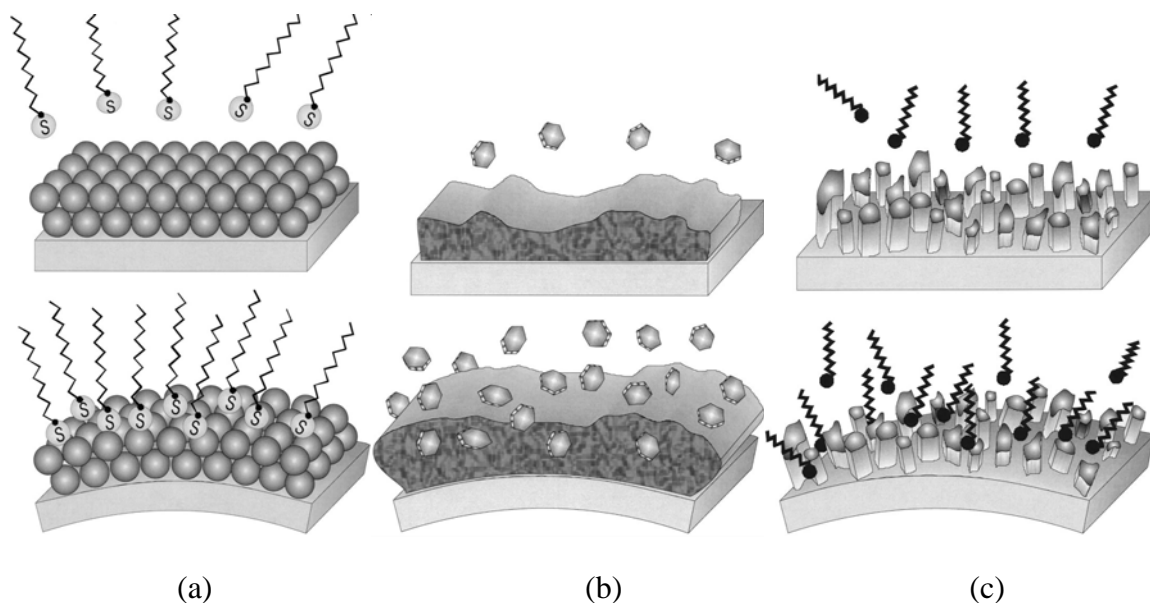


Fig. 62. Three sorption models [9]: (a) Adsorption onto a thin solid surface; (b) Absorption by a thicker analyte-permeable coating; (c) Mixed-mode sorption by a nanostructured coating.

Adsorption can be either physical or chemical in nature. *Physical adsorption* resembles the condensation of gases to liquids and depends on the physical, or van der Waals, force of attraction between the solid adsorbent and the adsorbate molecules. There is no chemical specificity in physical adsorption, any gas tending to be adsorbed on any solid if the temperature is sufficiently low or the pressure of the gas sufficiently high. In the case of *chemical adsorption*, gases are held to a solid surface by chemical forces that are specific for each surface and each gas. Chemical adsorption occurs usually at higher temperatures than those at which physical adsorption occurs; furthermore, chemical adsorption is ordinarily a slower process than physical adsorption and, like most chemical reactions, frequently involves an energy of activation E_a , as it is shown in Fig. 63.

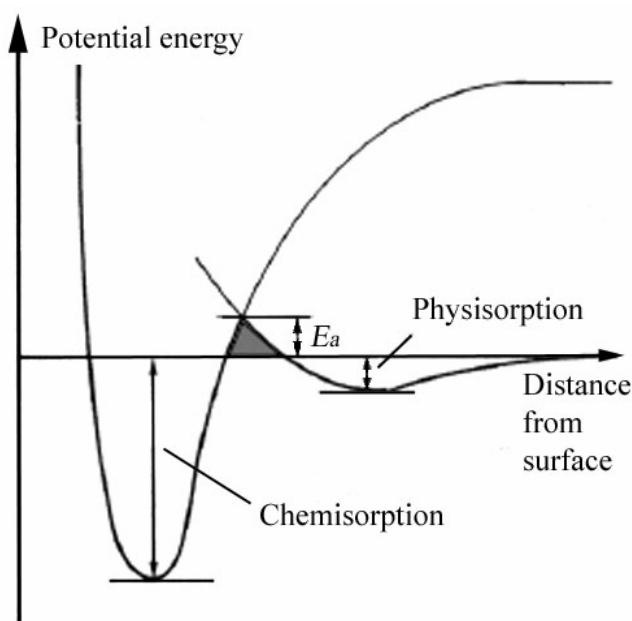


Fig. 63. Adsorption energy diagram.

Cantilevers intended for use in the static bending mode are typically modified so that one of the sides is relatively passive while the other side exhibits high affinity to the targeted analyte. The surface stress occurring during the adsorption process results in a static bending of the cantilever. Practically, differential surface stresses of several 10^{-3} N/m result in deflections of about 10 nm [12].

In dynamic mode, the cantilever may be coated on its upper and lower surfaces with a molecular layer sensitized to recognize molecules from the environment. For the cantilever geometry described in [111] (500 μm length, 100 μm width, and 8.6 μm thickness) 1 Hz frequency shift roughly corresponds to 1 pg of the added mass [12].

In order to understand how different modifying coatings provide responses of cantilever sensors, it is useful to consider the three distinctive models, which were shown in Fig. 62.

4.1.1. The first sorption model

is most adequate when interactions between the cantilever and its environment are predominantly surface phenomena. For instance, chemisorption of straight-chain thiol molecules on a gold coated cantilever (Fig. 62, a). Adsorption of analyte species on transducer surfaces may involve physisorption (weak bonding, binding energy < 0.1 eV) or chemisorption (stronger bonding, binding energy > 0.3 eV).

Physisorption is associated with van der Waals interactions between the adsorbate and the adsorbent substrate. As the analyte species approach the surface, they can polarize the surface creating induced dipoles. The resulting interactions are associated with binding energies less than 0.1 eV. Much higher binding energies are characteristic of chemical bonding between the analyte and the surface in the case of chemisorption.

Under physical adsorption, adsorbate molecules retain their individuality. Adsorption forces are similar to the Van Der Waals bondings in real gases. Under chemical adsorption, the molecules combine chemically with the surface atoms. Exchange coupling, ionic or coordination bond may occur.

Adsorption of a gas to a solid is a result of the net forces that exist between the gas and solid. These forces include repulsive forces (short term) as well as attractive forces (called coulombic forces). The repulsive forces are short term because of the nature of the electron clouds that exist around each molecule. When the degree of coverage is low, then the force between the adsorbent and adsorbate is important (low traffic), whereas once the surface begins to 'fill up' the adsorbate molecules begin to repel against each other. Chemisorption involves chemical bonding, hence can only exist in one layer. Physisorption can exist on many layers although the forces involved are much weaker. The same sort of chemical bonding cannot exist between the adsorptive and the adsorbate.

In general, changes in surface stresses can be largely attributed to changes in Gibbs free energy associated with adsorption processes. An example of this situation is given in Fig. 62 (a), where chemisorption of straight-chain thiol molecules on a gold-coated cantilever is schematically depicted. Since spontaneous adsorption processes are driven by an excess of the interfacial free energy, they are typically accompanied by the reduction of the interfacial stress. In other words, surfaces usually tend to expand (see Fig. 62) as a result of adsorptive processes. This type of surface stress change is defined as compressive, referring to a possibility of return of the surface into the original compressed state. The larger the initial surface free energy of the substrate, the greater the possible change in surface stress results from spontaneous adsorption processes. Compressive surface stresses were experimentally observed on the gold side of gold coated cantilevers exposed to vapour-phase alkanethiols.

When adsorbate-induced stresses are generated on ideal smooth surfaces or within coatings that are very thin in comparison to the cantilever, the predictions for the cantilever bending can be based on the expected surface stress change according to Eq. (8). Alternatively, responses of cantilever sensors converted into surface stress changes can be analysed as the measure of the coating efficiency independently of the transducer geometry.

4.1.2. The second sorption model

of analyte-induced stresses and cantilever deformation is applicable for a cantilever modified with a much thicker than a monolayer analyte-permeable coating, which is schematically depicted in Fig. 62 (b).

Taking into account interactions of the analyte molecules with the bulk of the responsive phase, a predominant mechanism of cantilever deflection can be described as deformation due to analyte-induced swelling of the coating (Fig. 62, b). Such swelling processes can be quantified using approaches developed in colloidal and polymer science, i.e., by evaluating molecular forces acting in the coating and between the coating and the analyte species. In general, dispersion, electrostatic, steric, osmotic, and solvation forces, acting within the coating can be altered by absorbed analytes. Depending on whether it is more appropriate to describe the responsive phase as solid or gel-like, these altered forces can be put into accordance with, respectively, stress or pressure changes inside the coating. An in-plane component of this change multiplied by the coating thickness yields an apparent surface stress change that can be used in Stoney's model, which is represented by Eq. (8), in order to estimate deflections of a cantilever coated with thin, soft, responsive films. It is important to note that the magnitude of apparent surface stress scales up in proportion with the thickness of the responsive phase.

4.1.3. The third sorption model

reflects analyte-induced cantilever deformation in the case of a structured modifying phase (Fig. 62, c). It is most relevant to nanostructured interfaces and coatings, such as porous surfaces, nanozeolites, surface-immobilized colloids and calixarenes, which have been recently recognized as a very promising class of responsive phases for chemical sensors. It is worthy to note that grain boundaries, voids, and impurities have been long known as being responsible for high intrinsic stresses in disordered, amorphous, and polycrystalline films.

Analyte-induced deflections of cantilevers with structured phases combine mechanisms of bulk, surface, and intersurface interactions. A combination of these mechanisms facilitates efficient conversion of the energy of receptor-analyte interactions into mechanical energy of cantilever bending. Our studies demonstrated that up to two orders of magnitude increases in cantilever responses can be obtained when receptor molecules are immobilized on

nanostructured instead of smooth gold surfaces. Furthermore, nanostructured responsive phases offer an approach to substantially increase the number of binding sites per cantilever without compromising their accessibility for the analyte. In fact, many of these nanostructured phases exhibit behaviours of molecular sponges. Although deflections of cantilevers with nanostructured coatings or thicker hydrogel layers cannot be accurately predicted using the analytical models mentioned above, estimates for the upper limit of the mechanical energy produced by any cantilever transducer can always be based on simple energy conservation. This upper limit in available energy is given by the product of the energy associated with the binding site-analyte interaction and the number of such interactions on the cantilever surface.

Uncoated cantilevers also exhibit responses to analytes. This happens due to analyte adsorption onto native silicon oxide and pore condensation. Moreover, uncoated cantilevers are used as referent sensors for differentiating environmental fluctuations and improving the signal pattern. That is why our investigations encompass both theoretical and experimental aspects of silicon oxide sorption properties.

4.2. Adsorption onto cantilevers coated with silicon oxide films

All crystalline and amorphous modifications of SiO₂ (except stishovite) are based on the silicon-oxygen tetrahedrons SiO₄ [112]. Tetrahedron SiO₄ structures are stable if only the neighbouring tetrahedrons have common vertexes. SiO₄ structures with common edges or with common planes are very unstable due to increased repulsion forces between Si atoms. If such overstrained siloxane bridges contact water, partial restoration of the hydroxyl mantle takes place, as illustrated in Fig. 64.

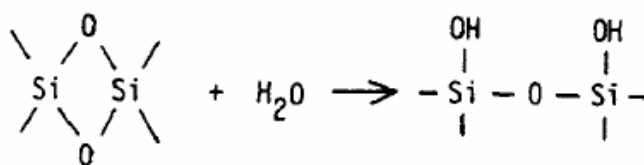


Fig. 64. Unstable SiO₄ structures in contact with water molecules [112]

All free oxide surfaces, which are in contact with atmosphere, are always hydrated, i.e., they contain water molecules and hydroxyl groups as well. Large amounts of these groups can be identified with IR- and NMR-spectroscopy. Hydroxyl mantle of SiO₂ surface is extremely non-homogeneous. According to IR- and NMR-spectra, it consists of 3 different types of OH-groups, as it is shown in Fig. 65.

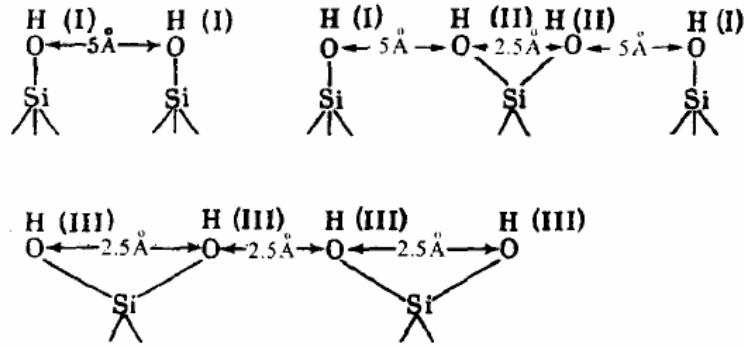


Fig. 65. Typical hydroxyl groups on the SiO_2 surface [112].

There are two types of adsorbed water molecules:

- 1) H_2O molecules that are combined with the surface by weak hydrogen bonds, which can be fully destroyed by thermal vacuum treatment at $T = 350\dots450$ K.
- 2) H_2O molecules that are combined with silicon atoms by strong coordination bonds. These molecules can be removed in vacuum at $T = 500\dots600$ K.

During adsorption process, water film on the SiO_2 surface grows as a cluster structure. Cluster formation centres are H_2O molecules. Lateral cluster extension is attributed to the OH-surface groups. Then coalition of these clusters occurs, and polymolecular film appears. Further adsorption takes place due to increasing of water film thickness. Such the way, water adsorption model on hydrated SiO_2 surface according to BET (Brunauer-Emmet-Teller) theory of adsorption can be represented by Volmer-Weber growth model, as illustrated in Fig. 66.

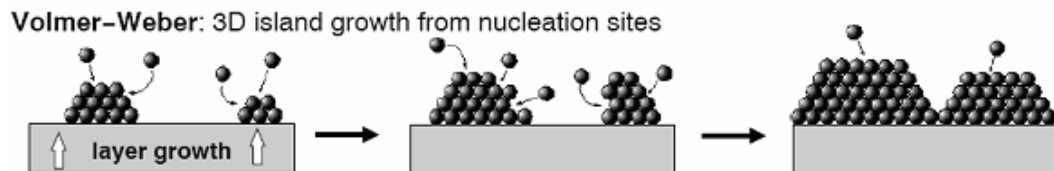


Fig. 66. Water adsorption model on hydrated SiO_2 surface according to Volmer-Weber growth model.

Experimental results below present the data, which was directly obtained from the cantilever coated with native oxide, which is 15...20 nm thick. The cantilever was actuated by quartz crystal (0.3 V oscillation amplitude), and the output voltage was averaged by 100 points. Relative humidity were measured with referent capacitive Rh-sensor MiniCap 2 by Panametrics.

The resonance frequencies versus relative humidity at different temperatures are shown in Fig. 67. At room temperature frequency shift of 13 Hz is observed for increasing relative humidity from 5 to 80% (Fig. 67, a). As can be concluded from Fig. 67 (b), temperature increase leads to the lowering of sensitivity of the cantilevers. This can be explained as temperature increase makes desorption rate higher, which leads to the fluctuations observed in Fig. 67 (b). Higher temperature makes the cantilever practically insensitive Fig. 67 (c).

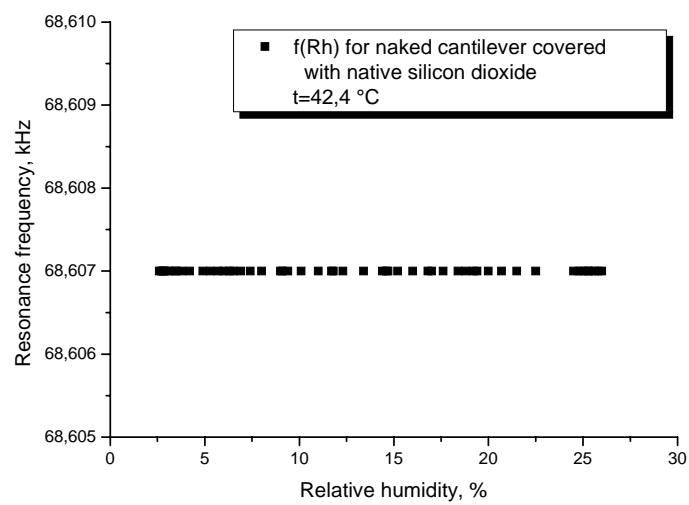
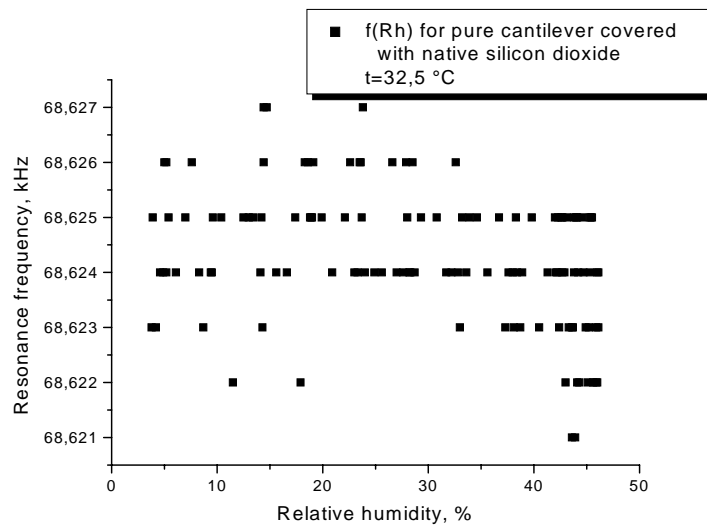
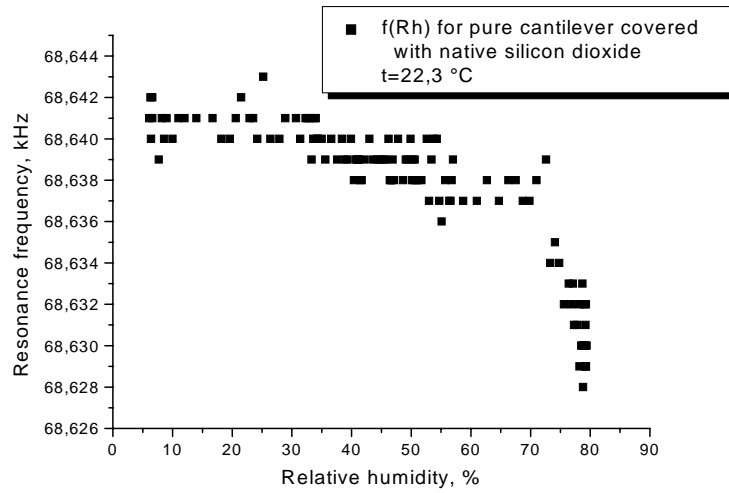


Fig. 67. Resonance frequency vs relative humidity for uncoated cantilever at three different temperatures: 22.3 °C (a); 32.5 °C (b); 42.4 °C (c).

Dispersion of 2...4 Hz is usual for all our measurements, thus approximated characteristics for the resonance frequencies is adduced in Fig. 68, which summarizes the raw data as isotherms (polynomial approximation was used). It can be concluded that cantilevers have the highest dynamic range at lower temperatures.

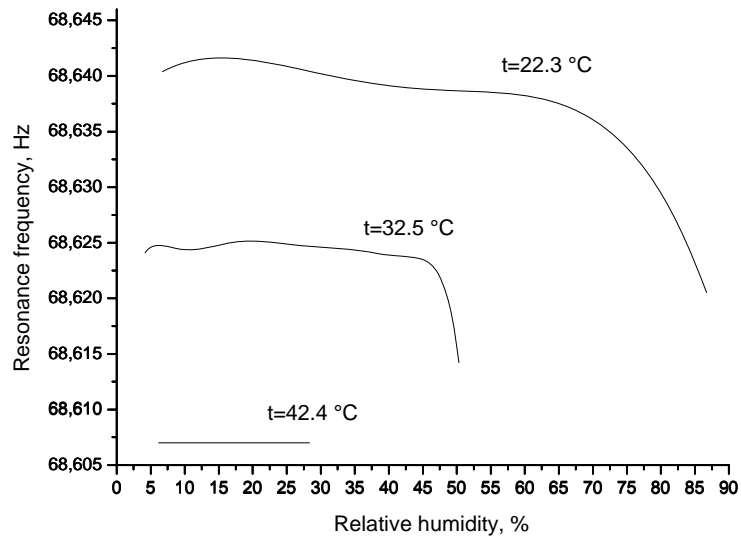


Fig. 68. Resonance frequency vs relative humidity for uncoated (native oxide coated) cantilever at different temperatures.

Temperature dependence of the resonance frequency is shown in Fig. 69. Thus, uncoated cantilever is more sensitive to the temperature changes than to the water vapour concentration.

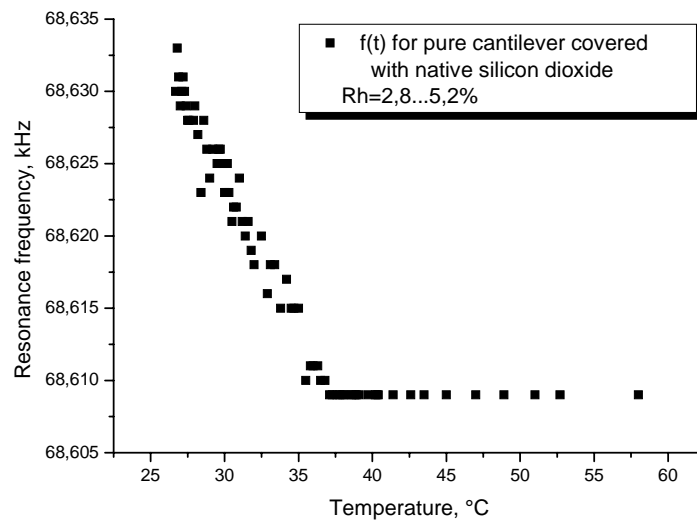


Fig. 69. Resonance frequency vs temperature for uncoated cantilever.

Such the way, native oxide surface can unspecifically physisorb water vapours due to weak Van-der-Waals forces and condensation onto the surface. Naturally, the condensation is more effective at lower temperatures, as it has been confirmed by our experiments. Actually, the resonance frequency remains the same at temperatures elevated over 37 °C. It can be explained by the equilibrium of the adsorption-desorption rate at higher temperatures such a way that no water condensation is possible.

Obviously, thicker silicon oxide with higher porosity should provide greater responses. Measurements with a cantilever covered with thermally grown oxide prove this assumption. 25 Hz frequency shift was observed with such a cantilever versus relative humidity changes from 5 to 80% (Fig. 70). Thicker 600...800 nm oxide was the not-etched mask for boron diffusion obtained at 850...900 °C in the mixture of nitrogen and oxygen flow. Amplitude at the quartz actuator was 2 V; the results were averaged by 100 independent consequent measurements. Q-factor modulation for the cantilever coated with thick oxide is also presented in Fig. 70.

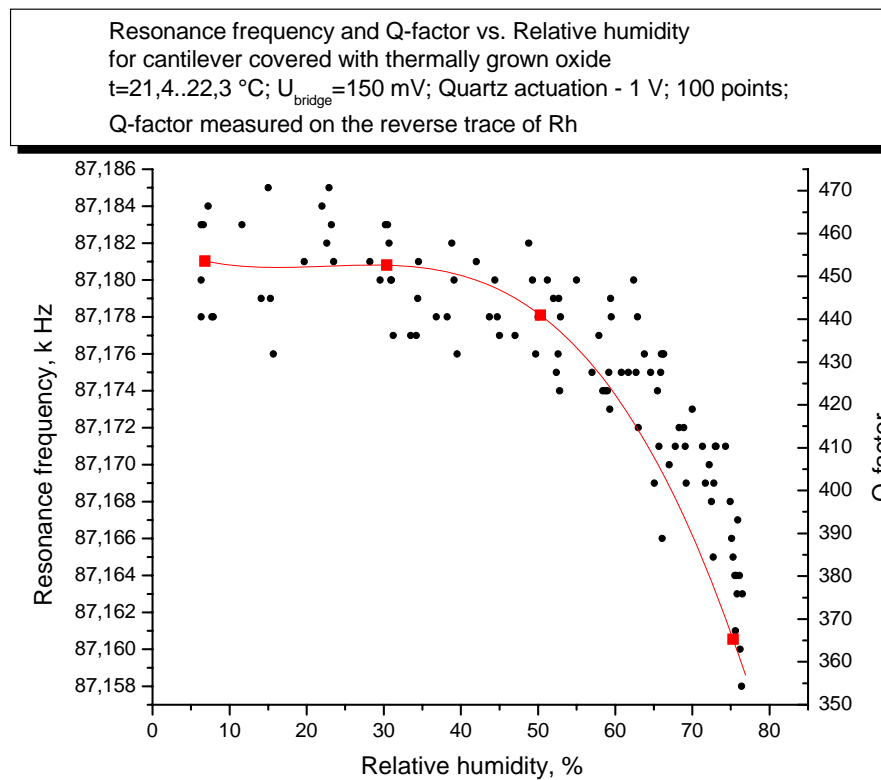


Fig. 70. Resonance frequency and Q-factor vs relative humidity for cantilever with thermally grown oxide.

Other vapours (methanol, ethanol, 2-propanol, and acetone) also invoke the resonance frequency shift as it is shown in Fig. 71. The relative humidity value for these experiments was around 10%.

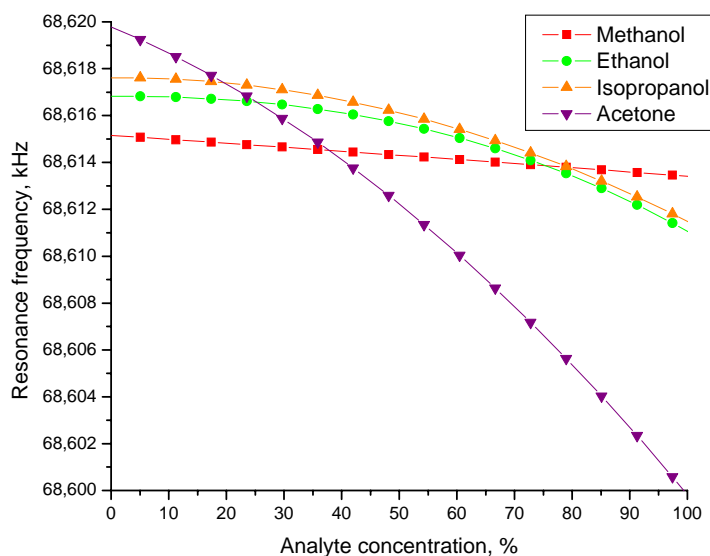


Fig. 71. Uncoated cantilever responses to different analyte concentrations.

The chart in Fig. 72 shows Q-factors for maximum concentration of each analyte.

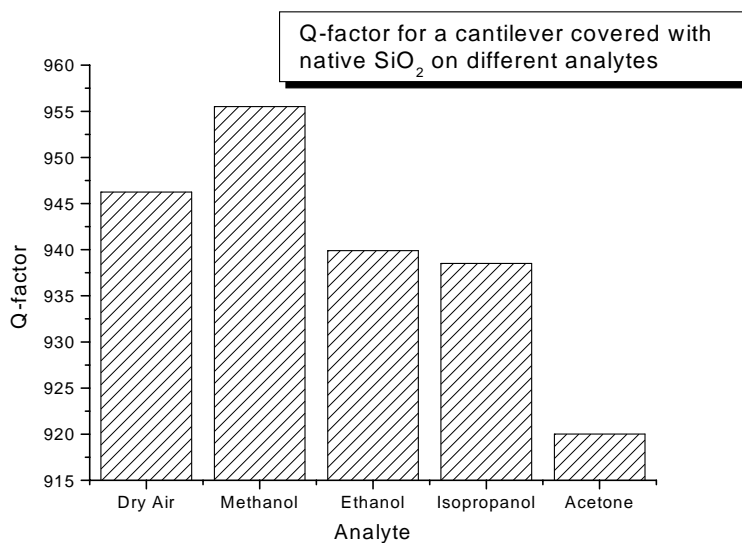


Fig. 72. Q-factor modulation as an additional parameter for chemical recognition.

Obtained results suggest that Q-factor modulation takes place in rather stable manner, thus can be used as an additional information parameter for chemical recognition. Tab. 5 summarizes resonant responses of an uncoated cantilever (namely, readout amplitude, resonance frequency, and the Q-factor) under exposure of the cantilever to different volatile analytes.

	Dry Air	Methanol	Ethanol	Isopropanol	Acetone
Amplitude, mV	780	929	1271	1161	1961
Frequency shift, Hz	0	2	5	6	18
Q-factor	946	956	940	939	920

Tab. 5. Resonance parameters of an uncoated cantilever at different volatile analytes.

Such the way, even uncoated cantilever shows resonance frequency changes according to the first adsorption model (Fig. 62, a) and can be employed as a sensor element without any functionalization. Detection of explosives can be also succeeded by oxide-coated cantilevers, e.g., as demonstrated in [113].

Functionalized cantilevers show sufficiently different responses to volatile analytes. For instance, responses gathered from two calixarene-functionalized cantilevers, which adsorb VOCs according to the third adsorption model (nanostructured sorbent), are illustrated in Fig. 73 in comparison with an uncoated cantilever's responses. All three cantilevers summarized in Fig. 73 were installed into the same measurement cell according to § 3.3.

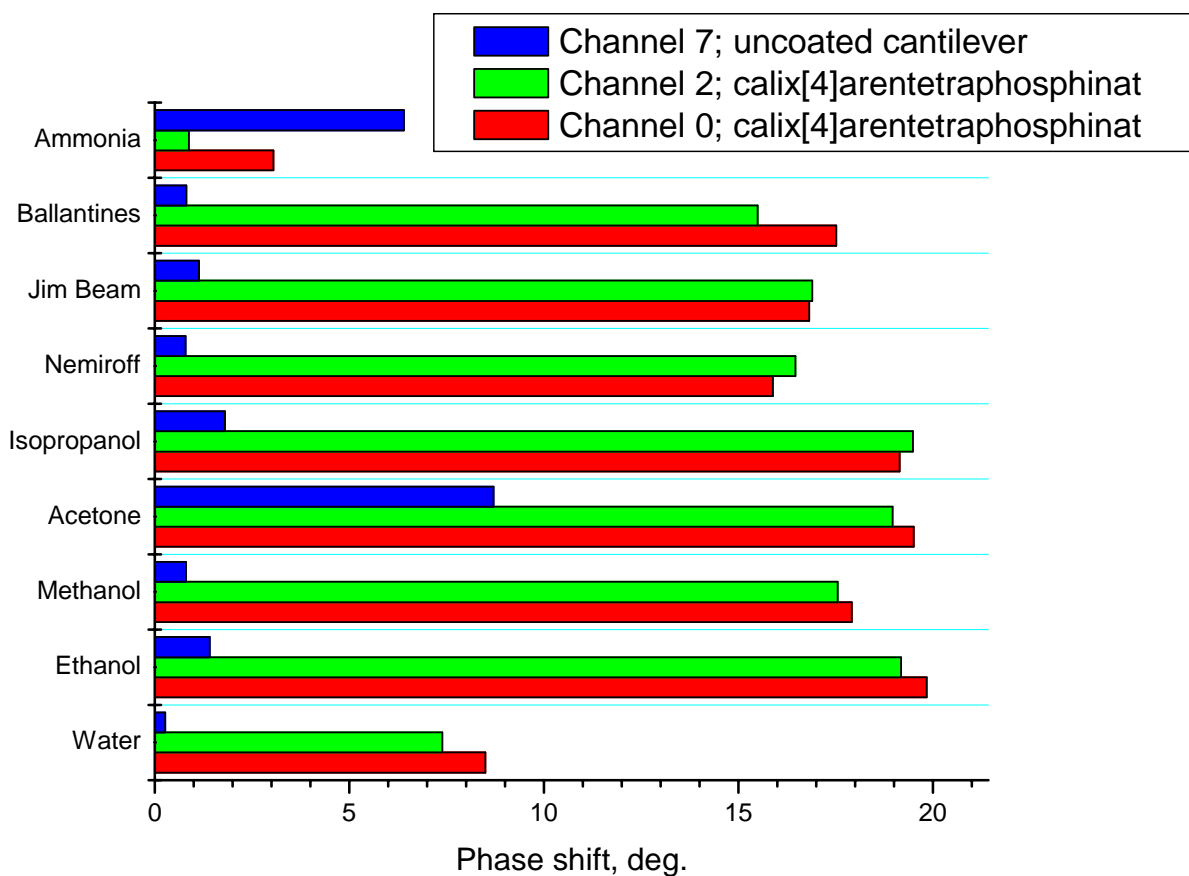


Fig. 73. Responses of three different cantilevers towards various VOCs (at 33 vol. %).

Calix[4]arenetetraphosphinat used for the functionalization is synthesized to be sensitive to ketones and alcohols, but not sensitive to ammonia. This corresponds to our experimental results: sensitivity to ammonia vapours of the functionalized cantilevers is few times lower than for uncoated cantilevers, and up to 20 times higher for alcohols. Binary mixtures of ethanol and water were also exposed. They are represented by Jim Beam, Ballantines, and Nemiroff alcoholic drinks. Sensitivity in their cases is between ethanol and water, but closer to ethanol.

Usually observed 5% discrepancy between equally functionalized sensors suggests us using larger arrays for systems of chemical recognition.

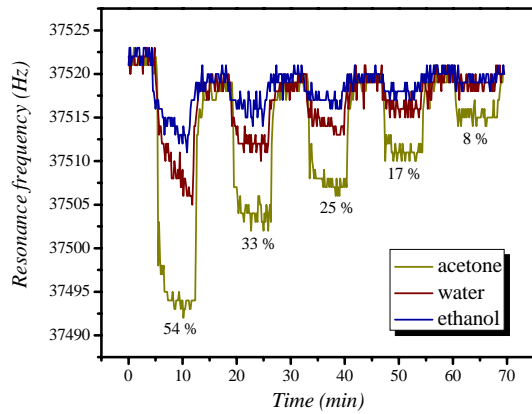
Fig. 73 will be once more considered in § 5.2, devoted to organic coatings in general and calixarenes in particular. Next paragraph proceeds with another example of inorganic coatings, which behaves according to the first sorption model (surface adsorption on solids with low porosity).

4.3. Investigation of chemical and physical adsorption with a chalcohalide-coated cantilever transducer

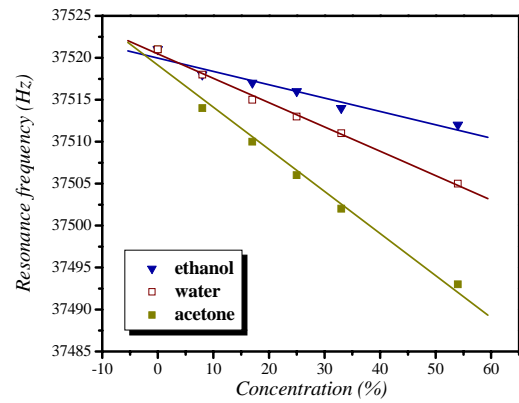
Till now only few papers have reported on chemical sensors based on chalcogenide glassy materials in the form of membranes [114, 115] or thin films [116]. The advantages of these amorphous inorganic materials are that they can be prepared easily and of low costs in bulk and layered form by various methods, they possess high chemical stability and the possibility of variation of their properties due to their disordered amorphous structure, which are common requirements for materials applied in gas sensors. However, the possibility for application of chalcogenide or chalcohalide materials on cantilever-based sensors has not been tested till now.

Thin (120 nm) amorphous $\text{Ge}_{30}\text{S}_{60}(\text{AgI})_{10}$ films were thermally evaporated on the cantilever beam using a slot mask. The films were smooth and uniform in thickness as revealed by means of atomic force and scanning electron microscopies.

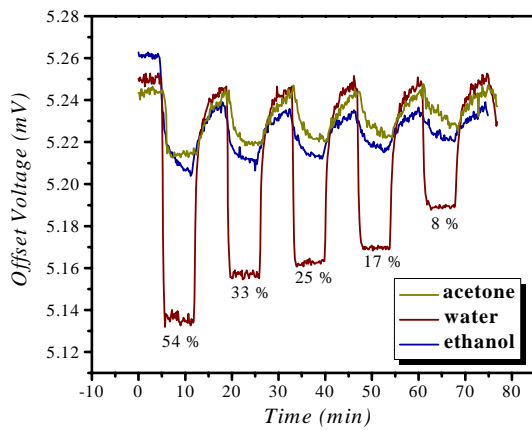
The microcantilever sensor behaviour was investigated in gas flow mode under exposure to different concentrations of water, ethanol, acetone, and ammonia vapours. The measurement cell for these experiments is described in § 3.1. Analyte injection with concentrations between 8 and 54 vol.% into the measurement cell was performed according to the procedure described in § 3.4. The dynamic and static responses (the resonance frequency and the offset voltage, respectively) were measured simultaneously. Fig. 74 (a) shows resonance frequency changes for 3 volatile analytes (water, ethanol, and acetone). Fig. 74 (c) shows offset voltage changes (measure of static cantilever bending) under the same analyte conditions. The signal magnitude increases with the analyte concentration; thus the largest responses were detected for 54 vol. % of each analyte. However, offset voltages versus analyte concentrations are not linear (Fig. 74, d) unlike resonance frequencies plotted versus analyte concentration (Fig. 74, b). Moreover, offset voltage measurements over a large number of experiments showed less stable and predictable behaviour. That is why we rely only on the resonance frequency shift for all experiments discussed below. Our experiments show (see Fig. 74, a and b) that the sensor exhibits the largest sensitivity for acetone vapours, i.e. towards the analyte with the highest molecular weight, and the cantilever acted as microbalance. The higher sensitivity towards water vapours as compared with ethanol could be due to partial penetration of small water molecules with relatively high electric dipole moment 1.85 D ($6.2 \cdot 10^{-30}$ C·m in SI units) into the amorphous film and/or formation of weak bonds with e.g. silver atoms from the sensitive coating. The sensor has a very good linearity over a wide range of analyte concentrations (Fig. 74, b) and a good reversibility (Fig. 74, a), which means that the analytes are primarily physisorbed onto the chalcogenide surface. The responses towards all tested analytes are relatively weak suggesting also physisorption of the gas molecules on the surface of the sensitive layer. Their in-depth absorption is hindered by the dense structure of the amorphous $\text{Ge}_{30}\text{S}_{60}(\text{AgI})_{10}$ films (density of the corresponding bulk sample is $3.2 \pm 0.1 \text{ g/cm}^3$). The leading slope of the analyte injection transition process should be obviously explained by the saturation time of the cantilever cell volume rather than reaction time of the sensor itself.



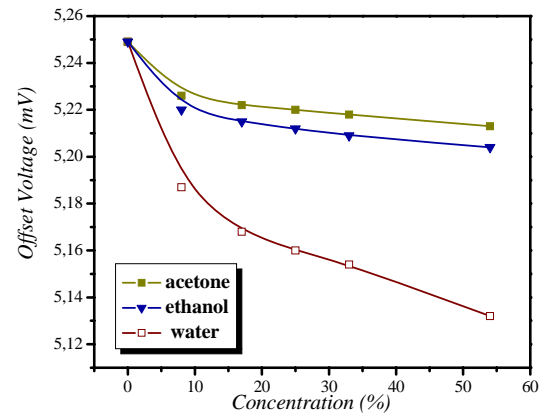
(a)



(b)



(c)



(d)

Fig. 74. Resonance frequency shift (a) with corresponding transfer curve (b); offset voltage modulation (c) with corresponding transfer curve (d) of the cantilever exposed to water, ethanol, and acetone vapours with different concentrations in gas flow mode.

Next set of experiments deals with ammonia detection and is shown in Fig. 75. Initially, the baseline was established by purging the measurement cell with dry nitrogen for 7 min like in the previous experiments. Next peak in Fig. 75 corresponds to the ammonia vapour exposure with 54 vol. % concentration. This exposition leads to a very large resonance frequency shift (360 Hz), which is one order of magnitude higher than for other analytes. Next purging with nitrogen was not able to recover initial baseline, which is now shifted for about 90 Hz. We tried to recover the sensor with water vapour and pure nitrogen in different proportions during several days, but new baseline appeared to be very stable. It means, we have some ammonia molecules chemisorbed onto the sensor coating surface. Consequently, increase of the microcantilever beam mass lowered its resonance frequency.

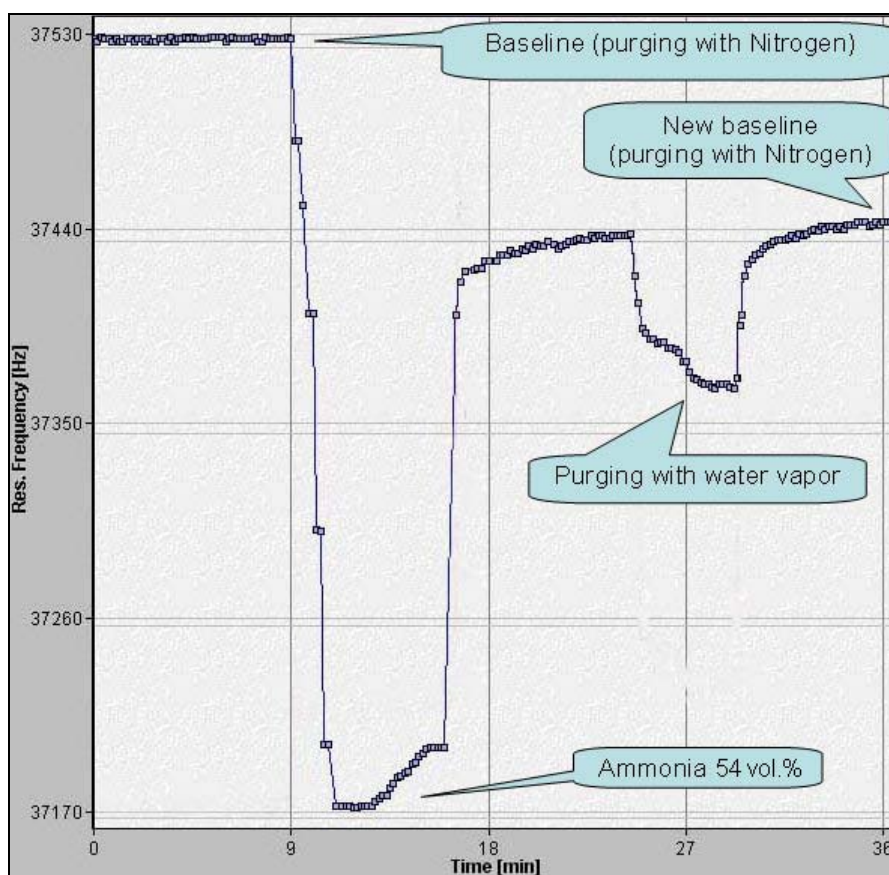


Fig. 75. Chemisorption of ammonia vapour onto chalcohalide-coated cantilever.

The important is that chemisorbed ammonia modified the chalcohalide surface and made it more susceptible for some kinds of physisorbed analytes, e.g., water molecules or explosive nitroaromatic compounds. That is proved by next series of our experiments, which is shown in Fig. 76.

Fig. 76 represents comparison of 3 sets of water vapour exposition. The initial experiment, described above, showed the weakest sensitivity (Fig. 76, a). The chemical modification of the chalcohalide surface with ammonia vapours resulted in the formation of additional binding sites for water molecules as well as in the shift of the baseline down due to the added mass of ammonia molecules onto the cantilever beam (Fig. 76, b). This effect improved drastically the sensitivity towards water vapours (100 Hz shift for 54 vol. % as compared to 16 Hz for the same concentration) as it is seen from Fig. 76.

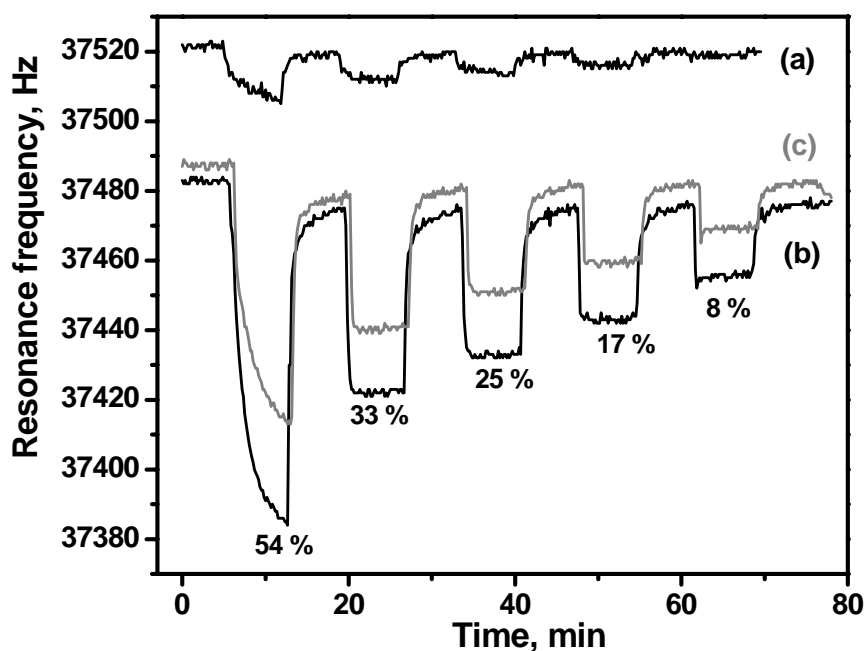


Fig. 76. Sensing of water vapour with chalcohalide-coated cantilever:

- (a) initial (not modified) chalcohalide surface;
- (b) "fresh" chemically modified chalcohalide surface;
- (c) "exhausted" chemically modified chalcohalide surface.

In few days of constant measurements the surface became a little bit "exhausted", i.e. some ammonia molecules were purged out of the cantilever. As a result, the baseline was shifted to the higher frequencies because of the mass loading effect and the sensitivity became worse because of the less number of binding sites (Fig. 76, c). Higher sensitivity was re-established after second processing of the cantilever in ammonia vapour.

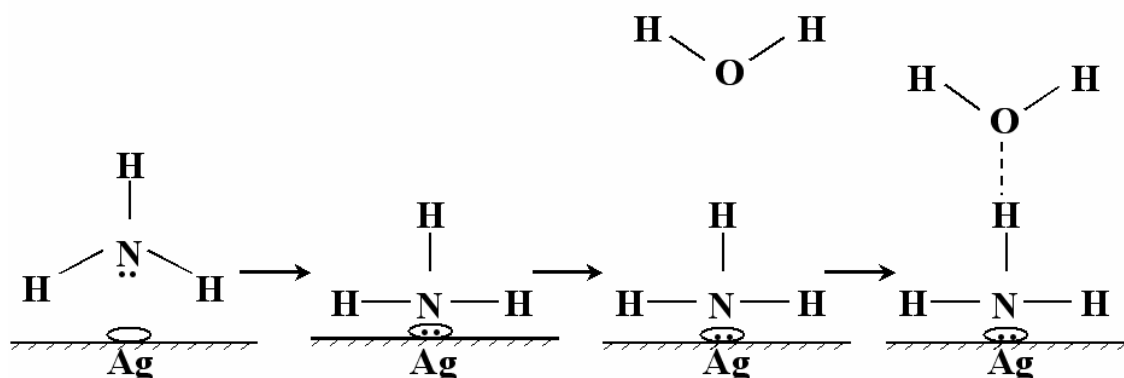


Fig. 77. Chemical modification of chalcohalide surface with ammonia improves capturing of water molecules.

The observed chemical modification of the surface of the Ge-S-AgI coating and the resulting increase of the sensitivity towards water vapours can be explained as follows: silver

due to its high polarizing power and low position in the electrochemical series of elements has a strong tendency towards formation of coordinate bonds, e.g., with NH_3 . The ammonia molecules from the gas phase form donor-acceptor bonds with silver atoms on the surface of the sensitive layer via donation of an electron pair from the nitrogen atom (Fig. 77). The ammonia molecules remain on the cantilever even after purging of the measurement cell with dry nitrogen leading to an increase of the cantilever mass. These NH_3 molecules become sites for interaction upon new exposure to water vapours by formation of hydrogen bonds, which can explain the higher sensitivity of the cantilever sensor.

Fig. 78 summarises relative sensitivity of our sensor for all conducted experiments in chronological order. Each bar in Fig. 78 shows resonance frequency shift, which corresponds to 54 % of certain analyte volume concentration. 2nd, 3rd and 4th bars represent the experiments shown in Fig. 74, which is discussed above. The largest bar represents experiment with ammonia vapour, which is discussed in last paragraph. It is clearly seen, that small sensor sensitivity towards water vapours (about 15 Hz) exhibited during the 1st and 3rd experiments was significantly improved after chemical modification of the surface with ammonia (100 Hz shift). Sensitivity towards acetone vapour was also increased (28 Hz and 45 Hz respectively). Several days of consequent experiments with different gas flow modes resulted in sensitivity degradation, e.g., 8th bar shows the resonance frequency shift of 75 Hz for water vapours. However, one another subsequent modification of the surface with ammonia re-established the sensitivity towards water vapours for 110 Hz, which is similar to those after the first modification.

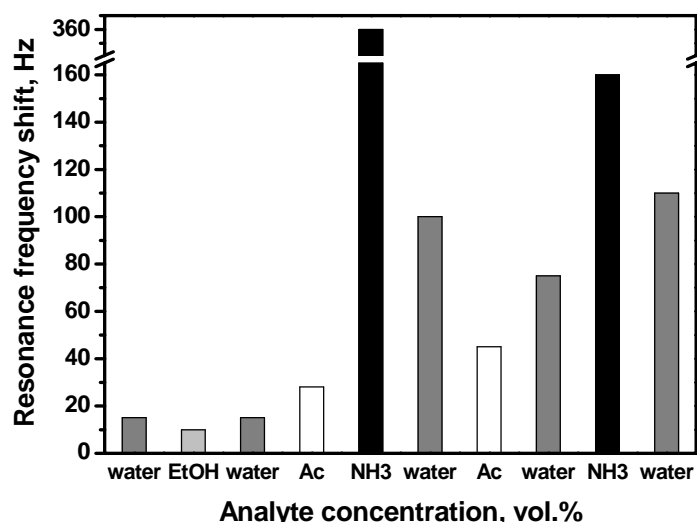


Fig. 78. From left to right: comparison of sensitivities to different analytes in chronological order.

Such the way, cantilever sensor techniques allow us to study physisorption and chemisorption processes, as well as determine material-specific properties such as enthalpy changes during phase transitions.

Ammonia-modified surfaces play an important role in detection of explosives due to the high-affinity binding sites for nitroaromatic compounds, e.g., which are shown in Fig. 79.

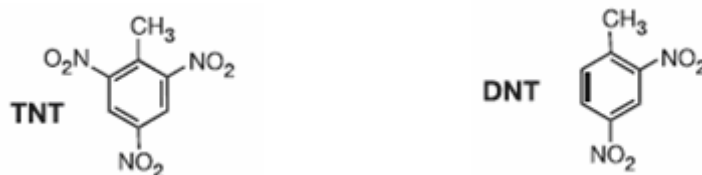


Fig. 79. Chemical formulas of 2,4,6-trinitrotoluene (TNT) and 2,4-dinitrotoluene (DNT).

Highly sticking nitroaromatic compounds, such as trinitrotoluene (TNT), which is the explosive component emanating from most landmines, can be detected with inorganic coatings, e.g., chalcohalide or oxide surface by either added mass or via deflagration on the cantilever surface followed by exothermic reaction.

However, organic coatings would be once again more competitive. Trace vapours of the explosives 2,4,6-trinitrotoluene (TNT) and 2,4-dinitrotoluene (DNT) can be more effectively sensed with gold surface cantilever functionalized by a self-assembled monolayer (SAM) of 6-mercaptopicolinic acid molecules, which is confirmed [117] to have superior specific reaction with TNT molecules to the reported 4-mercaptobenzoic acid SAM [118, 119].

Because inorganic coatings cannot normally provide with high selectivity necessary for many applications, cantilevers functionalized with chemically selective organic layers will be considered in the next chapter.

Chapter 5.

Functionalization of the cantilevers with organic coatings

The previous chapter discussed three sorption models and described the first one – adsorption onto thin solid inorganic surfaces as an obvious example how chemical or physical adsorption may influence the cantilever operation. However, for reliable detection of targeted analytes, inorganic coatings exhibit less selectivity and sensitivity in comparison with specially selected organic functionalization coatings. The latter have been represented in the present investigation by organic polymers, which react with swelling under analyte adsorption (most usually according to the second sorption model, see Fig. 62, b) or nano-structured organic zeolites - calixarenes (third sorption model, see Fig. 62, c).

5.1. Investigations on microcantilevers functionalized with organic polymers

Various commercially available “generic” polymers, e.g., poly(methyl methacrylate), polystyrene, polyurethane, and their co-polymers, have responded differently to various VOCs [120, 121]. Detection of water vapour has been described by using hydrophilic coating, such as poly(N-vinylpyrrolidinone) and poly(ethyleneglycol) [122] as well as with gelatine-coated cantilevers in [57]. Conventional photoresist layer undergoes swelling in presence of organic vapours. It can be used for cantilever functionalization in static deflection mode with sensitivity as low as 10 ppm (in the case of ethanol) [123] or in dynamic resonant mode, as it is demonstrated in our studies, e.g. photoresist AZ1518 shown in Fig. 33 and described therein.

Functionalization technique depends on the material to be deposited. Generally, cantilevers are functionalized by one of the following procedures:

- dipping into a polymer solution or incubation in dimension-matched glass capillaries [12];

- micropipetting [22] or coating using an ink-jet spotting device [12];
- spray coating (air-brushing) [14];
- spin coating;
- thermal vacuum evaporation;
- chemical vapour deposition from plasma source;
- lateral self-organisation of molecular mono- and multi-layers (SAM and LB-techniques described below).

In this study we used to functionalize the cantilevers with such organic polymers as PMMA (polymethyl methacrylate), PVP (polyvinylpyridine), SAN (styrene-acrylonitrile copolymers), Formvar™, VCl-VA (vinylchloride-vinylacetate copolymer), photoresist AZ1518, etc. A layout example of differently polymer-functionalized cantilevers is shown in Fig. 80.

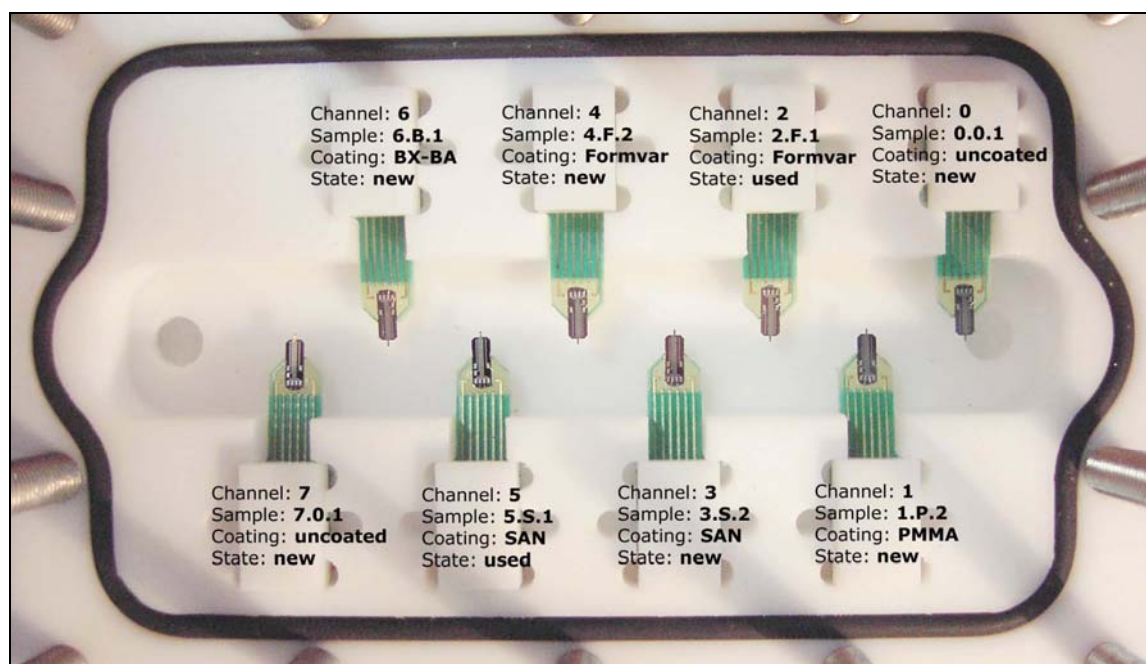


Fig. 80. 8-cantilever sensor layout ready for measurements.

Most usually the polymers were deposited by dipping technique using micromanipulator shown in Fig. 81.



Fig. 81. Cantilever functionalization by dipping into polymer solution.

Deposition of a polymer definitely influenced the resonance frequency of the cantilever and its Q-factor as well similarly to the mass load effect described above, as it is shown in Fig. 82. Resonance frequency was measured before and after dipping into the polymer solution, thus the deposited polymer mass could be calculated.

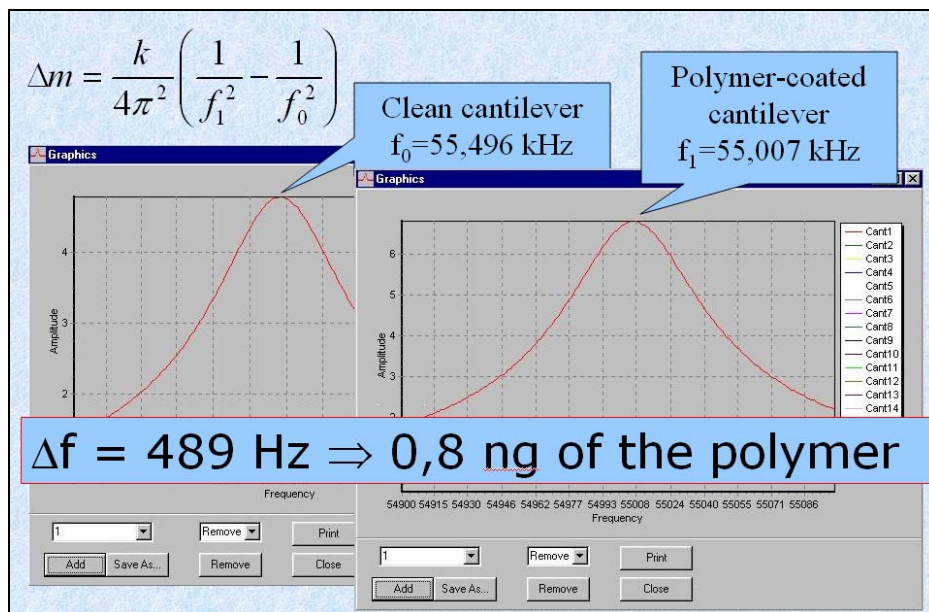


Fig. 82. Cantilever responses before and after dipping into polymer solution.

Since thermal actuation may influence morphology of the polymer layer, we checked the effect. Using an optical microscope, we observed polymer layer before and after heating. We

conclude that the layer structure shows no noticeable changes after being operated with integrated thermal actuator. A captured example is presented in Fig. 83.

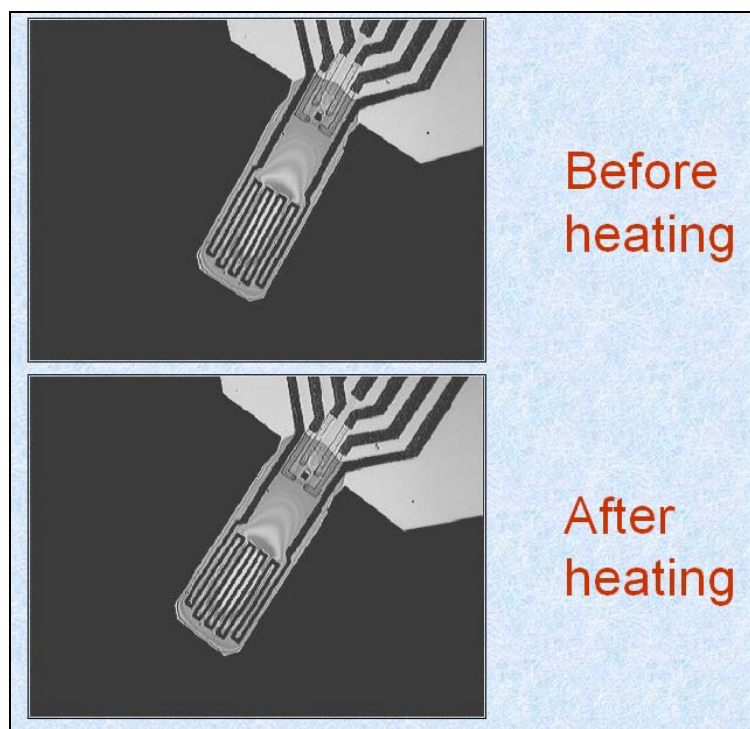


Fig. 83. Polymer layer structure before and after operation with thermal actuator.

In the frame of this work, recognition performance of a 4-cantilever array functionalized by different coatings has been investigated and published [22]. Identification of individual analytes and their binary mixtures has been performed by using 2 commercially available organic polymers, polydimethylsiloxane (PDMS) and polyvinylpyridine (PVP), and also amorphous nitrogen-rich carbon nitride films (CN_x) as sensitive layers. The polymers were dissolved in toluene and ethanol, respectively, and deposited onto one side of the cantilevers by a micropipette. These polymers have been selected in a way to provide different selectivity and sensitivity toward various analyte vapours. The other two cantilevers of the array were functionalized with CN_x films of different thicknesses (240 nm and 120 nm). The CN_x functionalization layers have been prepared by inductively coupled plasma chemical vapour deposition (ICP-CVD) utilizing transport reactions from a solid carbon source [21]. The films were thoroughly investigated with respect to their morphology, structure, composition, chemical bonding structure and mechanical properties [21]; they exhibit particular sensitivity towards humidity. The functionalized 4-cantilever array is shown in Fig. 84. The measurement set-up for these experiments is described in § 3.2.

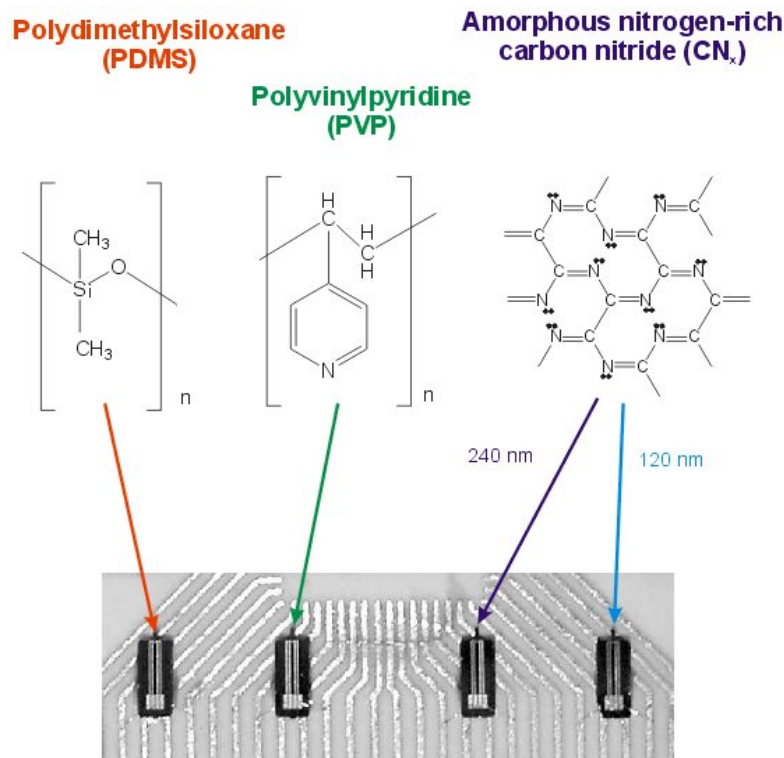


Fig. 84. Functionalized 4-cantilever array.

Since the detection of water vapours plays an important role in many sensor applications, the cross-sensitivity of the functionalized cantilevers toward water vapours was initially tested. The relative humidity in the test cantilever cell was real-time monitored by a commercially available capacitive-type reference humidity sensor MiniCap2 by Panametrics. Fig. 85 shows the acquired cantilever responses plotted versus relative humidity in the cantilever cell.

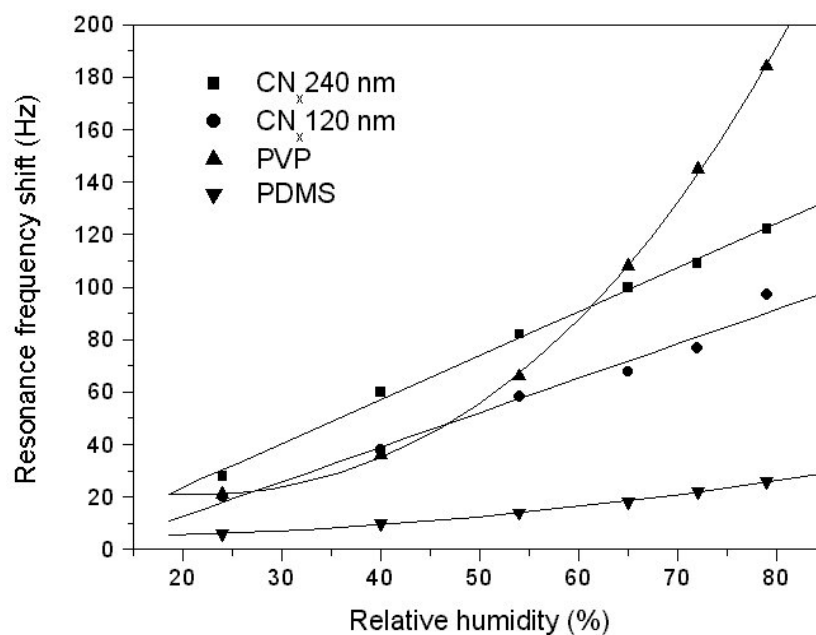
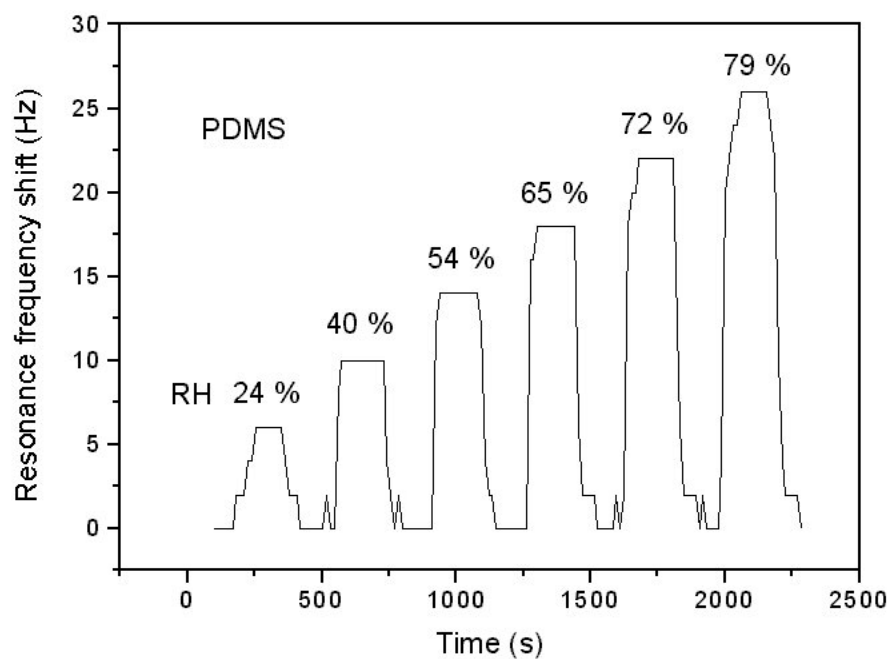


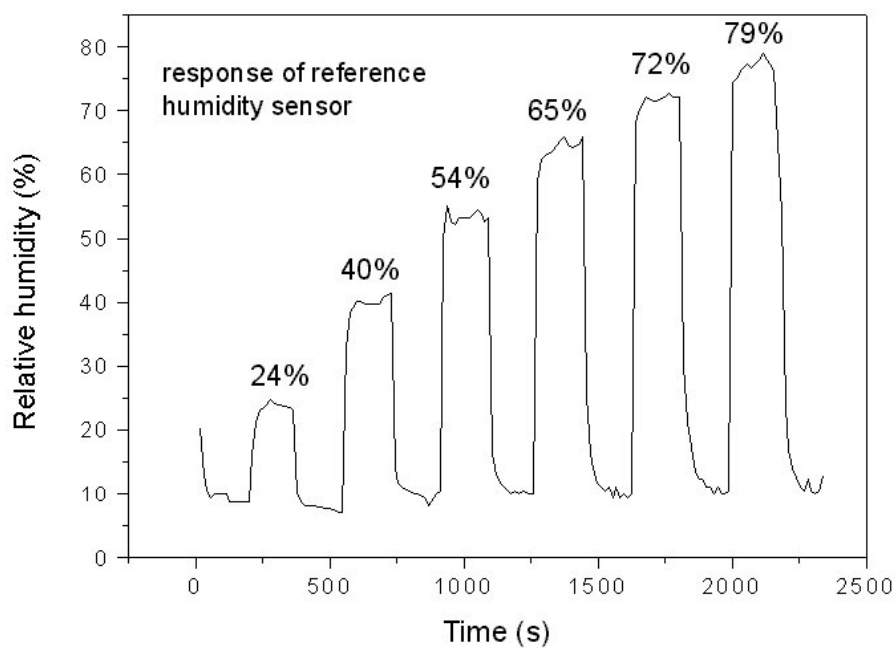
Fig. 85. Calibration curves of the cantilever array towards water vapours.

The resonance frequency shift is due to the interaction between the analyte molecules and the sensitive layers, resulting in an increase of the load mass and consequently a decrease of the resonance frequency. The chemical nature of the sensitive coatings determines their hydrophilicity, polarity, extent of swelling (in some cases), and influences the recognition performance of the functionalized cantilevers toward water vapours. The PVP-coated cantilever shows the largest response since the polymer is water-soluble and strongly absorbs water. The process leads to swelling and softening of the sensitive material at high humidity values, resulting in a deviation from the linear dependence of the resonance frequency shift on the humidity. The cantilevers coated with CN_x films exhibit responses in the intermediate range of frequency shift; the dependence on the humidity is more linear as compared to the PVP functionalized cantilever. The CN_x layers are built from $>C=N-$ units forming a network with porous structure. The polar water molecules can penetrate into this fine structure; this process is additionally enhanced by the polar character of the CN_x material (composed of C-N dipoles). We found that the sensitivity of the cantilevers coated with CN_x increases by increasing the film thickness. The H_2O molecules most probably form hydrogen bonds with the N atoms of the films not only on the surface, but also in depth of the sensitive layer. This trend is more pronounced for the thicker film (240 nm), which allows more moisture to penetrate, consequently resulting in a higher sensitivity. For thinner films (120 nm) the mass hygroscopicity is limited by the smaller volume for penetration of water molecules. In principle both surface adsorption and in-depth absorption phenomena can contribute substantially to the sensitivity towards water molecules. On the base of the results obtained one can assume that the humidity detection takes place more or less in the bulk of the CN_x films; thus the sensitivity can be increased by increasing the thickness of the sensitive layer. This behaviour of the CN_x films has been confirmed once again by the experiments with alcohols as shown below. The PDMS-coated cantilever is the least sensitive toward water vapours from all four cantilevers in the array.

The time responses of the cantilevers were monitored with increasing the humidity in the cantilever cell with one and same injection time. All responses were fast and reversible (Fig. 86, a), even for the PDMS-coated cantilever, which is relatively insensitive toward water vapours. For comparison, Fig. 86 (b) shows the responses of the reference humidity sensor.



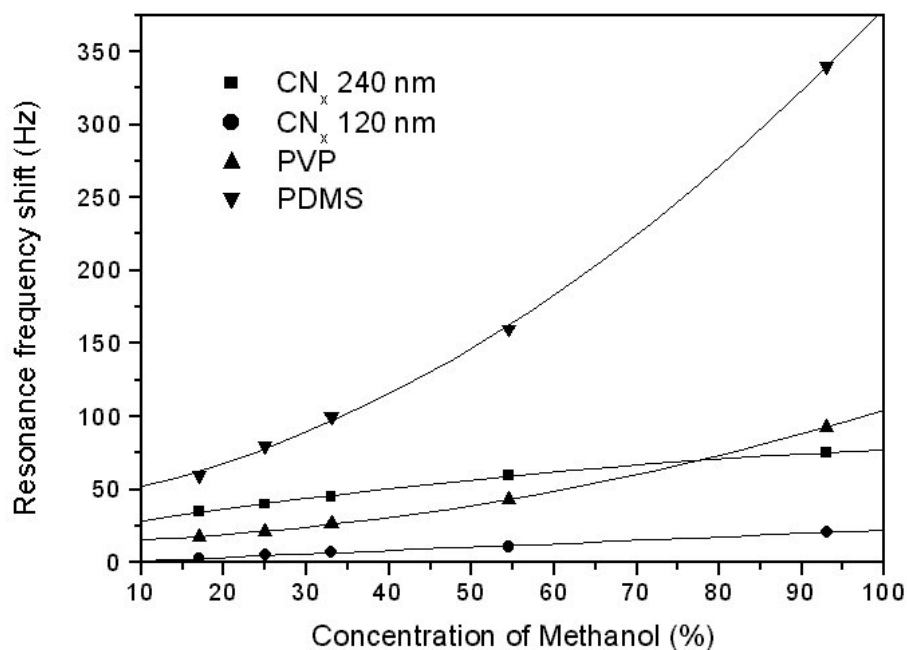
(a)



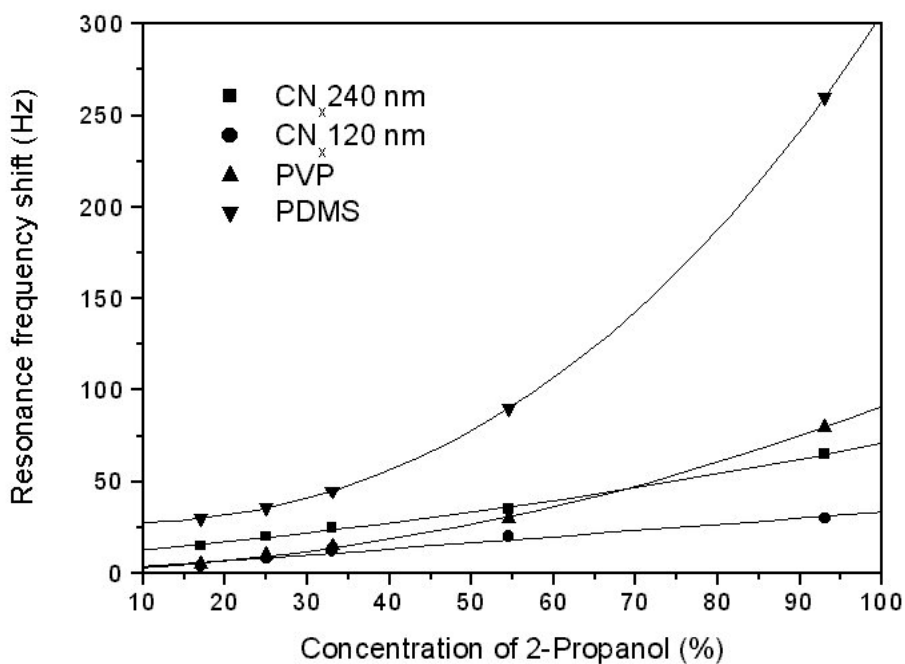
(b)

Fig. 86. Time responses of the PDMS-coated cantilever (a), and the reference humidity sensor (b).

Further, the behaviour of the cantilever array on exposure to various concentrations of methanol (Fig. 87, a) and 2-propanol (Fig. 87, b) has been analysed. During the experiments the relative humidity and the temperature in the cantilever cell were kept constant at 10% and 22°C, respectively.



(a)



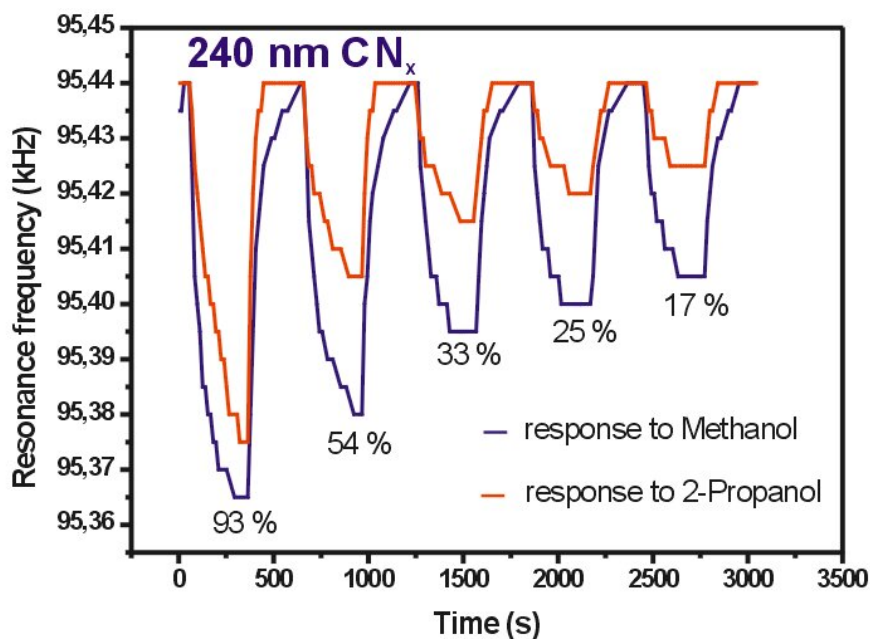
(b)

Fig. 87. Cantilever responses vs. methanol (a) and 2-propanol (b).

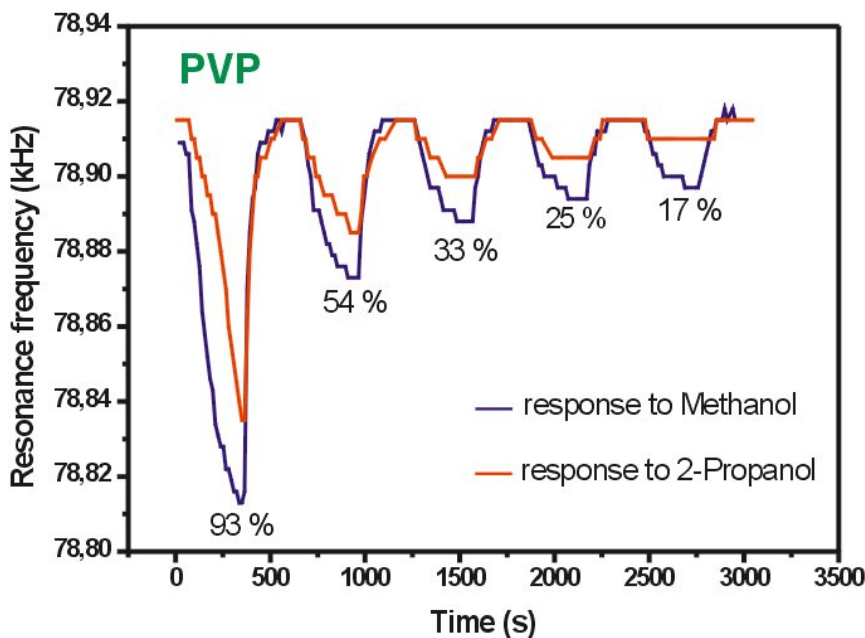
The largest responses were detected for the PDMS-coated cantilever in contrast to the case of exposure to water vapour. The frequency shift of the sensor coated with 240 nm CN_x is larger compared to that with 120 nm CN_x, indicating higher sensitivity with increasing the thickness, as discussed above. The sensor with the thicker CN_x coating tends to saturation at higher analyte concentrations, which is not observed for the thinner one. The responses to 2-propanol were smaller compared to those to methanol with the exception of the cantilever coated

with 120 nm CN_x film. The thinner CN_x layer is more sensitive to 2-propanol, i.e., toward the analyte with the smaller dipole moment but the higher molecular weight. The cantilever seems in this case to act as a microbalance, distinguishing between the two alcohols by the difference in their molecular weights.

The time responses of the cantilevers were monitored on exposure to alcohols with different concentrations (Fig. 88).



(a)



(b)

Fig. 88. Dynamical responses of cantilevers coated with 240 nm thick CN_x (a) and PVP (b).

In the case of 240 nm CN_x film, the smaller molecular size and the higher dipole moment of the methanol causes a higher penetration ability and stronger interactions between CN_x

material and analyte molecules resulting in larger response signals and longer recovery time as compared to 2-propanol (Fig. 88, a). In contrast to the 240 nm thick CN_x film, the recovery times of the PVP-coated cantilever during the purging are nearly the same for the two analytes within the whole concentration range investigated (Fig. 88, b).

In a further series of measurements, the cantilever array was exposed to four test binary mixtures with different concentrations of methanol and 2-propanol. Fig. 89 represents the response patterns of the sensors depending on the analyte ratio in the binary mixtures.

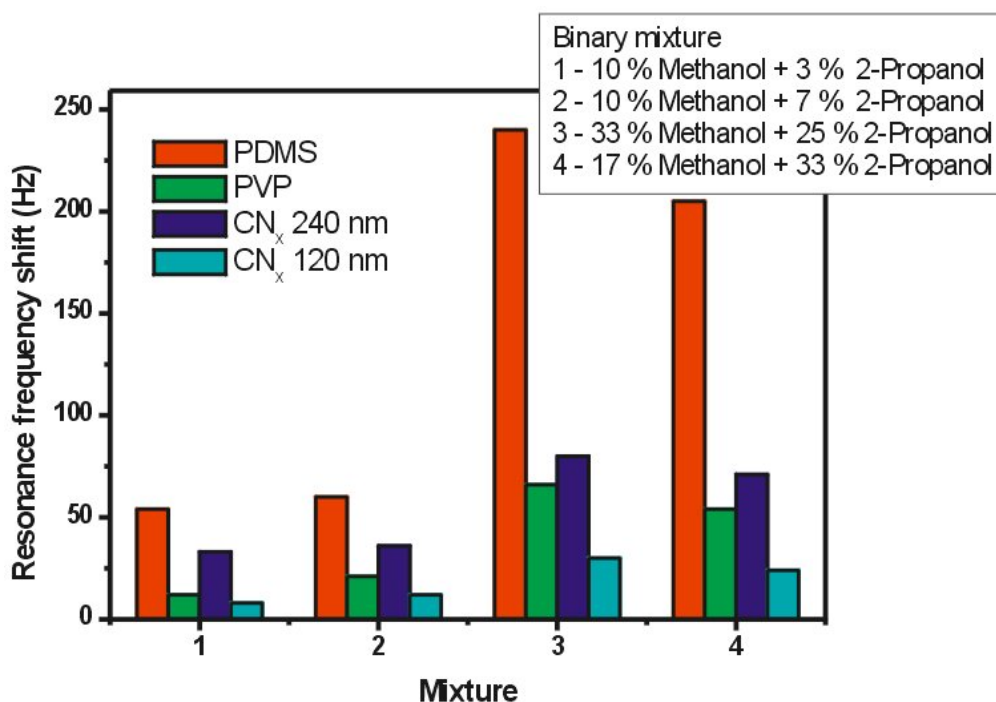


Fig. 89. Response patterns of the cantilever array upon exposure to binary mixtures of methanol and 2-propanol.

From a comparison with Fig. 88 (a) and Fig. 88 (b) it can be seen that those for a given mixture are larger than the responses for the individual analytes with the same concentrations; however, they are not simply a superposition of the responses of the individual alcohols. As expected, the largest responses are observed for the PDMS-coated cantilever, which has shown the highest sensitivity toward both alcohols. The sensors exhibited a higher sensitivity to the variation of the methanol concentration as compared to those of 2-propanol.

In order to investigate the cross-sensitivity of the sensors toward methanol at different relative humidities, we tested a second group of binary mixtures of methanol and water vapours using the same mixing technique and concentrations; the results of these experiments are shown in Fig. 90. The sensor signals decreased as compared to the first binary mixtures with the exception of the cantilever coated with 240 nm CN_x film. The higher sensitivity of the thicker CN_x film toward water vapours in the considered concentration region caused an increase of the

sensor response; the signal for the fourth binary mixture was even stronger than that of the PDMS-coated cantilever.

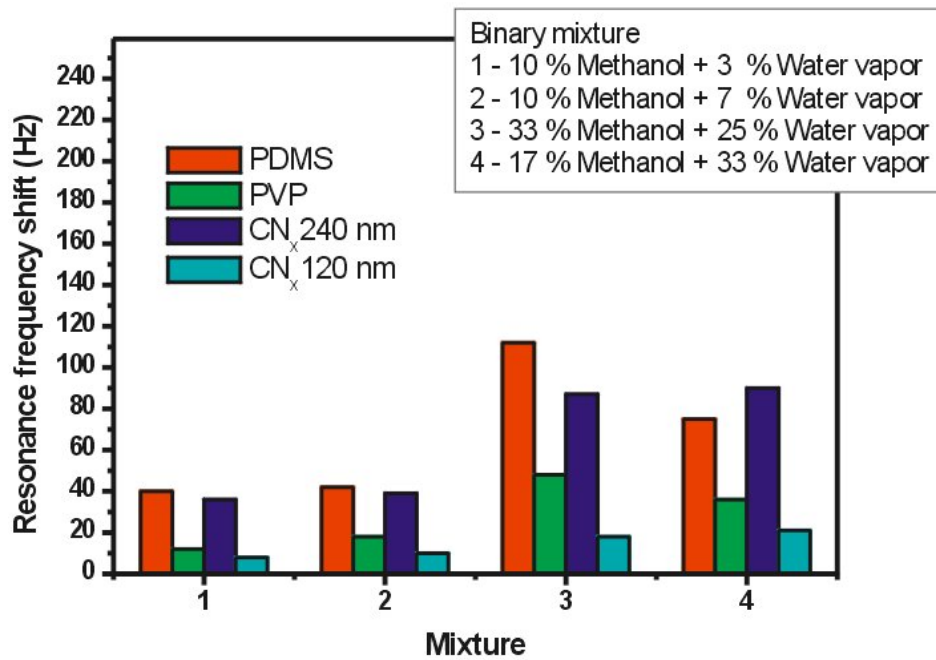


Fig. 90. Response patterns of the cantilever array upon exposure to binary mixtures of methanol and water.

The transient responses of the cantilever coated with PDMS exhibited a significant difference in the recovery time. Fig. 91 illustrates the time responses of this sensor to methanol, 2-propanol and two binary mixtures.

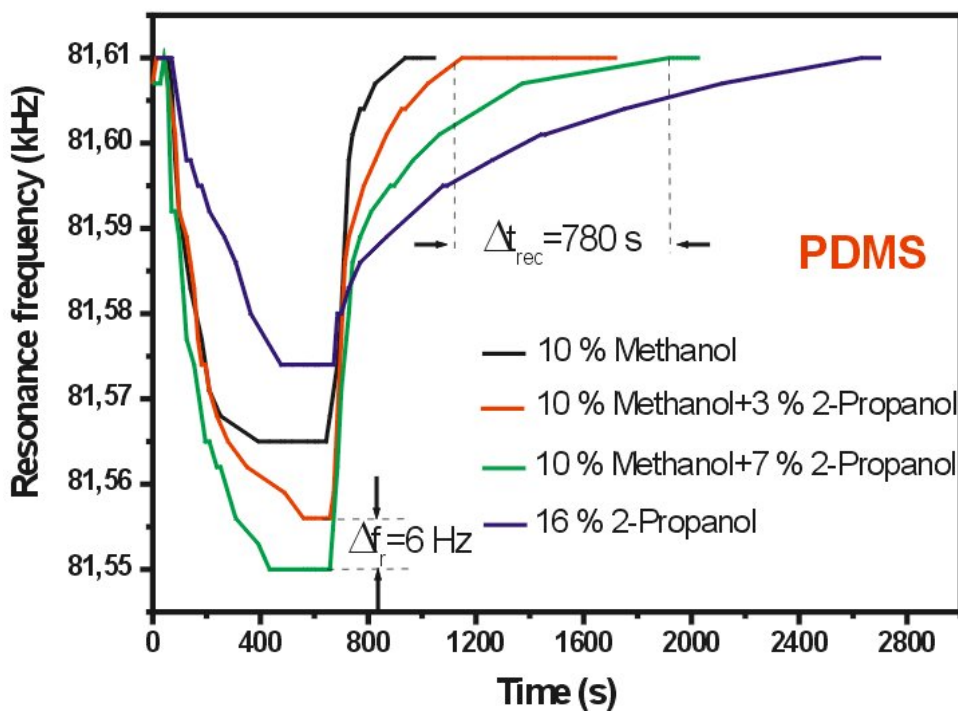


Fig. 91. Time response of the PDMS-coated cantilever upon exposure to methanol, 2-propanol, and their binary mixtures.

In contrast to the fast recovery time for methanol, the cantilever needs much longer time to reach the initial resonance frequency for 2-propanol. A rather small difference between the concentrations of 2-propanol in the binary mixtures causes a relatively small frequency shift of approximately 6 Hz, but at the same time a much larger difference in the recovery time. The diversity in the recovery time of the PDMS-coated cantilever upon the alcohols tested and their binary mixtures with small variation of the concentrations can be successfully used as a second characteristic, in addition to the resonance frequency shift to discriminate the individual components in the analyte mixtures.

In order to improve selectivity and sensitivity of microcantilever-based sensors, calixarene functionalization coatings, which enable specific host-guest interactions, have been studied and described in the next section.

5.2. Calixarenes as novel functionalization materials

Calixarene is a wide class of cyclic oligomers, which has not been well investigated by the moment for sensor applications. They have been described mostly from the point of view of their synthesis and also their chemical and physical properties [124]. However, only few types of calixarene-coated transducers have been developed until now. They include ion-selective electrodes (ISEs) [125], ion-selective field effect transistors (ISFETs) [126], electrolyte-insulator-semiconductor sensors (EIS) [127], quartz-crystal microbalances (QCMs) [128], and optodes [129]. Our pioneering experimental results showed them to be very promising as organic nanosized receptors for chemical gas sensors based on nanoparticle gold films [20, 130] and microcantilevers. In our studies, thin films of calixarene derivatives have demonstrated excellent sorption abilities and selectivity, long time stability, technological feasibility. Depending on the deposition technique, both molecularly ordered (e.g. Langmuir-Blodgett-deposited) or molecularly disordered (e.g. thermally evaporated) calixarene layers are of great interest in chemical liquid and gas sensors due to their unique zeolite-like capacity and excellent selectivity features as well.

Name “calix” originates from Greek word chalice, which means “bowl” or “cup”, whereas “arene” denotes aromatic rings, which total number is represented in square brackets, e.g., calix[6]arene. Fig. 92 shows spatial architecture of a calix[4]arene molecule. The aromatic rings constitute a cup-shaped cavity, which is suitable for encapsulating of ions or neutral species. Different complexing groups at a wide upper rim and a narrow lower rim of calixarene are able to attract target molecules with pre-defined selectivity. Additionally, the functional groups are responsible for physical properties of calixarene molecules. Small molecule can be

also captured and released by the apolar hydrophobic cavity in host-guest interactions. This phenomenon determines zeolite-like behaviour of calixarenes at the nano-scale, including excellent desorption ability. Enhanced stability is an inherited fundamental property of aromatic compounds.

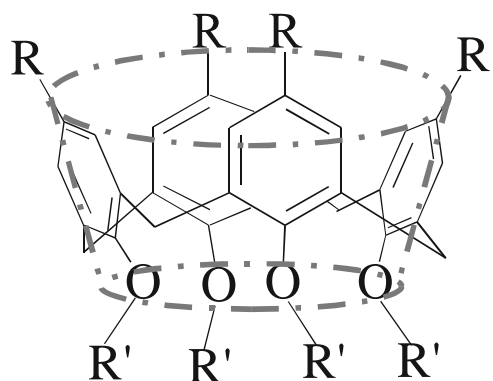


Fig. 92. Spatial architecture of calix[4]arene molecule.

The size of the molecular cavity obviously depends on the number of the aromatic rings, which constitute the macrocycle. X-ray structure analysis of calixarenes shown in Fig. 93 clearly reveals this phenomenon. Calixarenes built of 4 aromatic rings have the cavity volume of approximately 10 \AA^3 .

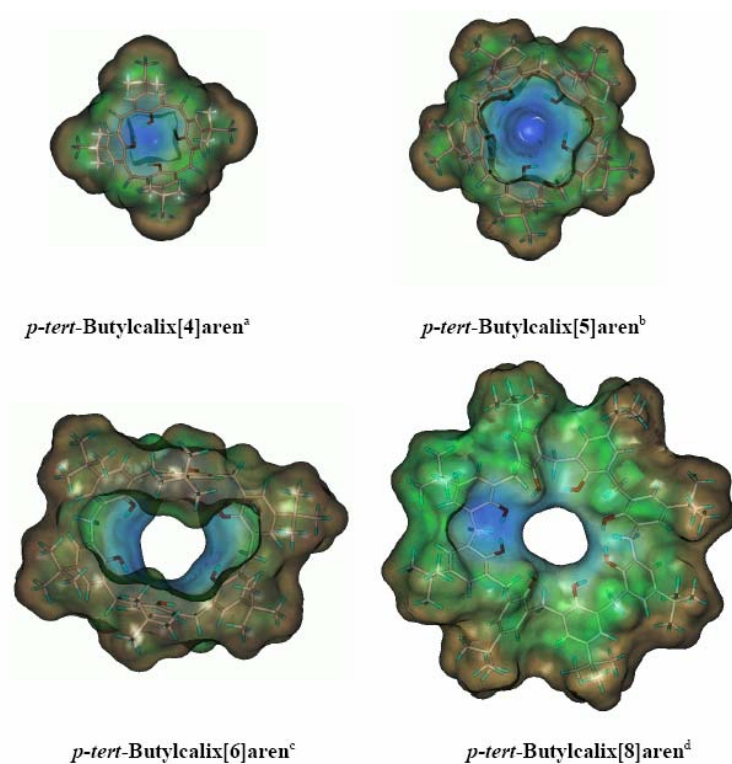


Fig. 93. X-ray structure analysis of calixarenes: the adsorbed molecule can be captured by the hole. [131]

Spatial architecture of calixarenes may have different conformations, as it is shown in Fig. 94. It means that each of the phenol rings can turn upside down because calixarenes possess rotational degrees of freedom around the single bonding between the aromatic rings. In our studies, cone conformations of calixarenes were investigated.

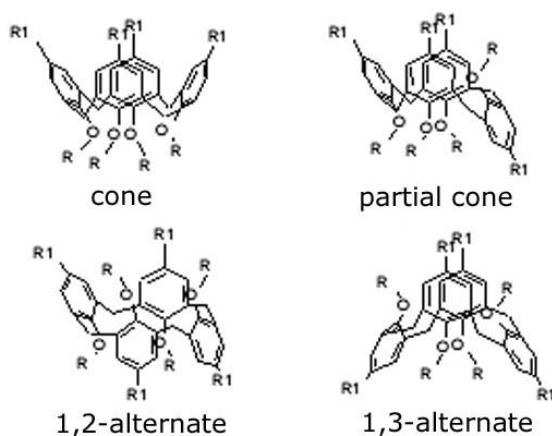


Fig. 94. Conformations of calix[4]arene: cone (a); partial cone (b); 1,2-alternate (c); 1,3-alternate (d) [124].

Calixarenes can be immobilized onto solid surfaces in different ways. An example of silicon surface pre-treatment, calixarene anchoring, and guest molecule adsorption is shown in Fig. 95.

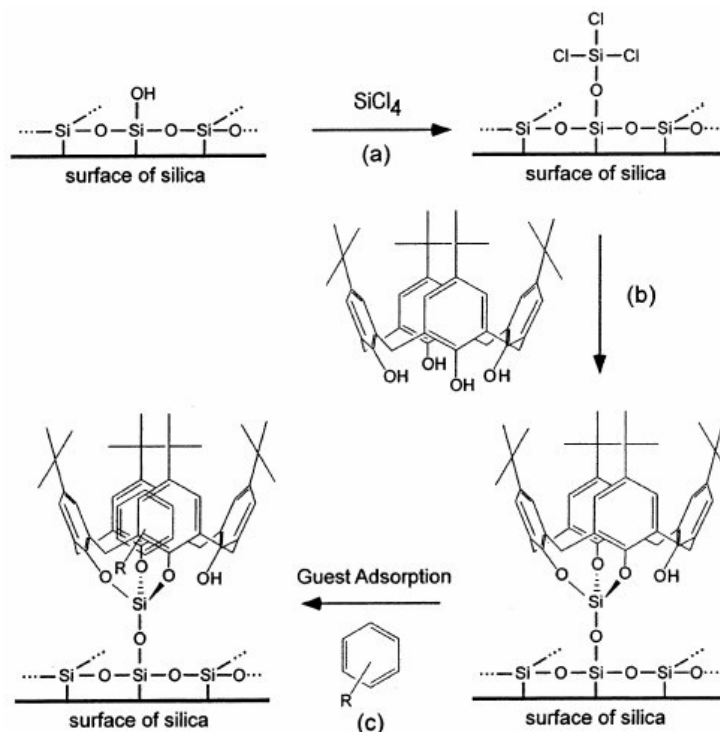


Fig. 95. Schematic illustration of the immobilization of tert-butyl-calix[4]arene onto silica and subsequent use of anchored site for small-molecule adsorption comprising (a) activation of silica surface with silicon tetrachloride, (b) reaction of the activated surface atom with calixarene, and (c) adsorption of small-molecule guest onto immobilized host [132].

In order to utilize a chemical sensor, it must have a particular selectivity to specific species, without which it would not be able to differentiate between different chemical substances. Such specificity can be achieved using the principles of molecular recognition, based upon the concept of a host molecule / guest molecule interaction. In designing host molecules, a series of criteria must be considered in order for effective binding to take place. The key criteria are:

- the host must contain functionalities, which can electrostatically attract charged species;
- the host must also have the appropriate pre-organization, which can selectively hold the guest molecule;
- the binding event must be detectable by either spectral and/or electrochemical techniques.

Calixarenes have inherited an appropriate pre-organization of the host molecule, because the calixarene macrocycle is shaped like a conical basket, where it possesses a lower rim and an upper rim. In addition to the number of aromatic rings, which constitute the macrocycle, a variety of functionalities determine diversity of calixarene family.

For example, the lower rim of *tert-butyl-calixarene* contains polar hydroxyl (–OH) groups, while nonpolar hydrophobic (tertiary butyl^{*}) groups are located at the upper rim of the macrocycle, as it is shown in Fig. 96.

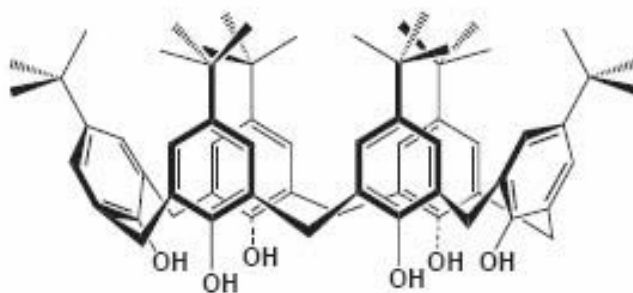


Fig. 96. *tert-butyl-calix[6]arene*, comprising six CH_2 -bridged phenyl rings. The conformation, where substituents at the phenyl rings show into the same direction, is called 'cone'. [133]

The lower rim hydroxyl groups of *tert-butyl-calixarene* are spatially oriented inwards the cavity. Such a way, they can encapsulate various charged species via polar interactions. Consequently, the lower rim of the *tert-butyl-calixarene* is of interest in host/guest interactions.

^{*} *tert-butyl* group: $(\text{CH}_3)_3\text{C}-$ (fully systematic name "1,1-dimethylethyl").

Selectivity for specific host species can be achieved by selectively *functionalizing** the lower rim hydroxyl groups. A series of various classes of functionalities (e.g. esters, amides, phosphines, phosphine oxides, etc.) can be introduced into the lower rim with each class of functionality demonstrating specificity for target cation hosts.

On the contrary to *tert-butyl-calixarenes*, *resorcinarenes* have longer hydrophobic radical tails (alkyl chains $-C_{11}H_{23}$) at their lower rims, while the upper rim radicals contain OH-groups, which naturally possess high hydrophylicity (see Fig. 97). This makes highly amphiphilic *resorcinarenes* very suitable for Langmuir-Blodgett (LB) deposition (Fig. 98), which saves spatial distribution of the long tails. Thus LB-deposited *resorcinarenes* should be more susceptible to longer alkanes than thermally evaporated ones due to a deeper interdigitation of the alkyl chains maximizing van der Waals contacts. The number of layers in a multilayer is readily controlled by the number of dippings.

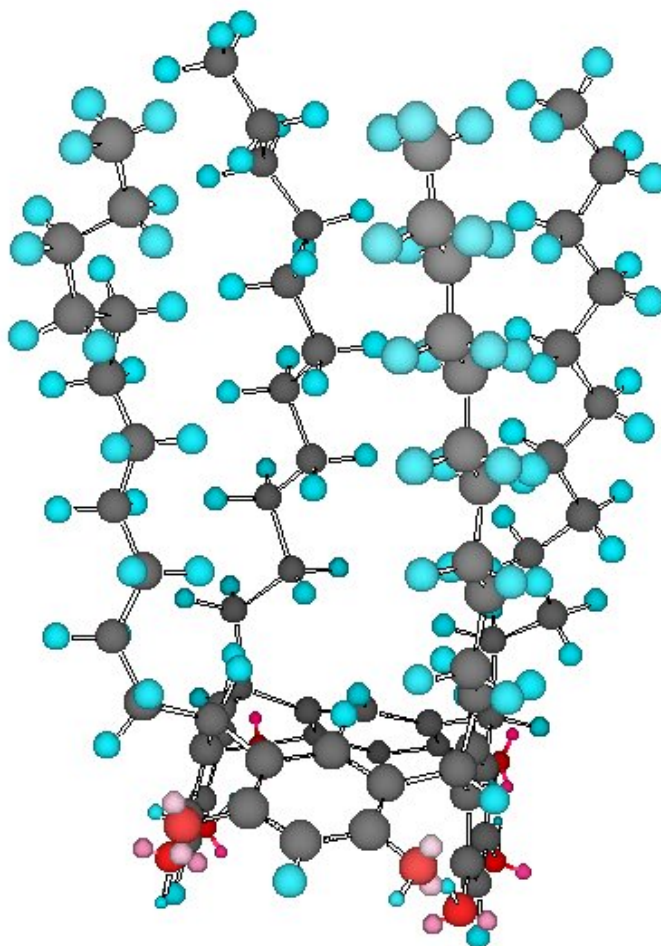


Fig. 97. Illustrative representation of calix[4]resorcinarene molecule architecture.

* Here the term “functionalization” is used in respect to the calixarene molecule, which from the chemical point of view can be considered as “sensor” instead of more conventional appellation of the term in respect to the transducer.

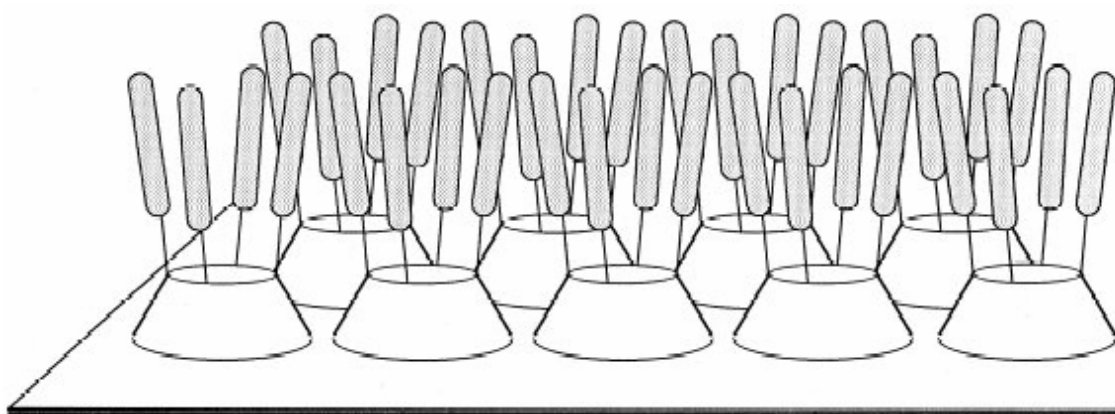


Fig. 98. Calix[4]resorcinarene Langmuir-Blodgett monolayer. [134]

The presented study concerns investigations of calixarene-coated microcantilevers in partial comparison with other mass-sensitive transducers - Quartz Crystal Microbalances (QCM). QCM operate as molecular balances, which register adsorbed mass changes at ppm level. The interaction of the receptor layer, which is deposited on one of the electrodes, with the analyte determines a frequency shift according to the Sauerbrey equation [135]:

$$\Delta f \approx -\frac{2f_0^2}{A\sqrt{\rho_q\mu_q}} \Delta m, \quad (100)$$

where f_0 is fundamental frequency, A is the effective quartz area, μ_q – the “piezoelectric stiffness” and ρ_q – the quartz density. Following the change of quartz frequency one can easily observe adsorption-desorption processes with high resolution (approximately $10\dots 20 \text{ ng}\cdot\text{Hz}^{-1}\text{cm}^{-2}$). Relation (100) is valid if frequency shift Δf is less than 2% of f_0 . Similarly to other transducer types, QCM selectivity has been achieved by varying calixarene type, thickness and deposition technique.

Both microcantilevers and QCM can be functionalized with calixarenes by using different deposition techniques, such as LB-technique, thermal vacuum evaporation, dipping, spin-coating, dropping or air-brushing. However, it is important to emphasize that different calixarene types either have their own optimal deposition technique or some deposition techniques may not be applicable for the given calixarene subclass. For instance, it was found that thermally evaporated *tert-butyl-calixarenes* had shown the most repeatable and stable responses in

comparison with other deposition techniques, whereas *resorcinarenes*, which possess a greater inherent amphiphilicity than simple calixarenes, had shown their best sensor performances being deposited by LB-technique. That can be explained by the fact that *tert-butyl-calixarenes* have shorter alkyl groups attached to the lower rim than *resorcinarenes* (see Fig. 97). Consequently, the spatial structure of thermally evaporated *tert-butyl-calixarene* molecules does not suffer too much. Despite we obtain a disordered layer after the evaporation, it was found that thermally evaporated *tert-butyl-calixarene* films showed the most repeatable and stable responses in comparison with other deposition techniques.

Tert-butyl-calixarene films were obtained by thermal evaporation in vacuum onto the cantilever surface. Knudsen cell and vacuum installation VUP-5M with residual pressure of 1.33×10^{-3} Pa was used for it. The thickness of the coatings was monitored directly during deposition with a built-in piezoelectric sensor.

Cantilever sensor coated with 150 nm thick *tert-butyl-calix[6]arene* is practically insensitive to water vapours, shows moderate sensitivity to different alcohols and good sensitivity to acetone vapours (Fig. 99). Sensitivity to water along with other compounds, which are likely to be adsorbed by hydrogen bonding, is rather negligible. This indicates that OH-groups at the lower rim of *tert-butyl-calix[6]arene*, which are directed inside the macrocycle, do not participate in anchoring of analytes. In its own turn, it suggests that water molecules do not penetrate the calixarene cavity. However, water and larger molecules of alcohols and acetone can fit the inter-calixarene cavities, thus providing greater response for those molecules that are spatially compatible with *tert-butyl* groups (e.g., acetone). It happens because tangled molecule-radical complex maximizes van der Waals contacts.

Fig. 100 shows Q-factors plotted for 100% concentration of each analyte. Q-factor modulation for different analytes can be explained by the fact that analyte molecules in the vicinity of the resonating cantilever are differently captured by its surface, thus increasing its effective mass. Correspondingly, analytes with lower sticking probability or faster adsorption-desorption kinetic would affect the cantilever effective mass to less extend. As it is confirmed by our experiments (Fig. 100), the smallest methanol molecules damp the cantilever motion less than larger 2-propanol or acetone molecules, which tend to interact with adsorbents slowly, e.g., as it was shown in Fig. 91.

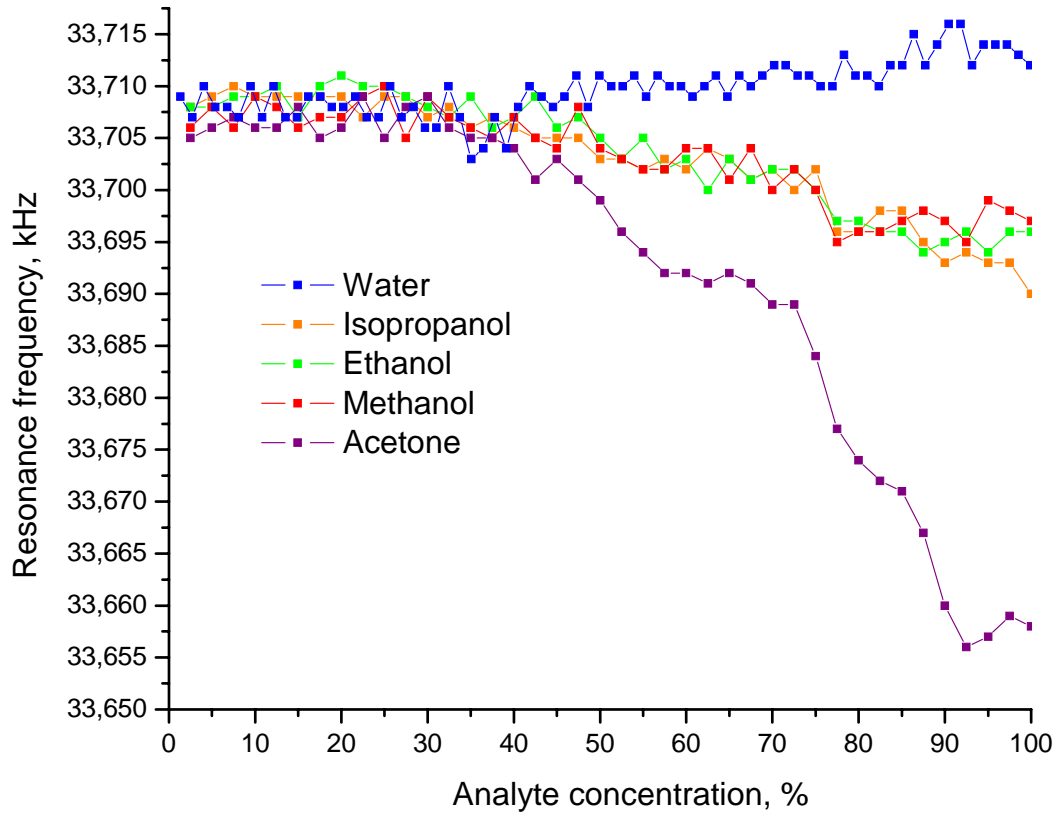


Fig. 99. Responses of a cantilever coated with thermally evaporated 150 nm thick tert-butyl-calix[6]arene layer.

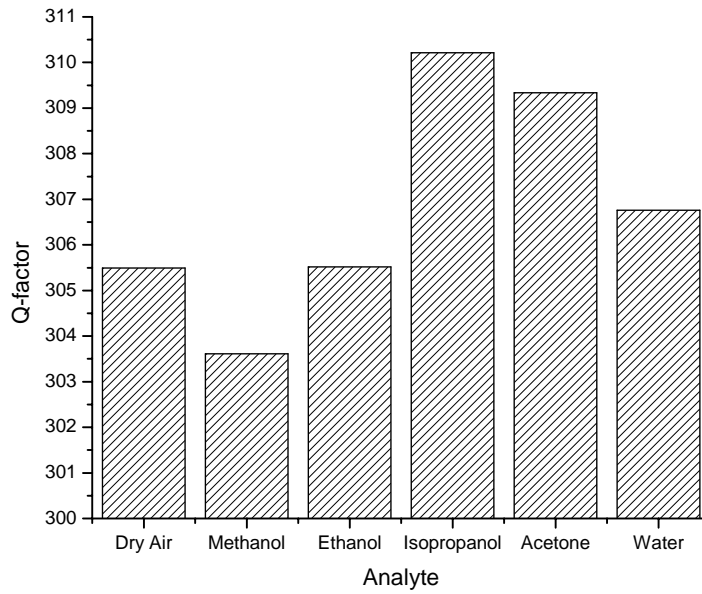


Fig. 100. Q-factor of a cantilever coated with thermally evaporated 150 nm thick tert-butyl-calix[6]arene layer at different analytes.

In summary, *tert-butyl-calix[6]arene* sorption performance is mostly defined by apolar *tert-butyl* groups and the intermolecular cavities, thus specific interaction has been found towards acetone, and low sensitivity to water and other hydrogen-bond analytes. Three types of specifically tailored phosphorylated calixarenes allowed comparing the influence of either hydroxyl or alkyl groups on the calixarene sorption properties.

Phosphorylated calixarenes are very promising for the gas sensors due to their interesting specific sorption properties to VOCs. In this study, three phosphorylated calixarenes, namely calix[4]arenbisphosphonic acid, calix[4]arentetraphosphinic acid, and calix[4]arentetraphosphinat, which for the simplicity will be further referred to as calixarene “F”, “G”, and “H” correspondingly (Fig. 101), were investigated by means of QCM and the cantilevers.

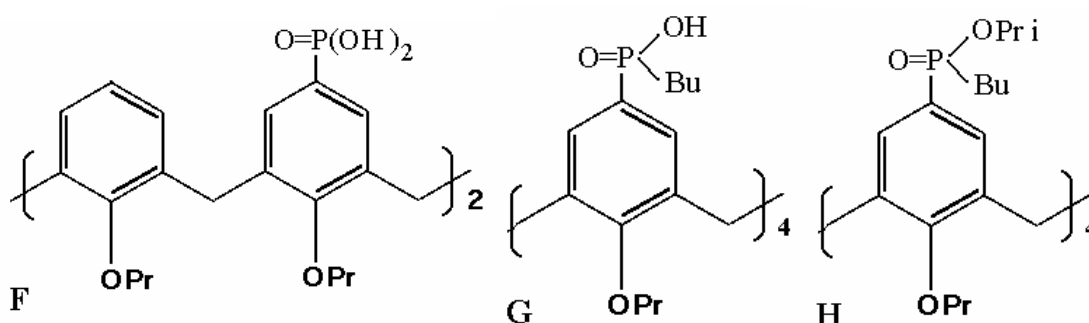


Fig. 101. Phosphorylated calixarenes: calix[4]arenbisphosphonic acid (F), calix[4]arentetraphosphinic acid (G), and calix[4]arentetraphosphinat (H). Specific designations: Pr- propyl group, Bu – butyl group, Pr i – isopropyl group:



(a) *n*-butyl group; $\text{CH}_3\text{CH}_2\text{CH}_2\text{CH}_2-$, (fully systematic name "butyl");

(b) *n*-propyl group; $\text{CH}_3\text{CH}_2\text{CH}_2-$, (fully systematic name "propyl");

(c) isopropyl group; $(\text{CH}_3)_2\text{CH}-$, (fully systematic name "1-methylethyl").

As one can see from Fig. 101, the calixarenes differ by the radicals attached to the phosphor atom. Four aromatic rings constitute the macrocycle of each compound represented. Correspondingly, calixarene “F”, which contains two hydroxyl groups, is most sensitive to ammonia, calixarene “G” with one hydroxyl group is less sensitive to ammonia than “F”, and calixarene “H” is not sensitive to ammonia, however exhibits particular sensitivity to alcohols and organochlorides instead.

The calixarenes were deposited by pipetting of the calixarene solutions (in the corresponding solvents) on QCM and cantilever surfaces. Then the solvents were dried in inert environment till full solvent evaporation. The film thicknesses were approximately 150 nm.

Investigation of adsorption properties of phosphorylated calixarenes to different volatile analytes, namely ethanol (C_2H_5OH), methanol (CH_3OH), acetone (CH_3COCH_3), and ammonia (NH_4OH) was carried out at QCM and cantilevers. Bar chart showing the sensor responses for 1000 ppm analyte injection is shown in Fig. 102. The cantilevers were also tested towards 2-propanol and water vapours as well as with some binary mixtures (Jim Beam, Ballantines, and Nemiroff). Sensitivities of all used phosphorylated calixarenes deposited on the cantilevers are summarized in Fig. 103. Sensitivity thresholds of QCM and cantilevers coated with phosphorylated calixarenes are summarised in Tab. 6.

Calixarene Analyte	F		G		H	
	QCM	Cantilever	QCM	Cantilever	QCM	Cantilever
Acetone	<100	<20	<50	<10	100	<50
Ethanol	200	<200	400	<400		
Methanol	300	<20	500	<500		
Ammonia	100	<10	<20	<100	not sensitive	

Tab. 6. Sensitivity thresholds [ppm] of QCM and cantilevers functionalized with different phosphorylated calixarenes.

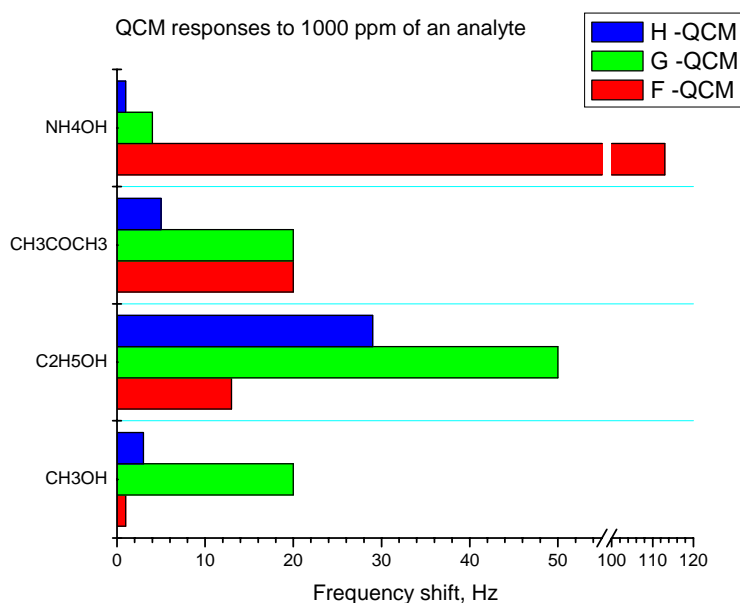


Fig. 102. Responses of QCM sensors coated with phosphorylated calixarenes (F, G, H) to 1000 ppm of different analytes.

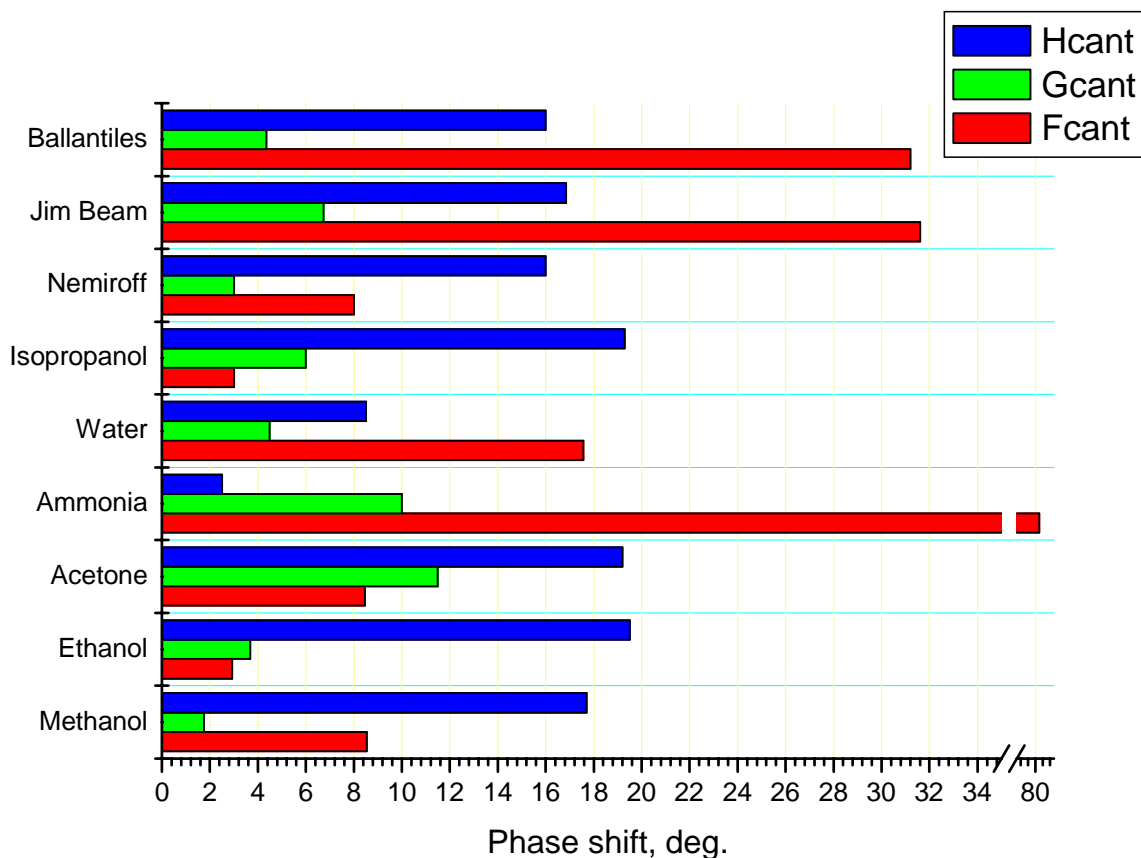


Fig. 103. Sensitivities of 3 different cantilevers functionalized with phosphorylated calixarenes to 33 vol% analyte concentrations.

Calixarene without functional groups show minimum sensitivity, whereas adding, e.g., two phosphoryl group $O=P(OPri)_2$ to the macrocycle sufficiently increases the sensitivity towards a range of analytes, especially organochlorides and aromatic organic solvents. Changing the propyl- to hydroxyl-groups (calixarene F) introduces sensitivity to ammonia, which is not practically registered without them. Sensor abilities of calixarenes F and G are similar due to the OH-groups. Only these two calixarenes are sensitive to ammonia down to tens ppm with also high selectivity. Sensitivity to other analytes is approximately two orders of magnitude lower. Calixarene H is sensitive to alcohols, however absence of hydroxyl groups makes it absolutely insusceptible to ammonia and hardly sensitive to water vapours. Calix[4]arentetraphosphinat-coated (calixarene “H”) transducer may discriminate well between three different compounds: water, ammonia, and alcohol vapours. However, the signal differences between different alcohols and acetone is relatively small. For this purpose one or more differently functionalized cantilever transducers should be employed in order to create an individual pattern for each VOC. On the contrary to resorcinarenes, phosphorylated calixarenes interact with alcohols not due to

hydrogen bonds, because in that case the most sensitive layers would be F and G, which is not observed.

General effect of an uncoated cantilever functionalization with phosphorylated calixarenes was considered in § 4.2, and in particular presented in Fig. 73. The cantilever selectivity to the volatile analytes was significantly enhanced due to the functionalization. An important observation is that the selective responses of the functionalized cantilevers may be not only increased, but also decreased in comparison with uncoated cantilevers. Particularly, adsorption of ammonia with high affinity to the silicon dioxide surfaces may be lowered if the cantilever is coated with calix[4]arenetetraphosphinate, which provides no hydroxyl binding sites (Fig. 73 and Fig. 101).

Such the way, this chapter demonstrates that cantilever functionalization with organic materials increases selectivity and sensitivity of the sensor. This effect is obvious for organic polymer layers, however using of specially tailored supramolecular complexes – calixarenes – make the selectivity patterns unambiguously sharper.

In this study, calixarene coatings, which act as specifically sensitive zeolites at the nanoscale, served for functionalization of different mass-sensitive transducers, such as quartz crystal microbalances (QCM) and microcantilevers. Transducers based on conductivity modulation in nanoparticle gold films were also thoroughly investigated during this work [20, 130]. Experimental results above confirm that combination of a highly sensitive transducer with nanostructured functionalization layers provides researcher with sensor elements for building up a task-specific sensor array for molecular recognition.

Chapter 6.

Conclusion and outlook

The most important achievements within this work include implementation of advantageous signal acquisition techniques, which improve the mass sensitivity of microcantilevers with integrated piezo-resistive read-out and bimorph-effect actuator down to attogram range, as well as investigation of novel functionalization materials, which are able to provide highly selective responses of the chemical sensor.

In comparison with other types of widely used (bio-)chemical sensors, modern state-of-the-art cantilever transducers offer better specific mass sensitivity (per area unit) [136]:

- Cantilever (dynamic mode): $0.025 \text{ fg} / \mu\text{m}^2 / \text{Hz}$;
- Quartz crystal microbalance: $0.17 \text{ fg} / \mu\text{m}^2 / \text{Hz}$;
- Surface plasmon resonance: $1.0 \text{ ng} / \mu\text{m}^2 / \text{Hz}$.

An important feature of cantilever-based sensors is that interaction between the sensor and its environment can be complementary characterised by gathering several response parameters from the cantilever driven in the resonant mode. Namely, resonance frequency, phase delay, oscillation amplitude, quality factor, and static deflection of the cantilever can be measured quasi-simultaneously.

In the frame of this work self-actuated piezo-resistive microcantilevers were applied as mass sensitive transducers in dynamic resonant mode, which is more stable and sensitive for the given cantilever design and the foreseen application fields. Four highly sensitive shallow-implanted piezo-resistors arranged in the Wheatstone bridge configuration provide integrated inexpensive read-out from the cantilevers along with temperature compensation and improved SNR. Integrated thermal actuator based on the bimorph effect reveals additional possibilities for miniaturisation.

Theoretical investigations of cantilever operation in static bending mode, dynamic resonant mode, phase shift mode, and higher eigenmodes have been thoroughly carried out. Calculated coefficients for the effective cantilever mass not only for the first, but also for higher eigenmodes are presented for the first time. This simplifies estimation of the added mass

according to simple “spring” formula not only for natural resonance, which is rather common approach, but also for higher eigenmodes as well.

While widely used finite-element software (e.g., Ansys ®) provide outperformed potential for the complex cantilever design simulations, analytical estimations may provide fast, accurate, and simple solutions, which are practically more useful for an applied adaptation. That is why the presented thesis relies mostly on the summarizing of the existing analytical techniques and also their expansion to the chemical sensor application of the cantilevers.

Cantilever microbalance operation in phase shift mode has not been described in literature, and the presented work fills this gap. Our experimental results suggest that we have lower noise and higher dynamical range by operating in phase shift mode instead of conventional measuring the frequency shift.

Elaboration and tuning of the experimental set-up in collaboration with Microsystems Ltd. (Varna, Bulgaria) was also an important achievement of this work. Three generations of application-specific measurement cells have been developed and tested. Low-noise pre-amplifier and board electronics have been realised for up to 8 cantilevers operated quazi-simultaneously. The board electronic have been designed for using in conjunction with PC-based ADC-DAC card. User-friendly software interface for cantilever control, signal acquisition and processing has been implemented. The set-up made it possible to gather plenty of experimental data in resonance frequency shift and phase shift modes.

Our experimental results have shown that the cantilever resonance frequency shifts with changing the exposed analyte concentration. In many cases this shift can be explained by additional mass load onto the cantilever surface. It has been proved that even uncoated (native oxide coated) cantilevers produce responses to different VOCs due to the normally hydrated surface. Investigation of cantilever-based gas sensors with inorganic coatings has been an important part of this work. Silicon oxide- (native and thermally grown), gold- and chalcohalide-coated cantilevers have been tested in gas flow mode with varying concentrations of water, ethanol, methanol, 2-propanol, acetone, and ammonia vapours. Demonstration of physical and chemical adsorption within these experiments became one of the key-topics of the present study. It has been also concluded that some chemisorbed analytes, e.g. ammonia, may modify the active surface and change (in our experiments – to improve) the sensitivity toward certain analytes of about one order of magnitude.

By using organic polymers or porous materials, like zeolites, as the sensing layer, one can enhance the sensitivity and reduce dispersion of the cantilever responses. Recognition of individual analytes and their binary mixtures based on 4-cantilevers array was carried out and published [22]. The cantilevers were functionalized by polydimethylsiloxane, polyvinylpyridine

and amorphous nitrogen-rich carbon nitride films with different thicknesses to ensure different selectivities and sensitivities toward water, methanol, 2-propanol and their binary mixtures. It was found that the cantilevers coated with CN_x films exhibit larger responses toward tested analytes with increasing layer thickness. The differences in the sensor recovery times can be used as another information parameter in addition to the resonance frequency shift for the identification of the individual components in the mixtures.

A novel class of nanostructured organic materials – calixarene – has been proposed as sensitive coatings for microcantilevers. Investigation of the basic operational principles of calixarene layers was one of the key issues of the presented work. Our experiments have shown that calixarenes, specially synthesised for sensing certain compound, leave behind over the conventional polymer in terms of selectivity. Three different calixarenes have demonstrated a drastic difference in their sorption abilities, making one of them very sensitive to ammonia vapours and practically insensitive to alcohols and vice versa.

The advantages of cantilever sensors can be further expanded by arranging individual cantilever transducers into large multisensor arrays integrated with on-chip electronic circuitry. One-dimensional and two-dimensional arrays of cantilever transducers offer additional advantages that cannot be overlooked. In particular, such arrays provide a viable platform for the development of high-performance “electronic noses”. Furthermore, the measured response patterns of the cantilever multi-array can be used as input to different recognition techniques such as principal component analysis (PCA) and artificial neural network (ANN) in order to classify and identify the tested analytes and their mixtures.

References

1. Göpel, W., J. Hesse, and J.N. Zemel, *Sensors : a comprehensive survey*. 1989.
2. Grandke, T., et al., *Fundamentals and general aspects*. 1989: p. XIII, 641 S.
3. Göpel, W., J. Hesse, and J.N. Zemel, *Chemical and biochemical sensors ; Pt. 1*. 1991: p. XVII, 716 S.
4. Persaud, K. and G. Dodd, *Analysis of Discrimination Mechanisms in the Mammalian Olfactory System Using a Model Nose*. *Nature*, 1982. **299**(5881): p. 352-355.
5. Rangelow, I.W., S. Skocki, and P. Dumania, *Plasma-Etching for Micromechanical Sensor Applications*. *Microelectronic Engineering*, 1994. **23**(1-4): p. 365-368.
6. Linnemann, R., et al., *Atomic force microscopy and lateral force microscopy using piezoresistive cantilevers*. *Journal of Vacuum Science & Technology B*, 1996. **14**(2): p. 856-860.
7. Ivanov, T., *Piezoresistive cantilevers with an integrated bimorph actuator*. PhD Thesis. 2004, Kassel. II, 133 S.
8. Ivanov, T., et al., *Thermally driven micromechanical beam with piezoresistive deflection readout*. *Microelectronic Engineering*, 2003. **67-8**: p. 550-556.
9. Lavrik, N.V., M.J. Sepaniak, and P.G. Datskos, *Cantilever transducers as a platform for chemical and biological sensors*. *Review of Scientific Instruments*, 2004. **75**(7): p. 2229-2253.
10. Ziegler, C., *Cantilever-based biosensors*. *Anal Bioanal Chem*, 2004. **379**(7-8): p. 946-59.
11. Carrascosa, L.G., et al., *Nanomechanical biosensors: a new sensing tool*. *Trac-Trends in Analytical Chemistry*, 2006. **25**(3): p. 196-206.
12. Lang, H.P., M. Hegner, and C. Gerber, *Cantilever array sensors*. *Materials Today*, 2005(April): p. 30-36.
13. Baller, M.K., et al., *A cantilever array-based artificial nose*. *Ultramicroscopy*, 2000. **82**(1-4): p. 1-9.
14. Lange, D., et al., *Complementary metal oxide semiconductor cantilever arrays on a single chip: mass-sensitive detection of volatile organic compounds*. *Anal Chem*, 2002. **74**(13): p. 3084-95.
15. Tang, Y.J., et al., *Detection of femtomolar concentrations of HF using an SiO₂ microcantilever*. *Analytical Chemistry*, 2004. **76**(9): p. 2478-2481.
16. Mertens, J., et al., *Detection of gas trace of hydrofluoric acid using microcantilever*. *Sensors and Actuators B-Chemical*, 2004. **99**(1): p. 58-65.
17. Yan, X.D., et al., *Detection of organophosphates using an acetyl cholinesterase (AChE) coated microcantilever*. *Instrumentation Science & Technology*, 2004. **32**(2): p. 175-183.
18. Alvarez, M., et al., *Nanomechanics of the formation of DNA self-assembled monolayers and hybridization on microcantilevers*. *Langmuir*, 2004. **20**(22): p. 9663-9668.
19. Monchev, B., et al., *Investigation of the sorption properties of thin Ge-S-AgI films deposited on cantilever-based gas sensor*. *Applied Physics a-Materials Science & Processing*, 2007. **87**(1): p. 31-36.
20. Filenko, D. and I.W. Rangelow, *Nano-electronic sensor elements for chemical recognition systems*. 2004, Kassel {[u.a.]}. 91 Bl.

21. Abedinov, N., et al., *Investigations of the sorption behaviour of amorphous nitrogen-rich carbon nitride films as sensitive layers for cantilever-based chemical sensors*. Applied Physics a-Materials Science & Processing, 2004. **79**(3): p. 531-536.
22. Abedinov, N., et al., *Chemical recognition based on micromachined silicon cantilever array*. Journal of Vacuum Science & Technology B, 2003. **21**(6): p. 2931-2936.
23. Abedinov, N., et al., *Micromachined piezoresistive cantilever array with integrated resistive microheater for calorimetry and mass detection*. Journal of Vacuum Science & Technology a-Vacuum Surfaces and Films, 2001. **19**(6): p. 2884-2888.
24. Zambov, L.M., et al., *Gas-sensitive properties of nitrogen-rich carbon nitride films*. Advanced Materials, 2000. **12**(9): p. 656-+.
25. Yum, K., et al., *Experimental measurement and model analysis of damping effect in nanoscale mechanical beam resonators in air*. Journal of Applied Physics, 2004. **96**(7): p. 3933-3938.
26. Kooser, A., et al., *Gas sensing using embedded piezoresistive microcantilever sensors*. Sensors and Actuators B-Chemical, 2004. **99**(2-3): p. 474-479.
27. Fadel, L., et al., *Chemical sensing: millimeter size resonant microcantilever performance*. Journal of Micromechanics and Microengineering, 2004. **14**(9): p. S23-S30.
28. Fadel, L., et al., *Signal-to-noise ratio of resonant microcantilever type chemical sensors as a function of resonant frequency and quality factor*. Sensors and Actuators B-Chemical, 2004. **102**(1): p. 73-77.
29. Gunter, R.L., et al., *Investigation of DNA sensing using piezoresistive microcantilever probes*. Ieee Sensors Journal, 2004. **4**(4): p. 430-433.
30. Pei, J.H., F. Tian, and T. Thundat, *Glucose biosensor based on the microcantilever*. Analytical Chemistry, 2004. **76**(2): p. 292-297.
31. Yan, X.D., H.F. Ji, and Y. Lvov, *Modification of microcantilevers using layer-by-layer nanoassembly film for glucose measurement*. Chemical Physics Letters, 2004. **396**(1-3): p. 34-37.
32. Zhang, Y.F., et al., *Micromechanical measurement of membrane receptor binding for label-free drug discovery*. Biosensors & Bioelectronics, 2004. **19**(11): p. 1473-1478.
33. Lee, J.H., T.S. Kim, and K.H. Yoon, *Effect of mass and stress on resonant frequency shift of functionalized Pb(Zr_{0.52}Ti_{0.48})O₃ thin film microcantilever for the detection of C-reactive protein*. Applied Physics Letters, 2004. **84**(16): p. 3187-3189.
34. Lee, J.H., et al., *Label free novel electrical detection using micromachined PZT monolithic thin film cantilever for the detection of C-reactive protein*. Biosens Bioelectron, 2004. **20**(2): p. 269-75.
35. Yinon, J., *Detection of explosives by electronic noses*. Analytical Chemistry, 2003. **75**(5): p. 99a-105a.
36. Pinnaduwege, L.A., et al., *Detection of 2,4-dinitrotoluene using microcantilever sensors*. Sensors and Actuators B-Chemical, 2004. **99**(2-3): p. 223-229.
37. Pinnaduwege, L.A., et al., *Detection of trinitrotoluene via deflagration on a microcantilever*. Journal of Applied Physics, 2004. **95**(10): p. 5871-5875.
38. Zhang, J. and H.F. Ji, *An anti E-coli O157 : H7 antibody-immobilized microcantilever for the detection of Escherichia coli (E-coli)*. Analytical Sciences, 2004. **20**(4): p. 585-587.
39. Gfeller, K.Y., N. Nugaeva, and M. Hegner, *Micromechanical oscillators as rapid biosensor for the detection of active growth of Escherichia coli*. Biosensors & Bioelectronics, 2005. **21**(3): p. 528-533.
40. Ke, L. and H.-F. Ji, *Anal. Sci.*, 2004. **20**.
41. Zhang, Y.F., et al., *A pH sensor based on a microcantilever coated with intelligent hydrogel*. Instrumentation Science & Technology, 2004. **32**(4): p. 361-369.
42. Tian, F., et al., *Observation of the surface stress induced in microcantilevers by electrochemical redox processes*. Ultramicroscopy, 2004. **100**(3-4): p. 217-23.

43. Bottomley, L.A., M.A. Poggi, and S.X. Shen, *Impact of nano- and mesoscale particles on the performance of microcantilever-based sensors*. Analytical Chemistry, 2004. **76**(19): p. 5685-5689.
44. Ryu, W.H., et al., *Computer simulation of the resonance characteristics and the sensitivity of cantilever-shaped Al/PZT/RuO₂ biosensor*. Sensors and Actuators B-Chemical, 2004. **97**(1): p. 98-102.
45. Ren, Q. and Y.P. Zhao, *Influence of surface stress on frequency of microcantilever-based biosensors*. Microsystem Technologies-Micro-and Nanosystems-Information Storage and Processing Systems, 2004. **10**(4): p. 307-314.
46. Khaled, A.R.A. and K. Vafai, *Optimization modeling of analyte adhesion over an inclined microcantilever-based biosensor*. Journal of Micromechanics and Microengineering, 2004. **14**(8): p. 1220-1229.
47. Zhang, Y., Q. Ren, and Y.P. Zhao, *Modelling analysis of surface stress on a rectangular cantilever beam*. Journal of Physics D-Applied Physics, 2004. **37**(15): p. 2140-2145.
48. Tang, Y.J., et al., *Fabrication and characterization of SiO₂ microcantilever for microsensor application*. Sensors and Actuators B-Chemical, 2004. **97**(1): p. 109-113.
49. Hu, Z.Y., et al., *Calibration of optical cantilever deflection readers*. Review of Scientific Instruments, 2004. **75**(2): p. 400-404.
50. Jeon, S. and T. Thundat, *Instant curvature measurement for microcantilever sensors*. Applied Physics Letters, 2004. **85**(6): p. 1083-1084.
51. Bambu, G.-G. and e. al., Macromol. Chem. Phys., 2004. **205**(13): p. 1713.
52. McFarland, A.W., et al., *Production and characterization of polymer microcantilevers*. Review of Scientific Instruments, 2004. **75**(8): p. 2756-2758.
53. Ilic, B., et al., *Attogram detection using nanoelectromechanical oscillators*. Journal of Applied Physics, 2004. **95**(7): p. 3694-3703.
54. Sharos, L.B., et al., *Enhanced mass sensing using torsional and lateral resonances in microcantilevers*. Applied Physics Letters, 2004. **84**(23): p. 4638-4640.
55. Lin, R., P. Boggild, and O. Hansen, *Microcantilever equipped with nanowire template electrodes for multiprobe measurement on fragile nanostructures*. Journal of Applied Physics, 2004. **96**(5): p. 2895-2900.
56. Yue, M., et al., *A 2-D microcantilever array for multiplexed biomolecular analysis*. Journal of Microelectromechanical Systems, 2004. **13**(2): p. 290-299.
57. Thundat, T., et al., *Vapor Detection Using Resonating Microcantilevers*. Analytical Chemistry, 1995. **67**(3): p. 519-521.
58. Boltshauser, T., et al., J. Micromech. Microeng., 1992. **2**: p. 205-207.
59. Thundat, T., et al., *Detection of Mercury-Vapor Using Resonating Microcantilevers*. Applied Physics Letters, 1995. **66**(13): p. 1695-1697.
60. Hierlemann, A., et al., *Application-specific sensor systems based on CMOS chemical microsensors*. Sensors and Actuators B-Chemical, 2000. **70**(1-3): p. 2-11.
61. Maute, M., et al., *Detection of volatile organic compounds (VOCs) with polymer-coated cantilevers*. Sensors and Actuators B-Chemical, 1999. **58**(1-3): p. 505-511.
62. Lange, D., et al., Digest of Technical Papers TRANSDUCERS, 1999. **Sendai, Japan**: p. 1020-1023.
63. Lange, D., et al., Proc. SPIE, 1998. **3224**: p. 233-243
64. Lange, D., et al., Proc. IEEE MEMS, 2000(Myazaki, Japan): p. 547-552.
65. Britton, C.L., Jr., et al., *Multiple-input microcantilever sensors*. Ultramicroscopy, 2000. **82**(1-4): p. 17-21.
66. Kim, B.H., et al., *Multicomponent analysis and prediction with a cantilever array based gas sensor*. Sensors and Actuators B-Chemical, 2001. **78**(1-3): p. 12-18.
67. Koll, A., et al., Proc. SPIE, 1999.
68. Hagleitner, C., et al., Technical Digest TRANSDUCERS, 1999(Sendai, Japan): p. 1012-1015.

69. Kerness, N., et al., Proc. IEEE MEMS, 2000(Myazaki, Japan): p. 96-101.
70. Vashist, S.K., *A Review of Microcantilevers for Sensing Applications*. Journal of Nanotechnology Online, 2007; <http://www.azonano.com/Details.asp?ArticleID=1927>.
71. Lang, H.P., et al., *An Artificial Nose Based on Microcantilever Array Sensors*. Journal of Physics, 2007. **Conference Series 61**: p. 663–667.
72. Nugaeva, N., et al., *An antibody-sensitized microfabricated cantilever for the growth detection of Aspergillus niger spores*. Microsc Microanal, 2007. **13**(1): p. 13-7.
73. Nugaeva, N., et al., *Micromechanical cantilever array sensors for selective fungal immobilization and fast growth detection*. Biosens Bioelectron, 2005. **21**(6): p. 849-56.
74. Fritz, J., et al., *Translating biomolecular recognition into nanomechanics*. Science, 2000. **288**(5464): p. 316-318.
75. Gimzewski, J.K., et al., *Observation of a Chemical-Reaction Using a Micromechanical Sensor*. Chemical Physics Letters, 1994. **217**(5-6): p. 589-594.
76. Berger, R., et al., J. Science, 1997(276).
77. Baltès, H., D. Lange, and A. Koll, IEEE Spectrum, 1998. **9**: p. 35-38.
78. Pedrak, R., et al., *Micromachined atomic force microscopy sensor with integrated piezoresistive, sensor and thermal bimorph actuator for high-speed tapping-mode atomic force microscopy phase-imaging in higher eigenmodes*. Journal of Vacuum Science & Technology B, 2003. **21**(6): p. 3102-3107.
79. Chen, G.Y., et al., *Adsorption-induced surface stress and its effects on resonance frequency of microcantilevers*. J. Appl. Phys., 1995. **77**: p. 3618-3622.
80. Sarid, D., *Scanning force microscopy : with applications to electric, magnetic, and atomic forces*. 1991, New York: Oxford University Press. xi, 253 p.
81. Dufour, I. and L. Fadel, *Resonant microcantilever type chemical sensors: analytical modeling in view of optimization*. Sensors and Actuators B-Chemical, 2003. **91**(1-3): p. 353-361.
82. Stoney, G.G., *The Tension of Metallic Films Deposited by Electrolysis* Proceedings of the Royal Society of London. Series A., 1909. **82**(553): p. 172-175.
83. von Preissig, F.J., *Applicability of the classical curvature-stress relation for thin films on plate substrates*. J. Appl. Phys., 1989. **66**(9): p. 4262-4268.
84. Shuttleworth, R., *The Surface Tension of Solids*. Proc. Phys. Soc. A, 1950. **63**: p. 444-457.
85. Cherian, S. and T. Thundat, *Determination of adsorption-induced variation in the spring constant of a microcantilever*. Applied Physics Letters, 2002. **80**(12): p. 2219-2221.
86. Elmer, F.J. and M. Dreier, *Eigenfrequencies of a rectangular atomic force microscope cantilever in a medium*. Journal of Applied Physics, 1997. **81**(12): p. 7709-7714.
87. Han, J.Q., et al., *Dependence of the resonance frequency of thermally excited microcantilever resonators on temperature*. Sensors and Actuators a-Physical, 2002. **101**(1-2): p. 37-41.
88. Jin, D.Z., et al., *High-mode resonant piezoresistive cantilever sensors for tens-femtogram resolvable mass sensing in air*. Journal of Micromechanics and Microengineering, 2006. **16**(5): p. 1017-1023.
89. Thundat, T., et al., *Thermal and ambient-induced deflections of scanning force microscope cantilevers*. Appl. Phys. Lett., 1994. **64**: p. 2894-2896.
90. Cherian, S., A. Mehta, and T. Thundat, *Investigating the mechanical effects of adsorption of Ca²⁺ ions on a silicon nitride microcantilever surface*. Langmuir, 2002. **18**(18): p. 6935-6939.
91. Dohn, S., et al., *Enhanced functionality of cantilever based mass sensors using higher modes*. Applied Physics Letters, 2005. **86**(23): p. -.
92. Ekinici, K.L., Y.T. Yang, and M.L. Roukes, *Ultimate limits to inertial mass sensing based upon nanoelectromechanical systems*. Journal of Applied Physics, 2003. **95**(5): p. 2682-2689.

93. Hosaka, H., K. Itao, and S. Kuroda, *Damping Characteristics of Beam-Shaped Micro-Oscillators*. Sensors and Actuators a-Physical, 1995. **49**(1-2): p. 87-95.
94. Sader, J.E., *Frequency response of cantilever beams immersed in viscous fluids with applications to the atomic force microscope*. Journal of Applied Physics, 1998. **84**(1): p. 64-76.
95. Tamayo, J., *Study of the noise of micromechanical oscillators under quality factor enhancement via driving force control*. Journal of Applied Physics, 2005. **97**(4): p. -.
96. Tamayo, J., M. Alvarez, and L.M. Lechuga, *Digital tuning of the quality factor of micromechanical resonant biological detectors*. Sensors and Actuators B-Chemical, 2003. **89**(1-2): p. 33-39.
97. Yasumura, K.Y., et al., *Quality factors in micron- and submicron-thick cantilevers*. Journal of Microelectromechanical Systems, 2000. **9**(1): p. 117-125.
98. Houston, B.H., et al., *Thermoelastic loss in microscale oscillators*. Applied Physics Letters, 2002. **80**(7): p. 1300-1302.
99. Stemme, G., *Resonant silicon sensors*. J. Micromech. Microeng., 1991. **1**: p. 113-125.
100. Lifshitz, R. and M.L. Roukes, *Thermoelastic damping in micro- and nanomechanical systems*. Physical Review B, 2000. **61**(8): p. 5600-5609.
101. Lifshitz, R., *Phonon-mediated dissipation in micro- and nano-mechanical systems*. Physica B-Condensed Matter, 2002. **316**: p. 397-399.
102. Kim, S.J., T. Ono, and M. Esashi, *Capacitive resonant mass sensor with frequency demodulation detection based on resonant circuit*. Applied Physics Letters, 2006. **88**(5): p. -.
103. Zhou, W., et al., *Simulation and design of piezoelectric microcantilever chemical sensors*. Sensors and Actuators a-Physical, 2005. **125**(1): p. 69-75.
104. Timoshenko, S.P., *Analysis of bi-metal thermostats*. J. Opt. Soc. Am., 1925. **11**: p. 233-.
105. Jianqiang, H., et al., *Dependence of the resonance frequency of thermally excited microcantilever resonators on temperature*. Sensors and Actuators A: Physical, 2002. **101**(1-2): p. 37-41.
106. Moulin, A.M., R.J. Stephenson, and M.E. Welland, *Micromechanical thermal sensors: Comparison of experimental results and simulations*. Journal of Vacuum Science & Technology B, 1997. **15**(3): p. 590-596.
107. Barnes, J.R., et al., *Photothermal Spectroscopy with Femtojoule Sensitivity Using a Micromechanical Device*. Nature, 1994. **372**(6501): p. 79-81.
108. Timoshenko, S. and J.M. Lessells, *Applied elasticity*. 1st ed. 1925, East Pittsburgh, Pa.: Westinghouse technical night school press. xxi p., 1l., 544 p.
109. Datskos, P.G. and I. Sauers, *Detection of 2-mercaptoethanol using gold-coated micromachined cantilevers*. Sensors and Actuators B-Chemical, 1999. **61**(1-3): p. 75-82.
110. Thundat, T. and L. Maya, *Monitoring chemical and physical changes on sub-nanogram quantities of platinum dioxide*. Surface Science, 1999. **430**(1-3): p. L546-L552.
111. Battiston, F.M., et al., *A chemical sensor based on a microfabricated cantilever array with simultaneous resonance-frequency and bending readout*. Sensors and Actuators B-Chemical, 2001. **77**(1-2): p. 122-131.
112. Киселев, В.Ф., С.Н. Козлов, and А.В. Зотеев, *Основы физики поверхности твердого тела*. 1999, М.: Изд-во Московского университета. Физический факультет МГУ. 284.
113. Pinnaduwege, L.A., et al., *Desorption characteristics of uncoated silicon microcantilever surfaces for explosive and common nonexplosive vapors*. Ultramicroscopy, 2004. **100**(3-4): p. 211-216.
114. Tomova, R., R. Stoycheva-Topalova, and A. Buroff, J. Optoelectron. Adv. Mater., 2005. **7**.
115. Vassilev, V.S. and S.V. Boycheva, Talanta, 2005. **67**.

116. Schoning, M.J., et al., *Thin film sensors on the basis of chalcogenide glass materials prepared by pulsed laser deposition technique*. Sensors and Actuators B-Chemical, 2000. **68**(1-3): p. 254-259.
117. Li, P., et al., *Silicon dioxide microcantilever with piezoresistive element integrated for portable ultrasensitive gaseous detection*. Applied Physics Letters, 2006. **89**(7): p. -.
118. Pinnaduwa, L.A., et al., *Sensitive detection of plastic explosives with self-assembled monolayer-coated microcantilevers*. Applied Physics Letters, 2003. **83**(7): p. 1471-1473.
119. Datskos, P.G., N.V. Lavrik, and M.J. Sepaniak, *Detection of explosive compounds with the use of microcantilevers with nanoporous coatings*. Sensor Letters, 2003. **1**(1): p. 25-32.
120. Lang, H.P., et al., *A chemical sensor based on a micromechanical cantilever array for the identification of gases and vapors*. Applied Physics a-Materials Science & Processing, 1998. **66**: p. S61-S64.
121. Lang, H.P., et al., *Sequential position readout from arrays of micromechanical cantilever sensors*. Applied Physics Letters, 1998. **72**(3): p. 383-385.
122. Ferrari, V., et al., *Development and application of mass sensors based on flexural resonances in alumina beams*. Ieee Transactions on Ultrasonics Ferroelectrics and Frequency Control, 1996. **43**(4): p. 601-608.
123. Boisen, A., et al., *Environmental sensors based on micromachined cantilevers with integrated read-out*. Ultramicroscopy, 2000. **82**(1-4): p. 11-16.
124. Dickert, F.L. and R. Sikorski, *Supramolecular strategies in chemical sensing*. Materials Science & Engineering C-Biomimetic and Supramolecular Systems, 1999. **10**(1-2): p. 39-46.
125. Chen, L.X., et al., *Calixarene derivatives as the sensory molecules for silver ion-selective electrode*. Microchemical Journal, 2000. **65**(2): p. 129-135.
126. Mlika, R., et al., *Study of ion-selective evaporated calixarene film used as a sensitive layer on ISFET sensors*. Sensors and Actuators B-Chemical, 1998. **47**(1-3): p. 43-47.
127. Mlika, R., et al., *Calixarene membranes on semiconductor substrates for EIS chemical sensors*. Electrochimica Acta, 1998. **43**(8): p. 841-847.
128. Koshets, I.A., et al., *Calixarene films as sensitive coatings for QCM-based gas sensors*. Sensors and Actuators B-Chemical, 2005. **106**(1): p. 177-181.
129. Hartmann, J., et al., *Supramolecular interactions on mass sensitive sensors in gas phases and liquids*. Sensors and Actuators B-Chemical, 1996. **34**(1-3): p. 305-311.
130. Filenko, D., et al., *Chemical gas sensors based on calixarene-coated discontinuous gold films*. Sensors and Actuators B-Chemical, 2005. **111**: p. 264-270.
131. Gebauer, S. *Calixaren-Kieselgele unterschiedlich große Makrocyclen als chromatographische Selektoren in der HPLC*. [cited; Online-Ressource.].
132. Katz, A., et al., *The first single-step immobilization of a calix-[4]-arene onto the surface of silica*. Chemistry of Materials, 2002. **14**(8): p. 3364-3368.
133. Ludwig, R. and N.T.K. Dzung, *Calixarene-based molecules for cation recognition*. Sensors, 2002. **2**(10): p. 397-416.
134. Kunihiro, I., *Characteristics of monolayers of calix[4]resorcinarenes derivatives having azobenzene chromophores*. Materials Science and Engineering C 1999(8-9): p. 353-359.
135. Sauerbrey, G., *Verwendung von Schwingquarzen zur Wagung dünner Schichten und zur Mikrowägung*. Z. Phys., 1959. **155**: p. 206.
136. Lang, H.P., *Nanomechanics: Exploring new frontiers in biosensing and diagnostics*, in *NanoBio Europe*. 2007: Münster, Germany. p. 66.

Abbreviations

AC	Alternating Current
ADC	Analog-to-Digital Converter
AFM	Atomic Force Microscopy
ANN	Artificial Neural Network
BET	Brunauer-Emmet-Teller (theory)
CMOS	Complementary Metal-Oxide Semiconductor
DAC	Digital-to-Analog Converter
DC	Direct Current
DDS	Direct Digital Synthesis
DNA	Deoxyribonucleic Acid
DNT	Dinitrotoluene
EIS	Electrolyte-Insulator-Semiconductor (sensors)
FEM	Finite-Element Method
ICP-CVD	Inductively Coupled Plasma Chemical Vapour Deposition
IR	Infrared
ISE	Ion-Selective Electrodes
ISFET	Ion-Selective Field Effect Transistors
LB	Langmuir-Blodgett
LDL	Low-Density Lipoprotein
MEMS	Microelectromechanical Systems
MFC	Mass-Flow Controller
MOS	Metal-Oxide Semiconductor
MUX	Multiplexer
NEMS	Nanoelectromechanical Systems
NMR	Nuclear Magnetic Resonance
PC	Personal Computer
PCB	Printed Circuit Board
PDMS	Polydimethylsiloxane

PMMA	Polymethylmethacrylate
ppb	parts per billion
ppm	parts per million
PSA	Prostatic Specific Antigen
PTFE	Polytetrafluoroethylene
PVP	Polyvinylpyridine
QCM	Quartz-Crystal Microbalance
Rh	Relative humidity
RMS	Root Mean Square
SAM	Self-Assembled Monolayer
SAN	Styrene-Acrylonitrile
SAW	Surface Acoustic Wave
SNR	Signal-to-Noise Ratio
TNT	Trinitrotoluene
UV	Ultraviolet
VCl-VA	Vinylchloride-Vinylacetate
VOC	Volatile Organic Compound

List of publications prepared during PhD work

Articles in referred journals:

1. D. Filenko, T. Ivanov, B. Volland, K. Ivanova, I. W. Rangelow, N. Nikolov, T. Gotszalk, and J. Mielczarski. **Experimental setup for characterization of self-actuated microcantilevers with piezoresistive readout for chemical recognition of volatile substances** // Rev. Sci. Instrum., 2008, Vol. 79, 094101, 6 pages.
2. B. Monchev, D. Filenko, N. Nikolov, C. Popov, T. Ivanov, P. Petkov, and I.W. Rangelow. **Investigation of the sorption properties of thin Ge–S–AgI films deposited on cantilever-based gas sensor** // Applied Physics A, 2007, Vol. 87, No. 1, pp. 31-36.
3. I. W. Rangelow, T. Ivanov, B. Volland, D. Dontsov, Y. Sarov, K. Ivanova, A. Persaud, D. Filenko, N. Nikolov, M. Zier, B. Schmidt, T. Gotszalk, T. Sulzback. **Raster-Sonden-Mikroskopie mit Cantilever-Arrays (Scanning Probe Microscopy with Cantilever Arrays)** // Technisches Messen, 2006, Vol. 73, Issue 9, pp. 485-492 (in German).
4. D. Filenko, T. Gotszalk, Z. Kazantseva, O. Rabinovych, I. Koshets, Yu. Shirshov, V. Kalchenko, and I. W. Rangelow. **Chemical gas sensors based on calixarene-coated discontinuous gold films** // Sensors and Actuators B, 2005, Vol. 111-112, pp. 264-270.
5. O. Rabinovych, A. Uvarov, D. Filenko, and I.W. Rangelow. **Radicals transport modelling in NANOJET** // Applied Physics A, 2005, Vol. 81, pp. 1661-1666.
6. N. Abedinov, C. Popov, Zh. Yordanov, Tzv. Ivanov, T. Gotszalk, P. Grabiec, W. Kulisch, I. W. Rangelow, D. Filenko, and Yu. Shirshov. **Chemical recognition based on micromachined silicon cantilever array** // Journal of Vacuum Science & Technology B: Microelectronics and Nanometer Structures, 2003, Vol. 21, Issue 6, pp. 2931-2936.

Conference contributions:

1. D. Filenko, B. Volland, T. Ivanov, N. Nikolov, K. Ivanova, Y. Sarov, V. Kalchenko, Z. Kazantseva, I. Koshets, Yu. Shirshov, and I. W. Rangelow. **(Bio-)chemical recognition using cantilever array** // Poster presentation at the international conference on nanobiotechnology “NanoBio-Europe 2007”, Münster, Germany, 13-15 June 2007.
2. D. Filenko, T. Ivanov, B. Volland, N. Nikolov, K. Ivanova, Y. Sarov, V. Kalchenko, Z. Kazantseva, Yu. Shirshov, A. Beliaev, and I. W. Rangelow. **Chemical Recognition Using Cantilever Array** // Abstracts book of Ukrainian-German Symposium on Nanobiotechnology, Kiev, Ukraine, 14-16 December 2006, p. 59; poster presentation.
3. Denis Filenko, Zoya Kazantseva, Olexandr Rabinovych, Katerina Ivanova, Yuri Shirshov, Vitaly Kalchenko and Ivo Rangelow. **Calixarene-coated nanoparticle gold films for chemical recognition system** // Abstracts of the International Conference “IEEE Sensors 2004”, Vienna, Austria, 24-27 October 2004, p. 153; oral presentation.
4. D. Filenko, Z. Kazantseva, K. Ivanova, O. Rabinovych, A. Kukla, Yu. Shirshov, V. I. Kalchenko, and I. W. Rangelow. **Calixarene-coated nanoparticle gold films for chemical recognition system** // Proceedings of the IEEE Sensors 2004 Conference, Vienna, Austria, October 24-27, 2004, pp. 669-672.
5. D. Filenko, O. Rabinovych, Yu. Shirshov, V. I. Kalchenko, I. W. Rangelow. **Nanomotion in functionalized nanoparticle gold films under exposure to volatile analytes** // Abstracts of the International Conference “MNE 2004 (Micro and Nano Engineering 2004)”, Rotterdam, The Netherlands, 19-22 September 2004, pp. 236-237; poster presentation.
6. D. Filenko, N. Abedinov, A. Kukla, Z. Kazantseva, S. Zynio, I. Koshets, Yu. Shirshov, and I. W. Rangelow. **Chemical gas sensors based on calixarene-coated discontinuous gold films** // Digest of Technical Papers of the International Conference “Eurosensors XVIII”, Rome, Italy, 13-15 September 2004, pp. 329-330; poster presentation.

Acknowledgements

First of all, I would like to express my sincere gratitude to Professor Ivo Rangelow, who proposed this research topic, and who has been supporting me during its fulfilment. His enthusiasm and research devotion have been inspiring me many times, and his management efforts made it possible to carry out this research. I am very thankful for his teaching and valuable remarks during my professional growth at his research group, and also for his help with my publications and presentations.

This work was carried out at the Institute of Nanostructure Technology and Analytics (INA). I am very thankful to my supervisors and reviewers, Professor Johann Peter Reithmaier and Professor Hartmut Hillmer, for my employment and their kind support.

Professor Yuri Shirshov from Kiev introduced me to a very exciting field of (bio-)chemical sensors, and helped me many times with his comprehensive scientific advisory. His impact to my scientific understanding cannot be overestimated.

Dr. Nikolay Abedinov proved to be my guru not only with the experimental work. He also initiated me into some simple but important aspects of living in Germany on my arrival. Another my 'German life' guru was Dr. Alex Rabinovych, whose continuous help during my stay in Kassel saved me a lot of time and energy.

I would like to thank Dr. Burkhard Volland, Dr. Tzvetan Ivanov, and Dr. Yanko Sarov for many useful discussions, collaborative work, and friendly support. I would like to thank Albert Malkomes, Michael Plätzer, and Dirk Albert for the technical maintenance. I am very thankful to Katja Ivanova, Lewis Lingys, Boris Monchev, Kolyo Kolev, Tino Pfau, Dr. Robert Pedrak, Dr. Alexander Gutscherov, Dr. Cyril Popov, and all my other INA-colleagues for those collaborative and pleasant hours that we spent together.

Special thank goes to Nikolay Nikolov from Microsystems Ltd. (Varna, Bulgaria) for the next generation measurement electronics according to high industrial standards. His outstanding ability to perform over the expectations made working with him an example of true collaboration, as it must be. It was my pleasure to meet you and work with you.

I am very grateful to Dr. Zoya Kazantseva, Dr. Stepan Synio, and Professor Vitaly Kalchenko, who helped me with calixarenes and organic polymers. All my friends and colleagues from Kiev, thank you for your countenance and many nice and useful conversations.

I would like to thank Holger Breter and Dr. Jens Ulbrich from AlphaContec GmbH for lucky collaborative opportunities, and the staff of Technische Universität Ilmenau for care and support; European Commission for TASNANO EC project No. NMP4-CT-2005-516865, and BMBF for UKR 01/056 project.

I am very thankful to Dida and Gerd Zuncke for the power to believe.

My sweetest background all over the time, Tanja! Your patience, understanding and encouragement are staying behind each page of this work. Thank you very much for your support and especially for my son Julian, whose smiling face makes me happy.

Everyone who was helping me during fulfilment of this work and who was making me happy those years – I appreciate deeply all your support and countenance!